N^o d'ordre : **03/2013-D/MT**

UNIVERSITE DES SCIENCES ET DE LA TECHNOLOGIE
HOUARI BOUMEDIENE, ALGER.
FACULTÉ DE MATHÉMATIQUES.

THÈSE

Présentée pour l'obtention du grade de DOCTORAT
En : mathématiques

Spécialité : ANALYSE : Equations aux Dérivées partielles

Par :

KACIMI ABDERRAHIM

Thème

A numerical investigation of the barotropic instability on the equatorial β-plane

Soutenue publiquement le 21 Février 2013 devant le jury composé :

Président :	D. Teniou PROFESSEUR,	à l' U.S.T.H.B	(Alger)
Directeur :	T. Aliziane MAITRE DE CONFÉRENCE/A,	à l' U.S.T.H.B	(Alger)
Directeur :	B. Khouider PROFESSEUR,	à l' U.victoria	(Canada)
Examinateurs :	Ms. Moulay PROFESSEUR,	à l'U.S.T.H.B	(Alger)
	T.Boulmezaoud PROFESSEUR,	à l' U. versailles	(France)
	N.Hannoun MAITRE DE CONFÉRENCE/A,	a l' U.S.T.H.B	(Alger)

Resume

Dans la première partie de cette thèse, on utilise la méthode du Jacobien d'Arakawa [1] et le schéma Essentiellement Non Oscillant (ENO-4) d'ordre quatre de Osher et Shu [41] pour la résolution numérique des équations barotropes dans le plan bêta équatorial. Le Jacobien d'Arakawa est un schéma centré aux différences finis d'ordre deux qui conserve l'énergie et l'enstrophie. Le schéma Essentiellement Non Oscillant d'ordre quatre (ENO-4) est spécifiquement utilisé dans la cadre des lois de conservation ainsi que la résolution des équations de Hamilton-Jacobi et ce schéma est traditionnellement utilisé pour suivre l'évolution du front. Nous nous sommes intéressé à la performance de ces deux méthodes pour la résolution des équations barotropes afin de déterminer si elles sont adéquates pour une étude numérique de l'instabilité barotrope. Les deux méthodes sont testées et comparées sur deux types de solutions exactes, une onde-packet régulière de Rossby et un cisaillement du vent discontinu, sur une longue période à l'échelle de climat de 100 jours. Les résultats numériques montrent que la méthode du Jacobien d'Arakawa conserve l'énergie et l'enstrophie presque exactement. En particulier, elle capte la vitesse de phase de l'onde de Rossby et converge vers la solution exacte avec un ordre de précision qui égale à deux dans les deux cas. Les mêmes propriétés sont conservées par le schéma ENO-4. Toute fois l'ordre quatre de précision est obtenu pour la solution règulière de l'onde de Rossby, alors que dans le cas de cisaillement du vent discontinu l'ordre de précision obtenu est de trois [25].
Dans la deuxième partie, l'investigation de l'instabilité barotrope de cisaillement du vent horizontal a était étudiée en utilisant les deux méthodes mentionnées ci-dessus. Nous nous sommes intéressés à la performance de ces deux méthodes en étudiant l'évolution de l'instabilité pour une longue durée sous l'effet de la non-linéarité, dans le cas simple du profile de Helmholtz.

Le problème linéaire associé est résolu analytiquement et la solution linéaire obtenue est utilisée comme condition initiale pour les simulations numériques ultérieures. On effectue une série de simulations numériques en utilisant les deux méthodes avec différente grilles et avec deux amplitudes différentes pour la perturbation initiale. Un terme de viscosité est ajouté dans l'équation de vorticité pour amortir les ondes à l'echelle de grille pour la méthode d'Arakawa. Ceci n'est pas nécessaire pour le schéma d'ordre supérieure ENO-4 qui a sa propre dissipation à l'échelle de grille. A haute résolution, les deux méthodes sont en bon accord; elles convergent qualitativement et quantitativement vers la même solution à long terme. Pour les petites perturbations l'écoulement total se stabilise dans un état stationnaire de cisaillement méridien avec un profile lisse prés de l'équateur tandis que pour les grandes perturbations, les vortex se fusionnent entre eux pour former un seul vortex à grande échelle qui se propage vers l'ouest, le long de l'équateur, qui est compatible avec les ondes d'est africaines et la circulation des moussons creusent. Pour la résolution grossière, la méthode d' Arakawa semble être plus performante que le schéma ENO-4 car elle fournit des solutions qui sont plus compatibles avec la résolution fine [26].

Abstract

In the first part of this dissertation, we use the Arakawa Jacobian method [1] and the fourth-order essentially non-oscillatory (ENO-4) scheme of Osher and Shu [41] to solve the equatorial beta-plane barotropic equations. The Arakawa Jacobian scheme is a second order centered finite difference scheme that conserves both energy and enstrophy. The fourth-order essentially non-oscillatory scheme is designed for the Hamilton-Jacobi equations and is traditionally used to track sharp fronts. We are interested in the performance of these two methods for solving the baratropic equations and determine whether they are adequate for studying the barotropic instability. The two methods are tested and compared on two typical exact solutions, a smooth Rossby wave-packet and a discontinuous shear on the long-climate scale of 100 days. The numerical results indicate that the Arakawa Jacobian method conserves energy and enstrophy nearly exactly in addition this method, captures the phase speed of the Rossby waveand achieves overall second order accuracy in both cases. The same properties are preserved by the ENO-4 scheme but the fourth order accuracy is observed only for the smooth Rossby wave solution while in the case of the discontinuous shear, it yields overall third order accuracy, even in the smooth regions, away from the discontinuity [25].

In the second part the barotropic instability of horizontal shear flows is investigated by using both methods mentioned above. We are interested in the performance of these two methods in tracking the long time behavior of the instability under the influence of the nonlinearity and in the simple case of a Helmholtz shear layer. The associated linear problem is solved analytically and the linear solution is used as an initial condition for the numerical simulations. We run a series of numerical simulations using both methods with several grids and with two different amplitudes of the initial

perturbation. A small viscosity term is added to the vorticity equation to damp the grid scale waves for Arakawa's method. This is not necessary for the high order ENO-4 scheme which has it own grid-scale dissipation. At high resolution, the two methods are in good agreement. They yield qualitatively and quantitatively the same solution in the long run. For small disturbances the total flow stabilizes into a steady state meridional shear with a smooth profile near the equator while strong disturbances merge together to form a single large-scale vortex that propagates westward, along the equator, consistent with the African easterly waves and the monsoons trough circulation. At coarse resolution, however, Arakawa's method seems to be much superior to the fourth order ENO-4 scheme as it provides solutions that are more consistent with the fine resolution one [26].

A mes parents,
A mon fils Rayane.

Acknowledgements

Ma reconnaissance va tout d'abord à mes directeurs de thèse, Aliziane Tarik et Khouider Boualem pour m'avoir encadré et aidé à mener à bien ce travail. Ma plus profonde gratitude va vers Khouider Boualem pour avoir proposé ce sujet de recherche et pour sa sympathie, sa patience, sa disponibilité et ses conseils. J'ai appris énormement grâce à lui, et je ne pense pas seulement aux problèmes mathématiques liés à la météorologie. Je le remercie chaleureusement pour son soutien continu dans les moments difficiles quand les maths ne marchaient pas. Enfin sa grandeur scientifique et sa gentillesse ont été pour moi de véritables atouts. Professeur Khouider : pour tous cela, un grand merci !

Je tiens encore à manifester ma plus profonde et sincère reconnaissance envers monsieur Aliziane Tarik pour m'avoir fait découverir les mathématiques appliquées, pour sa symphatie, son soutien et sa confiance. C'est grâce à ses encouragements que j'ai decidé de commencer cette thèse et je le remercie chaleureusement pour cela. Ses conseils sur les mathématiques et sur différents problèmes m'ont toujours aidé.

J'exprime mes sincères remerciements à monsieur le Professeur Teniou Djamel pour l'honneur qu'il me fait en acceptant de présider le jury de cette thèse.

Ma gratitude va également aux examinateurs. Je suis honoré par la présence dans mon jury des Professeurs Moulay Mohamed Said, Boulmezaoued Tahar et Hanoun Noureddine.

Je remercie de plus, toutes les personnes qui m'ont aidé durant la réalisation de cette thèse.

Contents

List of Figures

LIST OF FIGURES

List of Tables

Chapter 1

General Introduction

One important strategy for understanding general atmospheric circulation is the study of the numerical solutions of its governing equations. The equatorial beta-plane barotropic equations, a simple atmospheric model, have been studied for more than half a century and are at the heart of a hierarchy of more complex models. The first successful numerical weather prediction model, used by Charny *et al* in 1950 [9], was based on the barotropic vorticity equation (BVE). A barotropic atmosphere is a single-layered fluid; under this assumption there is no vertical component, and hence the equation to be solved is two dimensional (2D). For theoretical investigations of the evolution of vortices, atmospheric researchers are still using the barotropic assumption. For example, the BVE is useful for modelling the movement of tropical cyclones [8]. The barotropic assumption is also used to model global wave patterns in the middle troposphere [62]. To model tropical cyclones, the computational domain is a midlatitude β-plane. The β-plane approximation is a linear approximation to the Coriolis parameter found by a Taylor expansion [21] for a small displacement in latitude. Scale analysis shows that the nonlinear term is negligible. Most numerical models of the BVE use finite differences or spectral methods. A recent state of the art method from the applied mathematics [31] to the problem of tropical climate modelling [28] showed that a non-oscillatory central scheme can accurately model equatorial waves without undue dissipation of energy but seems to suffer some serious shortcoming [11, 28] (see conclusion section). However, the Arakawa Jacobian scheme [1], which is specifically designed for the incompressible BVE, is widely used in the atmosphere-ocean community. The Arakawa Jacobian has the useful feature that both domain integrated enstrophy and

domain integrated kinetic energy are conserved. It also conserves mean wavenumber; this prevents nonlinear instabilities from occurring. A third method which may be adapted to solve the incompressible BVE is the high-order essentially non-oscillatory scheme (ENO) of Osher and Shu [41]. The ENO scheme is a high order accurate finite difference scheme designed for problems with piecewise smooth solutions containing discontinuities. ENO schemes are traditionally used for hyperbolic conservation laws and Hamilton-Jacobi equations [41]. The key idea lies at the approximation level, where a nonlinear adaptive procedure is used to automatically choose the locally smoothest stencil, hence avoiding crossing discontinuities in the interpolation procedure as much as possible. ENO schemes have been quite successful in applications, especially for problems containing both shocks and complicated smooth solution structures, such as compressible turbulence simulations and aeroacoustic. The objective of this numerical solution of the barotropic system by the two methods described in Chapters 4 and 5 of this dissertation is a search for an adequate numerical method to study the barotropic instability on the equatorial beta-plane. This is pursued in Chapter 6 and 7.

The fundamental instability mechanisms for large scale atmospheric flows are the baroclinic and barotropic instabilities. The baroclinic instability is of primary importance at middle and high latitudes while the barotropic instability appears to be of central importance in the tropics. As noted by Lindzen and Tung [35], both instabilities have fundamentally the same origin: the conservation of potential vorticity. In the barotropic atmospheres, the vertical variations of the flow are ignored completely and the linearized 2d vorticity equation reduces to an ordinary differential equation in which the South-to-North coordinate y is the independent variable [14, 30]. Under such conditions the source of kinetic energy perturbation is solely the kinetic energy of the zonal basic flow. In the case of purely baroclinic atmospheres, the y variations of the flow are ignored completely, at least in the basic flow. The exclusive source of energy perturbation is the available potential energy inherent in the vertical shear of the zonal basic flow.

The barotropic instability propagates horizontally and chiefly transports momentum while the pure baroclinic instability propagates vertically and transports heat. Over the last three decades the study of these instabilities has been an important goal for Dynamic Meteorology since the baroclinic instability is the main source for midlatitude

synoptic-scale disturbances, i.e., weather systems. While the most general currents in the ocean and atmosphere have both horizontal and vertical shear, the existence of strong horizontal shear in the ocean and atmosphere suggests that in this circumstances barotropic instability may be important.

The stability of parallel shear flow was initially considered in the nineteenth century. Piecing flow profiles from straight lines, Rayleigh [47, 48] obtained analytic solutions for a variety of cases, including shear layers and jets, with and without zonal boundaries. He also derived a necessary condition for instability based on the occurrence of an inflection point in the velocity distribution [49]. A second necessary condition for instability of parallel shear flows was derived by Fjortoft [12]. The stability of parallel shear flows in the presence of a variable Coriolis parameter was first studied by Kuo [30]. The stability of parallel shear flows on the β-plane was also investigated by Howard and Drazin [22] who found analytic solutions for simple flow profiles and a neutral stability curve for the Helmholtz shear layer.

The objective of the present study is to investigate the non-linear effects of the barotropic shear instability in the equatorial beta-plane using two numerical methods mentioned above : the Arakawa Jacobian and a fourth-order ENO scheme of Osher and Shu. Our strategy consists in choosing a simple Helmholtz shear layer that can be easily analyzed linearly on the equatorial beta-plane. The unstable mode is then used to feed the numerical simulations in order to understand and analyze the effects of the shear instability on the environmental flow. Previous numerical studies of the barotropic instability were focussed on the wave-wave and wave-mean flow interactions. Moreover, in the non-linear saturation limits of the instability [40, 54, 55, 56], the numerical solution was mostly used to confirm and validate theoretical prediction. In contrast, here we are mostly interested in the performance and efficiency of the these numerical methods in tracking the long time behaviour of the physical solution.

The plan for the dissertation is as follows. First we present the barotropic equations on the equatorial β-plane. Next we give results for the existence and the uniqueness of solutions to the barotropic equations in a 2D channel. Next we study the numerical methods needed for solving the equatorial beta-plane barotropic equations. The Arakawa Jacobian is used together with a second-order numerical solution of the Poisson equation, which is used to enforce the incompressibility constraint. The fourth-order essentially non-oscillatory (ENO-4) scheme is coupled with a fourth-order Poisson solver.

Next We validate the numerical methods. The main contribution of this work is an examination of the performance of these two methods in tracking the longtime behaviour of the instability under the influence of the nonlinearity in the case of a Helmholtz shear layer. This is the subject of Chapters 6 and 7.

Chapter 2

Barotropic equations

2.1 Introduction

In this chapter we present the barotropic equations in an equatorial β-plane. These equations are a simple atmospheric model which was used to make the first successful numerical weather predictions in the early 1950s. In our study of the barotropic instability, we shall be concerned with atmospheric motion near the equator. The physical basis for using this equations to study the numerical barotropic instability in the equatorial beta plane is developed in the next sections.

2.2 Rotating fluid

The study of rotating fluids is particularly important for the understanding of atmospheric and oceanic flows. Indeed, the flows in the atmosphere and ocean observed from the surface of the earth are made in a rotating frame with angular velocity $\mathbf{\Omega}$ of local rotation thereof, so they are strongly influenced by this rotation. The Earth rotates eastward around the axis of its poles. It performs one full turn (2π radians) in a sidereal day, or 86164seconds (and not $24 \times 3600s = 86400s$). Therefore the angular velocity of rotation of the earth is $\Omega_{Earth} = \frac{2\pi rad}{86164sec} = 7,29 \times 10^{-5} rad \times s^{-1}$. For more details are given in "An Introduction to Fluid Dynamics" of G.K, Batchelor [4], and "Atmospheric and Oceanic Fluid Dynamic, Fundamentals and Large-scale Circulation " of Geoffrey K. Vallis [61].

2.2.1 Equation of motion of a fluid in the rotating frame

We start from the equation of motion in an inertial, non-rotating frame of reference (Navier Stokes equation) to derive the equation of motion in a rotating frame of reference at the angular velocity $\mathbf{\Omega}$. ($\mathbf{\Omega}$ is parallel to the axis of rotation). We note $\mathbf{v_i}$ the fluid velocity in an inertial, non-rotating frame of reference and $\mathbf{v_r}$ the fluid velocity in the rotating frame: the velocities are measured at a point M with $OM = r$ (O is the origin of both coordinate systems, and is located on the axis of rotation). Consider first a vector C of constant length rotating relative to an inertial frame at a constant angular velocity $\mathbf{\Omega}$. Then, in a frame rotating with that same angular velocity it appears stationary and constant. If in a small interval of time δt the vector C under goes a rotation of small angle $\delta\lambda$, then the change in C as perceived in the inertial frame, is given by (see Fig. 2.1).

$$\delta C = |C| \cos\theta \ \delta\lambda \mathbf{m} \tag{2.1}$$

where the vector $\mathbf{m}$ is the unit vector in the direction of change of C which is perpendicular to both C and $\mathbf{\Omega}$**.** But the rate of change of the angle is just, by definition, the angular velocity so that $\delta\lambda = |\mathbf{\Omega}|\,\delta t$ and

$$\delta C = |C|\,|\mathbf{\Omega}| \sin\varphi \ \mathbf{m}\delta t = \mathbf{\Omega} \wedge \mathbf{C}\delta t \tag{2.2}$$

Using the definition of the vector cross product, where $\varphi = \left(\frac{\pi}{2} - \theta\right)$ is the angle between $\mathbf{\Omega}$ and C, we get

$$\left(\frac{dC}{dt}\right)_{\mathbf{I}} = \mathbf{\Omega} \wedge \mathbf{C}, \tag{2.3}$$

where the left hand side is the rate of change of C as perceived in the inertial frame. Let us denoted by $\{e_x, e_y, e_z\}$ the basis vectors of the inertial frame and by $\{e'_x, e'_y, e'_z\}$ those of the rotating frame. According to (2.3), the particular derivative of the basis vectors $\{e'_x, e'_y, e'_z\}$ is

$$\frac{de'_x}{dt} = \mathbf{\Omega} \wedge e'_x, \quad \frac{de'_y}{dt} = \mathbf{\Omega} \wedge e'_y, \quad \frac{de'_z}{dt} = \mathbf{\Omega} \wedge e'_z,$$

Any vector A can be described in the two frames as

$$\begin{aligned} A &= A_x \ e_x + A_y \ e_y + A_z \ e_z \\ &= A'_x \ e'_x + A'_y \ e'_y + A'_z \ e'_z \end{aligned}$$

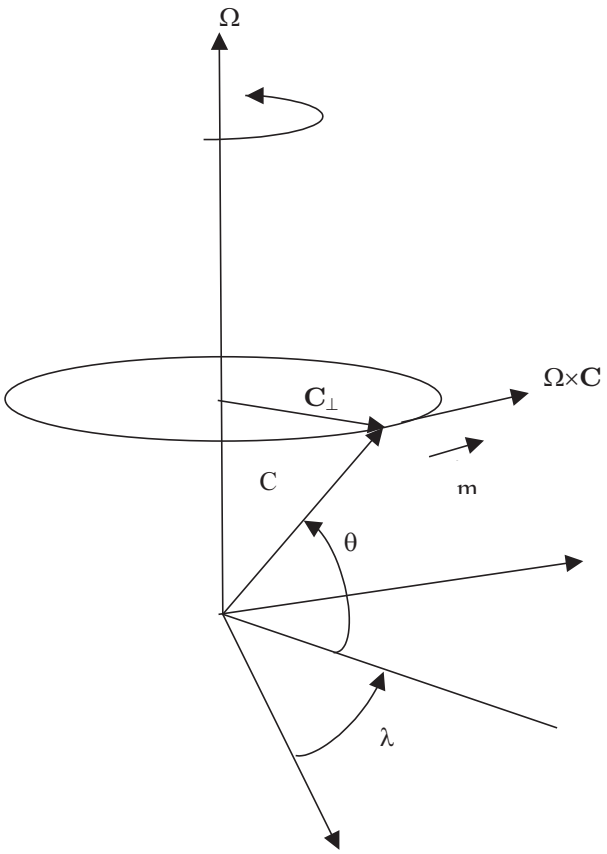

Figure 2.1: A vector C rotating at an angular velocity Ω. It appears to be a constant vector in the rotating frame, where as in the inertial frame it evolves according to $\left(\frac{dC}{dt}\right)_{\mathbf{i}} = \mathbf{\Omega} \wedge C$

its derivative with respect to time is

$$\begin{aligned}
\left(\frac{dA}{dt}\right)_{\mathbf{i}} &= \dot{A}_x e_x + \dot{A}_y\ e_y + \dot{A}_z\ e_z \\
&= \dot{A}'_x\ e'_x + \dot{A}'_y e'_y + \dot{A}'_z\ e'_z + A'_x\ \dot{e}'_x + A'_y\ \dot{e}'_y + A'_z\ \dot{e}'_z \\
&= \left(\frac{dA}{dt}\right)_{\mathbf{r}} + \mathbf{\Omega} \wedge \left(A'_x\ e'_x + A'_y\ e'_y + A'_z\ e'_z\right) \\
&= \left(\frac{dA}{dt}\right)_{\mathbf{r}} + \mathbf{\Omega} \wedge A
\end{aligned}$$

Then the temporal variations in the inertial frame and in the rotating frame for any

vector field $A(r)$ are related by the relation:

$$\left(\frac{dA}{dt}\right)_{\mathbf{i}} = \left(\frac{dA}{dt}\right)_{\mathbf{r}} + \mathbf{\Omega} \wedge A \tag{2.4}$$

In particular, if $A = r$ the position vecteur, we get the velocity

$$\mathbf{v_i} = \mathbf{v_r} + \mathbf{\Omega} \wedge r \tag{2.5}$$

This formula allows us to compare the velocity of the same object in both frames. Applying again equation (2.4) in the previous expression of $\mathbf{v_i}$, we obtain

$$\begin{aligned}
\left(\frac{d\mathbf{v_i}}{dt}\right)_{\mathbf{i}} &= \left(\frac{d\mathbf{v_i}}{dt}\right)_{\mathbf{r}} + \mathbf{\Omega} \wedge \mathbf{v_i} \\
&= \left(\frac{d\left(\mathbf{v_r} + \mathbf{\Omega} \wedge r\right)}{dt}\right)_{\mathbf{r}} + \mathbf{\Omega} \wedge \left(\mathbf{v_r} + \mathbf{\Omega} \wedge r\right) \\
&= \frac{d\mathbf{v_r}}{dt} + \mathbf{\Omega} \wedge \left(\frac{dr}{dt}\right)_{\mathbf{r}} + \mathbf{\Omega} \wedge \mathbf{v_r} + \mathbf{\Omega} \wedge \left(\mathbf{\Omega} \wedge r\right) \\
&= \frac{d\mathbf{v_r}}{dt} + \mathbf{\Omega} \wedge \mathbf{v_r} + \mathbf{\Omega} \wedge \mathbf{v_r} + \mathbf{\Omega} \wedge \left(\mathbf{\Omega} \wedge r\right) \\
&= \frac{d\mathbf{v_r}}{dt} + 2\mathbf{\Omega} \wedge \mathbf{v_r} + \mathbf{\Omega} \wedge \left(\mathbf{\Omega} \wedge r\right)
\end{aligned} \tag{2.6}$$

We can show that

$$\mathbf{\Omega} \wedge \left(\mathbf{\Omega} \wedge r\right) = -\frac{1}{2} \nabla \left(\mathbf{\Omega} \wedge r\right)^2 .$$

The Navier-Stokes equation in the inertial frame is

$$\left(\frac{d\mathbf{v_i}}{dt}\right)_{\mathbf{i}} = \frac{\partial \mathbf{v_i}}{\partial t} + \left(\mathbf{v_i} \cdot \nabla\right) \mathbf{v_i} = -\frac{1}{\rho} \nabla p + \upsilon \Delta \mathbf{v_i} + \nabla \phi \tag{2.7}$$

(where ϕ represents the potential of volumic forces per unit mass, e.g. $\phi = gz$ for the gravity forces). Applying Relation (2.6) to the previous equation, we obtain:

$$\frac{d\mathbf{v_r}}{dt} + 2\mathbf{\Omega} \wedge \mathbf{v_r} - \frac{1}{2} \nabla \left(\mathbf{\Omega} \wedge r\right)^2 = -\frac{1}{\rho} \nabla p + \upsilon \Delta \left(\mathbf{v_r} + \mathbf{\Omega} \wedge r\right) + \nabla \phi.$$

Since

$$\frac{d\mathbf{v_r}}{dt} = \frac{\partial \mathbf{v_r}}{\partial t} + \left(\mathbf{v_r} \nabla\right) \mathbf{v_r}$$

and

$$\Delta \left(\mathbf{\Omega} \wedge r\right) = 0$$

because $\left(\mathbf{\Omega} \wedge \mathbf{r}\right)$ is a linear function of the components of $\mathbf{r}$, we obtain

$$\frac{d\mathbf{v_r}}{dt} \equiv \frac{\partial \mathbf{v_r}}{\partial t} + \left(\mathbf{v_r} \cdot \nabla\right) \mathbf{v_r} = -\frac{1}{\rho} \nabla p + \upsilon \Delta \mathbf{v_r} + \nabla \phi - 2\mathbf{\Omega} \wedge \mathbf{v_r} + \frac{1}{2} \nabla \left(\mathbf{\Omega} \wedge r\right)^2 .$$

Thus we obtain the Navier-Stokes equation in the rotating frame, droping the subscript **r** we get

$$\frac{d\mathbf{v}}{dt} = \frac{\partial \mathbf{v}}{\partial t} + (\mathbf{v}\cdot\nabla)\,\mathbf{v} = -\frac{1}{\rho}\nabla p + \upsilon\Delta\mathbf{v} + \nabla\phi - 2\boldsymbol{\Omega}\wedge\mathbf{v} + \frac{1}{2}\nabla\left(\boldsymbol{\Omega}\wedge r\right)^2. \tag{2.8}$$

Here, $2\boldsymbol{\Omega}\wedge\mathbf{v}$ is the Coriollis force and it is perpendicular to both the velocity $\mathbf{v}$ in the rotating frame and $\boldsymbol{\Omega}$. The term $\frac{1}{2}\nabla\left(\boldsymbol{\Omega}\wedge r\right)^2$ is the centrifugal force and it acts as a volume force.

2.2.2 Equation of motion of a fluid in spherical coordinates

The Earth is nearly spherical and it might appear obvious that we should cast our equations in spherical coordinates. The location of a point is given by the coordinates (λ,θ,r) where λ is the angular distance eastwards (i.e., longitude), θ the angular distance polewards (i.e., latitude) and r the radial distance to the Earth center (see Fig. 2.2). If a is the Earth radius of the , then we define $z = r - a$. At a given location we may also define the Cartesian increments (dx,dy,dz) =$(r\cos\theta d\lambda$, $rd\theta$,$dr)$. For a scalar quantity ϕ the material derivative in spherical coordinates is

$$\frac{d\phi}{dt} = \frac{\partial\phi}{\partial t} + \frac{u}{r\cos\theta}\frac{\partial\phi}{\partial\lambda} + \frac{v}{r}\frac{\partial\phi}{\partial\theta} + w\frac{\partial\phi}{\partial r} \tag{2.9}$$

where the velocity components corresponding to the coordinates (λ,θ,r) are

$$(u,v,w) = \left(r\cos\theta\frac{d\lambda}{dt}, r\frac{d\theta}{dt}, \frac{dr}{dt}\right) \tag{2.10}$$

That is, u is the zonal velocity, v is the meridional velocity and w is the vertical velocity. If we define $(\mathbf{i},\mathbf{j},\mathbf{k})$ to be the unit vectors in the direction of increasing (λ,θ,r) then

$$\mathbf{v} = u\mathbf{i}+v\mathbf{j}+w\mathbf{k}$$

The divergence of a vector $B = B^\lambda\mathbf{i}+B^\theta\mathbf{j}+B^r\mathbf{k}$ is

$$\operatorname{div} B = \frac{1}{\cos\theta}\left[\frac{1}{r}\frac{\partial B^\lambda}{\partial\lambda} + \frac{1}{r}\frac{\partial\left(B^\phi\cos\theta\right)}{\partial\theta} + \frac{\cos\theta}{r^2}\frac{\partial\left(r^2B^r\right)}{\partial r}\right] \tag{2.11}$$

The gradient of a scalar is

$$\nabla\psi = \frac{1}{r\cos\theta}\frac{\partial\psi}{\partial\lambda}\mathbf{i}+\frac{1}{r}\frac{\partial\psi}{\partial\theta}\mathbf{j}+\frac{\partial\psi}{\partial r}\mathbf{k} \tag{2.12}$$

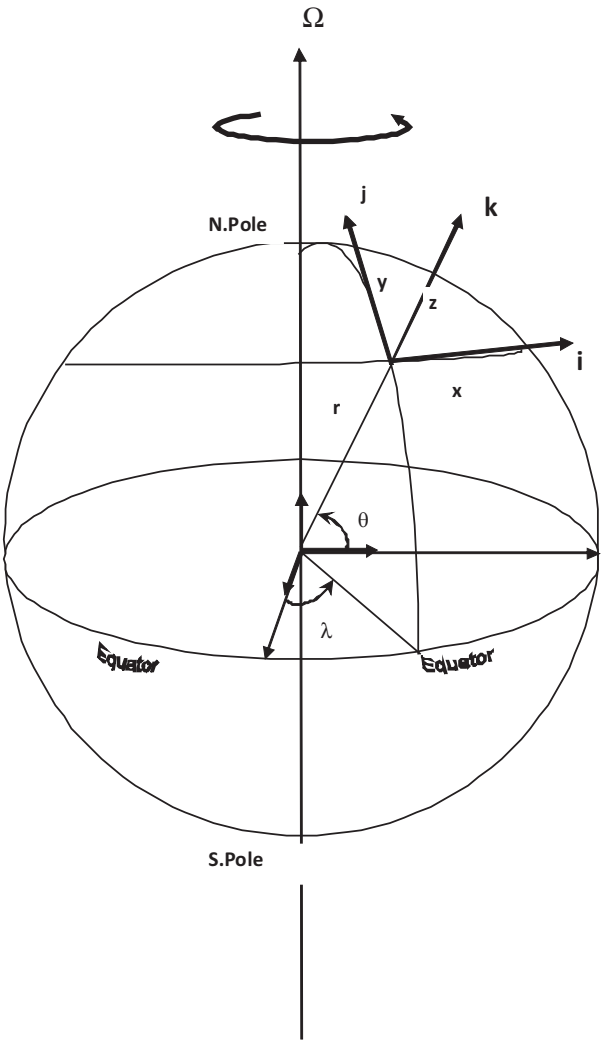

Figure 2.2: The spherical coordinate system. The orthogonal unit vectors $(\mathbf{i}, \mathbf{j}, \mathbf{k})$ point in the direction of increasing longitude λ , latitude θ, and altitude z. Locally, one may apply a Cartesian system with variables x, y and z measuring distances along i, j and k.

The Laplacien of a scalar is

$$\Delta\psi = \frac{1}{r^2\cos\theta}\left[\frac{1}{\cos\theta}\frac{\partial^2\psi}{\partial\lambda^2} + \frac{\partial}{\partial\theta}\left(\cos\theta\frac{\partial\psi}{\partial\theta}\right) + \cos\theta\frac{\partial}{\partial r}\left(r^2\frac{\partial\psi}{\partial r}\right)\right] \tag{2.13}$$

Recall that the inviscid momentum equation in (2.8) (Euler equation) is

$$\frac{d\mathbf{v}}{dt} + 2\boldsymbol{\Omega}\wedge\mathbf{v} = -\frac{1}{\rho}\nabla p - \mathbf{g}. \tag{2.14}$$

where ($\mathbf{g} = \nabla\Phi$ and $\Phi = gz + \frac{1}{2}(\boldsymbol{\Omega}\wedge r)^2$) is an 'effective geopotential' function. In spherical coordinates, the direction of the coordinate axes change with position and so the component expansion of (2.14) is

$$\frac{d\mathbf{v}}{dt} = \frac{du}{dt}\mathbf{i}+\frac{dv}{dt}\mathbf{j}+\frac{dw}{dt}\mathbf{k}+u\frac{d\mathbf{i}}{dt}+v\frac{d\mathbf{j}}{dt} + w\frac{d\mathbf{k}}{dt} \tag{2.15}$$

or

$$\frac{d\mathbf{i}}{dt} = \Omega_{flow}\wedge\mathbf{i},\quad \frac{d\mathbf{j}}{dt} = \Omega_{flow}\wedge\mathbf{j},\quad \frac{d\mathbf{k}}{dt} = \Omega_{flow}\wedge\mathbf{k}$$

where Ω_{flow} is the total rotation rate of a vector that moves whith the flow given by

$$\Omega_{flow} = -\frac{v}{r}\mathbf{i}+\frac{u}{r}\mathbf{j}+\frac{u\tan\theta}{r}\mathbf{k} \tag{2.16}$$

For details for the equation (2.16) see [61] page 52 chapter two.

Then (2.15) becomes

$$\frac{d\mathbf{v}}{dt} = \frac{du}{dt}\mathbf{i}+\frac{dv}{dt}\mathbf{j}+\frac{dw}{dt}\mathbf{k}+\Omega_{flow}\wedge\mathbf{v} \tag{2.17}$$

using the expression of $\Omega_{flow}\wedge\mathbf{v}$ in (2.17), we obtain,

$$\frac{d\mathbf{v}}{dt} = \left(\frac{du}{dt} - \frac{uv\tan\theta}{r} + \frac{uw}{r}\right)\mathbf{i}+\left(\frac{dv}{dt} + \frac{u^2\tan\theta}{r} + \frac{vw}{r}\right)\mathbf{j}+\left(\frac{dw}{dt} - \frac{u^2+v^2}{r}\right)\mathbf{k} \tag{2.18}$$

using the definition of a vector cross product the Coriolis term in (2.14) is

$$\begin{aligned} 2\boldsymbol{\Omega}\wedge\mathbf{v} &= \begin{vmatrix} \mathbf{i} & \mathbf{j} & \mathbf{k} \\ 0 & 2\Omega_{Earth}\cos\theta & 2\Omega_{Earth}\sin\theta \\ u & v & w \end{vmatrix} \\ &= \left(2w\Omega_{Earth}\cos\theta - 2v\Omega_{Earth}\sin\theta\right)\mathbf{i}+\left(2u\Omega_{Earth}\sin\theta\right)\mathbf{j}-\left(2u\Omega_{Earth}\cos\theta\right)\mathbf{k} \end{aligned} \tag{2.19}$$

using((2.18) and (2.19), and the gradient operateur given by (2.12), the momentum equation ((2.14) becomes

$$\begin{cases} \dfrac{du}{dt} - \left(2\Omega_{Earth} + \dfrac{u}{r\cos\theta}\right)(v\sin\theta - w\cos\theta) & = -\dfrac{1}{\rho r\cos\theta}\dfrac{\partial p}{\partial\lambda} \\ \dfrac{dv}{dt} + \dfrac{uw}{r} + \left(2\Omega_{Earth} + \dfrac{u}{r\cos\theta}\right)(u\sin\theta) & = -\dfrac{1}{\rho r}\dfrac{\partial p}{\partial\theta} \\ \dfrac{dw}{dt} - \dfrac{u^2+v^2}{r} - 2\Omega_{Earth}\cos\theta & = -\dfrac{1}{\rho}\dfrac{\partial p}{\partial r} - \mathbf{g} \end{cases} \tag{2.20}$$

The term involving Ω_{Earth} are called Coriolis terms and the quadratic term on the left hand side involving $\dfrac{1}{r}$ are often called metric terms.

2.2.3 The primitive equations

The so-called primitive equation of motion are simplification of the above equations frequently used in atmosphere and oceanic modelling. three related approximation are involved

(i) **The Hydrostatic approximation.** In the vertical momentum equation, the gravitational term is assumed to be balanced by the pressure gradient term, so that

$$\frac{\partial p}{\partial z} = -\rho g \tag{2.21}$$

The advection of vertical velocity, the Coriolis terms, and the metric term $\dfrac{(u^2+v^2)}{r}$ are all neglected.

(ii) **The shallow fluid approximation.** We write $r = a + z$ where the constant a is the radius of the Earth and z increases in the radial direction. The coordinate r is then replaced by a except where it is used as the differentiating argument.

(iii) **The traditional approximation.** The Coriolis term in the horizontal momentum equations involving the vertical velocity and the still smaller metric $\dfrac{uv}{r}$ and $\dfrac{vw}{r}$, are neglected.

Making these approximations, the momentum equations (2.20) become

$$\begin{cases} \dfrac{du}{dt} - fv - \dfrac{uv}{a}\tan\theta & = -\dfrac{1}{\rho a\cos\theta}\dfrac{\partial p}{\partial\lambda} \\ \dfrac{dv}{dt} + fu + \dfrac{u^2}{a}\tan\theta & = -\dfrac{1}{\rho a}\dfrac{\partial p}{\partial\theta} \\ 0 & = -\dfrac{1}{\rho}\dfrac{\partial p}{\partial z} - \mathbf{g} \end{cases} \tag{2.22}$$

where

$$\frac{d}{dt} = \left(\frac{\partial}{\partial t} + \frac{u}{a\cos\theta}\frac{\partial}{\partial \lambda} + \frac{v}{a}\frac{\partial}{\partial \theta} + w\frac{\partial}{\partial z} \right)$$

and $f = 2\Omega_{Earth}\sin\theta$ is called the Coriolis parameter.

2.2.4 Cartesian approximations: the tangent plane

2.2.4.1 The f-plane

Although the rotation of the Earth is central for many dynamical phenomena, the sphericity of the Earth is not always so. This is especially true for phenomena on a scale somewhat smaller than global where the use of spherical coordinates become awkward, and it is more convenient to use a locally Cartesian representation of the equations.

We will define a plane tangent to the surface of the Earth at a latitude θ_0, and then use the cartesian coordinate system (x, y, z) to describe motion on that plane. For a small displacement along the plane, $(x, y, z) \approx (a\lambda\cos\theta_0, a(\theta - \theta_0), z)$. The velocity is $\mathbf{v} = (u,v,w)$, so that u,v,w are the components of the velocity in the tangent plane, in approximately the east-west, north-south and vertical directions, respectively. The flow momentum equations for in this plane are then expressed as

$$\begin{cases} \dfrac{\partial u}{\partial t} + (\mathbf{v}\cdot\nabla)u + 2(\Omega^y w - \Omega^z v) & = -\dfrac{1}{\rho}\dfrac{\partial p}{\partial x} \\ \dfrac{\partial v}{\partial t} + (\mathbf{v}\cdot\nabla)v + 2(\Omega^z u - \Omega^x w) & = -\dfrac{1}{\rho}\dfrac{\partial p}{\partial y} \\ \dfrac{\partial w}{\partial t} + (\mathbf{v}\cdot\nabla)w + 2(\Omega^x v - \Omega^y u) & = -\dfrac{1}{\rho}\dfrac{\partial p}{\partial z} - \mathbf{g} \end{cases} \tag{2.23}$$

where the rotation vector $\mathbf{\Omega} = \Omega^x\mathbf{i} + \Omega^y\mathbf{j} + \Omega^z\mathbf{k}$ and $\Omega^x = 0$, $\Omega^y = \Omega_{Earth}\cos\theta_0$ and $\Omega^z = \Omega_{Earth}\sin\theta_0$. If we make the traditional approximation, and so ignore the component of $\mathbf{\Omega}$ not in the local vertical direction, then

$$\begin{cases} \dfrac{\partial u}{\partial t} + (\mathbf{v}\cdot\nabla)u - f_0 v & = -\dfrac{1}{\rho}\dfrac{\partial p}{\partial x} \\ \dfrac{\partial v}{\partial t} + (\mathbf{v}\cdot\nabla)v + f_0 u & = -\dfrac{1}{\rho}\dfrac{\partial p}{\partial y} \\ \dfrac{\partial w}{\partial t} + (\mathbf{v}\cdot\nabla)w & = -\dfrac{1}{\rho}\dfrac{\partial p}{\partial z} - \mathbf{g} \end{cases} \tag{2.24}$$

where $f_0 = 2\Omega^z = 2\Omega\sin\theta_0$. Defining the horizontal velocity vector $\mathbf{u} = (u, v, 0)$ the first two equation in (2.24) may also written as

$$\frac{d\mathbf{u}}{dt} + \mathbf{f}_0 \wedge \mathbf{u} = -\frac{1}{\rho}\nabla_z p$$

where $\frac{d\mathbf{u}}{dt} = \frac{\partial \mathbf{u}}{\partial t} + \mathbf{v}\cdot\nabla\mathbf{u}$, $\mathbf{f}_0 = 2\Omega\sin\theta_0\mathbf{k} = f_0\mathbf{k}$,$\nabla_z = \left(\frac{\partial}{\partial x}, \frac{\partial}{\partial y}, 0\right)$ and $\mathbf{k}$ is perpendicular to the plane (it does not change its orientation with latitude). This equations, describe the flow on the surface of a rotating sphere with a good approximation provided the flow is of limited latitudinal extent so that the effects of sphericity are unimportant; we have made what is known as the f-plane approximation since the Coriolis parameter is a constant. We may in addition make the hydrostatic approximation in wich case (2.24) becomes:

$$\begin{cases} \frac{\partial u}{\partial t} + u\frac{\partial u}{\partial x} + v\frac{\partial u}{\partial y} + w\frac{\partial u}{\partial z} - f_0 v = -\frac{1}{\rho}\frac{\partial p}{\partial x}, \\ \frac{\partial u}{\partial t} + u\frac{\partial v}{\partial x} + v\frac{\partial v}{\partial y} + w\frac{\partial v}{\partial z} + f_0 u = -\frac{1}{\rho}\frac{\partial p}{\partial y} \\ 0 = -\frac{1}{\rho}\frac{\partial p}{\partial z} - \mathbf{g}. \end{cases} \tag{2.25}$$

2.2.4.2 The β-plane approximation

The magnitude of the vertical component of rotation varies with latitude, and this has important dynamical consequences. We can approximate this effect by allowing the effective rotation vector to vary. Thus, noting that for a small latitude variation,

$$f = 2\Omega_{Earth}\sin\theta = 2\Omega_{Earth}\sin\theta_0 + 2\Omega_{Earth}\left(\theta - \theta_0\right)\cos\theta_0 \tag{2.26}$$

then on the tangent plane, we may mimic this by allowing the Coriolis parameter to vary linearly

$$f = f_0 + \beta y \tag{2.27}$$

where $f_0 = 2\Omega_{Earth}\sin\theta_0$ and $\beta = \frac{\partial f}{\partial y} = \frac{2\Omega_{Earth}\cos\theta_0}{a}$. This important approximation is known as the β-plane, approximation; it captures the most important dynamical effects of sphericity, without complicated geometric effects which are not essential for many phenomena. The momentum Equations (2.24) are unaltered except that f_0 is replaced by $f = f_0 + \beta y$ to represent a varying Coriolis parameter. The momentum Equations for the flow in the β-plane are then:

$$\begin{cases} \frac{\partial u}{\partial t} + \left(\mathbf{v}\cdot\nabla\right)u - fv &= -\frac{1}{\rho}\frac{\partial p}{\partial x} \\ \frac{\partial v}{\partial t} + \left(\mathbf{v}\cdot\nabla\right)v + fu &= -\frac{1}{\rho}\frac{\partial p}{\partial y} \\ \frac{\partial w}{\partial t} + \left(\mathbf{v}\cdot\nabla\right)w &= -\frac{1}{\rho}\frac{\partial p}{\partial z} - \mathbf{g} \end{cases} \tag{2.28}$$

We write the β-plane horizontal momentum equations:

$$\frac{d\mathbf{u}}{dt} + \mathbf{f} \wedge \mathbf{u} = -\frac{1}{\rho}\nabla_z p \tag{2.29}$$

where $\mathbf{f} = (f_0 + \beta y)\,\mathbf{k}$. In the component form this equation becomes

$$\begin{cases} \dfrac{\partial u}{\partial t} + u\dfrac{\partial u}{\partial x} + v\dfrac{\partial u}{\partial y} + w\dfrac{\partial u}{\partial z} - fv = -\dfrac{1}{\rho}\dfrac{\partial p}{\partial x}, \\ \dfrac{\partial u}{\partial t} + u\dfrac{\partial v}{\partial x} + v\dfrac{\partial v}{\partial y} + w\dfrac{\partial v}{\partial z} + fu = -\dfrac{1}{\rho}\dfrac{\partial p}{\partial y} \end{cases} \tag{2.30}$$

2.2.5 Geostrophic Flow

We see, then, that the principal difference that rotation is likely to make to the flow of a homogeneous fluid is in the action of the Coriolis acceleration. An important class of flows is obtained when motion is dominated by the Coriolis force. Consider a steady flow in which the Coriolis effect is large compared with both the inertia of the relative motion and viscous forces. This means that

$$|(\mathbf{v}\,\mathrm{grad})\,\mathbf{v}| << |\mathbf{\Omega} \wedge \mathbf{v}| \;\text{ and }\; |\upsilon\Delta\mathbf{v}| << |\mathbf{\Omega} \wedge \mathbf{v}| \;. \tag{2.31}$$

The ratios of these terms can be expressed in terms of dimensionless numbers, measured with respect to typical length and velocity scales, L and U as:

$$(\mathbf{v}\,\mathrm{grad})\,\mathbf{v} \approx \frac{U^2}{L}\;,\; \mathbf{\Omega} \wedge \mathbf{v} \approx \mathbf{\Omega}U \;\text{ and }\; \upsilon\Delta\mathbf{v} \approx \frac{\upsilon U}{L^2} \tag{2.32}$$

$$\frac{|(\mathbf{v}\,\mathrm{grad})\,\mathbf{v}|}{|\mathbf{\Omega} \wedge \mathbf{v}|} \approx \frac{U}{\mathbf{\Omega}L} = R_0 \tag{2.33}$$

$$\frac{|\upsilon\Delta\mathbf{v}|}{|\mathbf{\Omega} \wedge \mathbf{v}|} \approx \frac{\upsilon}{\mathbf{\Omega}L^2} = Ek \tag{2.34}$$

where R_0 is the Rossby number and Ek is the Ekman number respectively. A small Rossby number means a system which is strongly affected by Coriolis forces, and a large Rossby number means a system in which inertial forces dominate. However under the conditions $R_0 << 1$ and $Ek << 1$, the viscous and convective terms drop out, and the pressure terms balances the Coriolis force. Then the Navier-stokes equaion (2.8) simplifies to

$$2\mathbf{\Omega} \wedge \mathbf{v} \approx -\frac{1}{\rho}\,\mathrm{grad}\,p. \tag{2.35}$$

Flows in which this force balance between the Coriolis effects and the pressure gradient is dominant are called geostrophic flows.

2.3 Equatorial β-plane

A long the equator (latitude $\theta = 0\circ$), the Coriolis parameter $f = 2\Omega_{Earth} \sin\theta$ vanishes. Without a Coriolis force, currents cannot be maintained in geostrophic balance, and we expect dramatic dynamical differences between tropical and extratropical regions. The first question is the determination of the meridional extent of the tropical region where these special effects can be expected. It is most natural here to choose the equator as the origin of the meridional axis. The beta-plane approximation to the Coriolis parameter (see subsection 2.2.3 above) then yields $f = \beta y$ where y measures the meridional distance from the equator (positive northward) and $\beta = 2\Omega_{Earth}/a = 2.28 \times 10^{-11} m - 1.s - 1$ with Ω_{Earth} and a being, the earths angular rotation rate and radius ($\Omega_{Earth} = 7.29 \times 10^{-5} s^{-1}, a = 6371 km$) respectively. This representation of the Coriolis parameter bears the name of equatorial beta-plane approximation.

2.4 Equations governing geophysical flows

The geophysical flows equations, sometimes called primitive equations govern the motion of the ocean and of the atmosphere and they are derived from the general conservation laws of physics using the Boussinesq and hydrostatic approximations. They include: the conservation of horizontal momentum equation, the hydrostatic equation, the continuity equation, the equation for the density. These equations read

$$\begin{cases} \dfrac{\partial u}{\partial t} + u\dfrac{\partial u}{\partial x} + v\dfrac{\partial u}{\partial y} + w\dfrac{\partial u}{\partial z} - fv = -\dfrac{1}{\rho_0}\dfrac{\partial p}{\partial x} + \dfrac{\partial}{\partial x}\left(\mathcal{A}\dfrac{\partial u}{\partial x}\right) + \dfrac{\partial}{\partial y}\left(\mathcal{A}\dfrac{\partial u}{\partial y}\right) + \dfrac{\partial}{\partial z}\left(\nu_E\dfrac{\partial u}{\partial z}\right) \\ \dfrac{\partial v}{\partial t} + u\dfrac{\partial v}{\partial x} + v\dfrac{\partial v}{\partial y} + w\dfrac{\partial v}{\partial z} + fu = -\dfrac{1}{\rho_0}\dfrac{\partial p}{\partial y} + \dfrac{\partial}{\partial x}\left(\mathcal{A}\dfrac{\partial v}{\partial x}\right) + \dfrac{\partial}{\partial y}\left(\mathcal{A}\dfrac{\partial v}{\partial y}\right) + \dfrac{\partial}{\partial z}\left(\nu_E\dfrac{\partial v}{\partial z}\right) \\ 0 = \dfrac{\partial p}{\partial z} - \rho g \\ \dfrac{\partial u}{\partial x} + \dfrac{\partial v}{\partial y} + \dfrac{\partial w}{\partial z} = 0 \\ \dfrac{\partial \rho}{\partial t} + u\dfrac{\partial \rho}{\partial x} + v\dfrac{\partial \rho}{\partial y} + w\dfrac{\partial \rho}{\partial z} = \dfrac{\partial}{\partial x}\left(\mathcal{A}\dfrac{\partial \rho}{\partial x}\right) + \dfrac{\partial}{\partial y}\left(\mathcal{A}\dfrac{\partial \rho}{\partial y}\right) + \dfrac{\partial}{\partial z}\left(\mathcal{K}_E\dfrac{\partial v}{\partial z}\right) \end{cases} \tag{2.36}$$

where the reference density ρ_0 and the gravitational acceleration g are constant coefficients, the Coriolis parameter f, and the eddy viscosity and diffusivity coefficients $\mathcal{A}$, ν_E and $\mathcal{K}_E$ may taken as constants or functions of the flow variables and grid parameters. The hydrostatic approximation assumes that the pressure at any point in the

atmosphere is due to the weight of the air above it and is a reasonable approximation when the vertical acceleration is small compared to the gravitational acceleration. The Boussinesq approximation assumes that variations in density are small enough to be neglected except in the buoyancy term.

2.5 The Barotropic Equations on an Equatorial β-plane

The nonlinear equations for the barotropic mode is derived from the full 3d geophysical flow equations in (2.36) by assuming the fluid is homogeneous and inviscid, and the bottom and the surface are flat and horizontal. These assumptions are sufficient to neglect the viscosity, the density and vertical velocity in the primitive equations above (2.36), [5, 14, 36]. We have reduced the primitive equations to the following barotropic equations on a beta-plane:

$$\begin{cases} \dfrac{\partial u}{\partial t} + u\dfrac{\partial u}{\partial x} + v\dfrac{\partial u}{\partial y} - fv = -\dfrac{1}{\rho_0}\dfrac{\partial p}{\partial x} \\ \dfrac{\partial v}{\partial t} + u\dfrac{\partial v}{\partial x} + v\dfrac{\partial v}{\partial y} + fu = -\dfrac{1}{\rho_0}\dfrac{\partial p}{\partial y} \\ \dfrac{\partial u}{\partial x} + \dfrac{\partial v}{\partial y} = 0 \end{cases} \tag{2.37}$$

where the coriolis parameter $f = \beta y$ varies with the northward coordinate y. We now non-dimensionalize this set of equations in (2.37) by means of the following typical scales: For length and velocity, we write

$$\begin{aligned} x &= Lx' \quad & y &= Ly' \\ u &= U_0 u' \quad & v &= U_0 v' \end{aligned}$$

where (x', y') and (u', v') are non-dimensionless variables , L is length scale and U_0 is velocity scale. For time scale T we write

$$t = Tt'$$

with t' non-dimensionless, where

$$T = \frac{L}{U_0}$$

The pressure p is non-dimensionalized by

$$p = U_0^2 \rho_0 p'$$

After substitution in (2.37), we find:

$$\begin{cases} \dfrac{U_0}{T}\dfrac{\partial u}{\partial t'} + \dfrac{U_0^2}{L}\left(u'\dfrac{\partial u'}{\partial x'} + v'\dfrac{\partial u}{\partial y}\right) - U_0 L\beta v' = -\dfrac{U_0^2\rho_0}{\rho_0 L}\dfrac{\partial p'}{\partial x'} \\ \dfrac{U_0}{T}\dfrac{\partial v'}{\partial t'} + \dfrac{U_0^2}{L}\left(u'\dfrac{\partial v'}{\partial x'} + v'\dfrac{\partial v'}{\partial y'}\right) - U_0 L\beta u' = -\dfrac{U_0^2\rho_0}{\rho_0 L}\dfrac{\partial p'}{\partial y'} \\ \dfrac{U_0}{L}\left(\dfrac{\partial u'}{\partial x'} + \dfrac{\partial v'}{\partial y'}\right) = 0 \end{cases}$$

we replace $T = \frac{L}{U_0}$ and divise by $\dfrac{U_0^2}{L}$ in the two first equations above ($\beta = U_0/L^2$), we obtain the following barotropic equations (we drop the primes for the terms in the equations) in the non-dimensional form,

$$\begin{cases} \dfrac{\partial u}{\partial t} + u\dfrac{\partial u}{\partial x} + v\dfrac{\partial u}{\partial y} - yv = -\dfrac{\partial p}{\partial x} \\ \dfrac{\partial v}{\partial t} + u\dfrac{\partial v}{\partial x} + v\dfrac{\partial v}{\partial y} + yu = -\dfrac{\partial p}{\partial y} \\ \dfrac{\partial u}{\partial x} + \dfrac{\partial v}{\partial y} = 0 \end{cases} \tag{2.38}$$

In (2.38), u, v are respectively the zonal (east-west) and meridional (north-south) velocity components. The equations in (2.38) are nondimensionalized by with the characteristic units of equatorial synoptic scale dynamics [14, 36], so that the Coriolis gradient at the equator is normalized to $\beta = 1$, the velocity scale is the gravity wave speed $U_0 = NH_T/\pi \approx 50\ ms^{-1}$ ($N = 10^{-2}s^{-1}$ is the Brunt-Väisälä frequency) and $H_T = 16\ km$ is the tropospheric height. The length scale choice is based on the equatorial Rossby wave deformation radius $L = (U_0/\beta)^{\frac{1}{2}} \approx 1500\ km$ and the time scale is given by $T = L/U_0 = (U_0\beta)^{-\frac{1}{2}} \approx 8.3$ hours.

We can write the system in (2.38) in equivalent vectoriel form

$$\begin{cases} \dfrac{\partial \mathbf{v}}{\partial t} + \mathbf{v}\cdot\nabla\mathbf{v} + y\mathbf{v}^{\perp} + \bigtriangledown p = 0, \\ \operatorname{div}\mathbf{v} = 0. \end{cases} \tag{2.39}$$

where $\mathbf{v} = (u, v)$ with u, v are respectively the zonal (east-west) and meridional (north-south) velocity components. The operator $\nabla = \left(\dfrac{\partial}{\partial x}, \dfrac{\partial}{\partial y}\right)$ is the horizontal gradient vector and $\operatorname{div}\mathbf{v} = \dfrac{\partial u}{\partial x} + \dfrac{\partial v}{\partial y}$ is the horizontal divergence while the term $y\mathbf{v}^{\perp} = y\,(-v, u)$ represents the horizontal components of the Coriolis force due to the vertical component of Earth's rotation (beta effect).

2.6 Barotropic Rossby Waves

Here we consider the linear barotropic equations :

$$\begin{cases} \dfrac{\partial \mathbf{v}}{\partial t} + y\mathbf{v}^{\perp} + \bigtriangledown p = 0, \\ \operatorname{div} \mathbf{v} \ = 0. \end{cases} \tag{2.40}$$

We take the curl of the first equation in (2.40), to get

$$\frac{\partial^2 v}{\partial x \partial t} - \frac{\partial^2 u}{\partial y \partial t} \ + \beta y \left(\frac{\partial u}{\partial y} + \frac{\partial v}{\partial y} \right) - \beta v = 0 \tag{2.41}$$

Introducing the vorticiy ξ defined by

$$\xi \left(x, y, t \right) = \frac{\partial v}{\partial x} - \frac{\partial u}{\partial y} \tag{2.42}$$

and the sream function ψ defined by

$$u = -\frac{\partial \psi}{\partial y}, v = \frac{\partial \psi}{\partial x}. \tag{2.43}$$

and using the incompressible constraint, we obtain

$$\frac{\partial \xi}{\partial t} \ - \beta \frac{\partial \psi}{\partial x} = 0 \tag{2.44}$$

We may actually write this as an equation in the single variable ψ if we note that $\xi = \Delta \psi$ and thus

$$\frac{\partial \Delta \psi}{\partial t} \ - \beta \frac{\partial \psi}{\partial x} = 0 \tag{2.45}$$

Searching for solutions of the form

$$\psi = Re \left\{ e^{i(kx+ly-\omega t)} \right\} \tag{2.46}$$

We obtain

$$\omega \left(k, l \right) = -\frac{\beta k}{k^2 + l^2} \tag{2.47}$$

which is the dispertion relation for the barotropic planetary waves, or Rossby waves, on an equatorial β-plane.

2.7 Barotropic Equations in Vorticity Stream Form

In order to conserve geostrophy (numerically) for the barotropic system in (2.38), we move to the vorticity-stream function formulation [28]. We introduce the potential vorticity

$$\xi = \frac{\partial v}{\partial x} - \frac{\partial u}{\partial y} + y \tag{2.48}$$

and the stream function

$$u = -\frac{\partial \psi}{\partial y},\ v = \frac{\partial \psi}{\partial x} \tag{2.49}$$

The system in (2.38) leads to

$$\begin{cases} \dfrac{\partial \xi}{\partial t} + J(\psi, \xi) = 0, \\ \Delta \psi = \xi - y, \\ u = -\dfrac{\partial \psi}{\partial y}, v = \dfrac{\partial \psi}{\partial x}. \end{cases} \tag{2.50}$$

Here ξ is the potential vorticity, that is the relative vorticity, $\dfrac{\partial v}{\partial x} - \dfrac{\partial u}{\partial y}$, due the flow velocity plus the vertical component of Earth's rotations, βy, and ψ is the stream function. The velocity field is given by $u = -\dfrac{\partial \psi}{\partial y},\ v = \dfrac{\partial \psi}{\partial x}$. The term $J(\psi, \xi)$, the Jacobian determinant $J(\psi, \xi) = \dfrac{\partial \psi}{\partial x}\dfrac{\partial \xi}{\partial y} - \dfrac{\partial \psi}{\partial y}\dfrac{\partial \xi}{\partial x}$, represents the advective non-linearity of potential vorticity ξ by the associated flow. Since the Jacobian determinant of the plane Rossby waves in Equations (2.46) and (2.47) vanishes, the latter are also solutions to the nonlinear system (2.50). These solutions will be used to validate and assess the numerical methods considered in the present work.

2.8 Conservation properties

For our problem, we will restrict the domain to a rectangular strip which is periodic in x. This domain is centred on the equator and represents the tropics, our principal region of interest. The north-south walls are located at a distance $Y = 5000$ km away from the equator and the zonal period is equal to the perimeter of the earth at the equator, i.e., $P = 40000$ km. We assume there is no-flow through the boundaries:

$$v(x, \pm Y, t) = 0, \tag{2.51}$$

then from (2.50) the total enstrophy,

$$\zeta(t) = \frac{1}{2}\int_0^P \int_{-Y}^Y \left(\frac{\partial v(x,y,t)}{\partial x} - \frac{\partial u(x,y,t)}{\partial y}\right)^2 dxdy = \frac{1}{2}\int_0^P \int_{-Y}^Y (\Delta\psi)^2 dxdy \tag{2.52}$$

and kinetic energy

$$E(t) = \frac{1}{2}\int_0^P \int_{-Y}^Y \left(u^2(x,y,t) + v^2(x,y,t)\right) dxdy = \frac{1}{2}\int_{-Y}^Y \int_0^P |\mathbf{v}|^2 dxdy \tag{2.53}$$

are conserved (independent of time t). In fact, the Jacobian determinant in the first equation (2.50) can be written in flux form as

$$J(\psi,\xi) = \frac{\partial}{\partial x}\left(\psi \frac{\partial \xi}{\partial y}\right) - \frac{\partial}{\partial y}\left(\psi \frac{\partial \xi}{\partial x}\right) \tag{2.54}$$

or as

$$J(\psi,\xi) = \frac{\partial}{\partial y}\left(\xi \frac{\partial \psi}{\partial x}\right) - \frac{\partial}{\partial x}\left(\xi \frac{\partial \psi}{\partial y}\right) \tag{2.55}$$

Because of these flux forms, if we denote the domain integral of function p:

$$\langle p \rangle = \int\int p dxdy \tag{2.56}$$

then the domain integral of $J(\psi,\xi)$ vanishes, due to the periodicity of the domain,

$$\langle J(\psi,\xi) \rangle = 0. \tag{2.57}$$

This result implies that

$$\langle \psi J(\psi,\xi) \rangle = \left\langle J\left(\frac{1}{2}\psi^2, \xi\right)\right\rangle = 0. \tag{2.58}$$

$$\langle \xi J(\psi,\xi) \rangle = \left\langle J\left(\psi, \frac{1}{2}\xi^2\right)\right\rangle = 0. \tag{2.59}$$

For simplicity we consider here the relative vorticity $\xi = \dfrac{\partial v}{\partial x} - \dfrac{\partial u}{\partial y}$, noting that $\frac{1}{2}(\xi)^2 = \frac{1}{2}(\Delta\psi)^2$, we may multiply the barotropic vorticity equation (BVE) first equation in (2.50) by $\Delta\psi$ and integrate over the domain to obtain

$$\frac{\partial(\langle \frac{1}{2}(\Delta\psi)^2 \rangle)}{\partial t} + \langle \Delta\psi J(\psi, \Delta\psi) \rangle = 0, \tag{2.60}$$

which implies

$$\frac{\partial(\langle \frac{1}{2}(\Delta\psi)^2 \rangle)}{\partial t} = 0. \tag{2.61}$$

Hence, the domain-integrated enstrophy is conserved. Now consider the kenitic energy, multiplying the BVE by the stream function ψ yields

$$\psi \frac{\partial \xi}{\partial t} = -\psi \operatorname{div}(\mathbf{v}\xi) = -\operatorname{div}(\mathbf{v}\xi\psi) + \xi \mathbf{v} \cdot \nabla\psi, \tag{2.62}$$

where we have made use of the vector identity $\operatorname{div}(\lambda \mathbf{a}) = \nabla\lambda \cdot \mathbf{a} + \lambda \operatorname{div}(\mathbf{a})$. The second term on the right-hand side in the (2.62) vanishes due to the fact that $\mathbf{v}$ is perpendicular to $\nabla\psi$ by definition. With some judicious manipulation, the left-hand side becomes

$$\psi \frac{\partial \xi}{\partial t} = \psi \frac{\partial(\Delta\psi)}{\partial t} = \frac{\partial(\nabla\psi \cdot \nabla\psi)}{\partial t} - \nabla\psi \cdot \frac{\partial \nabla\psi}{\partial t} = \frac{\partial(\mathbf{v} \cdot \mathbf{v})}{\partial t} - \frac{1}{2}\frac{\partial(\mathbf{v} \cdot \mathbf{v})}{\partial t} = \frac{1}{2}\frac{\partial(\mathbf{v} \cdot \mathbf{v})}{\partial t} \tag{2.63}$$

Hence, we have

$$\frac{1}{2}\frac{\partial(\mathbf{v} \cdot \mathbf{v})}{\partial t} = -\operatorname{div}(\mathbf{v}\xi\psi), \tag{2.64}$$

we integrate the last equation over the entire domain, we obtain

$$\frac{\partial(\frac{1}{2}\langle \mathbf{v} \cdot \mathbf{v} \rangle)}{\partial t} = 0. \tag{2.65}$$

Therefore, the domain-integrated kinetic energy is conserved.

Expanding the stream function in a double Fourier series along the x and y:

$$\psi = \sum_k \sum_l a_{k,l} e^{i(kx+ly)} = \sum_{k,l} \psi_{k,l} \tag{2.66}$$

where the $a_{k,l}$ are real coefficients of the Fourier expansion. We define a total wave number $\mathbf{k}$ such that $\mathbf{k}^2 = k^2 + l^2$. Then

$$\langle \mathbf{v} \cdot \mathbf{v} \rangle = \langle \nabla\psi \cdot \nabla\psi \rangle = \langle \operatorname{div}(\psi\nabla\psi) \rangle - \langle \psi\Delta\psi \rangle = \sum_{k,l} \mathbf{k}^2 \langle \psi_{k,l}^2 \rangle \tag{2.67}$$

where we have used the periodicity of the domain and the fact that the Fourier modes are mutually orthogonal. Furthermore,

$$\langle \xi^2 \rangle = \sum_{k,l} \mathbf{k}^4 \langle \psi_{k,l}^2 \rangle . \tag{2.68}$$

Therefore the average wave number $\mathbf{k}_{avg}$, defined by

$$\mathbf{k}_{avg} = \left(\frac{\langle \xi^2 \rangle}{\langle \mathbf{v} \cdot \mathbf{v} \rangle} \right)^{\frac{1}{2}} \tag{2.69}$$

is conserved with time. This shows that no systematic one-way cascade of energy into shorter waves can occur in two-dimensional incompressible flow, ie no net transfer of energy from larger (smaller) scales to smaller (larger) scales; only the following energy exchanges are possible:

$$K_L \longleftarrow K_M \longrightarrow K_S$$

$$K_L \longrightarrow K_M \longleftarrow K_S$$

where K_L, K_M and K_S are the mean kinetic energies of the long waves, medium waves, and short waves, respectively.

Chapter 3

Existence and Uniqueness of solutions of Barotropic Equations

In this chapter we consider the barotropic equations described in the previous chapter of an ideal incompressible fluid in a 2D channel and we prove the existence and uniqueness of classical solutions for all time. The corresponding equations resemble the Euler equations of incompressible flows with a slight difference, the rotative term in the barotropic equations. First, we recall some results of the existence and uniqueness of solutions for the 2D Euler equations in two dimension. All details can be found in [38, 44].

3.1 Review of The Euler Equations

3.1.1 The Euler Equations

Incompressible flows of homogeneous fluids in all of space $\Omega \subseteq \mathbb{R}^2$, are solutions of the system of equations [38, 44]

$$\begin{cases} \frac{D\mathbf{v}}{Dt} = -\nabla p + f \ in \ \Omega \times [0, \ \ +\infty) \\ \operatorname{div} \mathbf{v} = \mathbf{0} \qquad (x,t) \ \in \Omega \times [0, \ \ +\infty) \\ \mathbf{v}\,(x,y,0) = \mathbf{v}_0 \quad (x,y) \ \in \ \Omega \end{cases} \tag{3.1}$$

where Ω is the bounded domain in $\mathbb{R}^2$ with regulary boundary $\partial\Omega$, $\mathbf{v} \equiv (v_1, v_2)$ the fluid velocity, $p\,(x,y,t)$ the pressure, $f\,(x,y,t)$ the forcing term and $\frac{D}{Dt}$ the convective derivative (i.e. the derivative along a particles trajectory)

$$\frac{D}{Dt} = \frac{\partial}{\partial t} + \sum_{j=1}^{2} v^j \frac{\partial}{\partial x_j} \tag{3.2}$$

and div is the divergence of a vector field,

$$\operatorname{div} \mathbf{v} = \sum_{j=1}^{2} \frac{\partial v^j}{\partial x_j} \tag{3.3}$$

The gradient operator ∇ is

$$\nabla = \left(\frac{\partial}{\partial x}, \frac{\partial}{\partial y} \right)^t \tag{3.4}$$

3.1.2 Knowns results

Here we recall some existence and uniqueness results for the solutions of the Euler equations, for all details of existence, uniqueness and the notion of weak solutions and strong solution see the references below. We supplement the system (3.1) with the boundary condition:

$$\mathbf{v} \cdot \mathbf{n} = \mathbf{0} \text{ on } [0, +\infty) \times \partial\Omega \tag{3.5}$$

$$\lim_{|(x,y)| \to \infty} |u| = 0 \text{ for } t \in [0, +\infty) \tag{3.6}$$

The last boundary condition in (3.6) for the case of the unbounded domain. If the initial condition u_0 is smooth then there exists a unique strong solution for all time of the Euler equations (3.1), (3.5) and (3.6) while

- Ω is a bounded smooth domain (Wolibner, 1933),
- $\Omega = \mathbb{R}^2$ (McGrath, 1967),
- Ω is outside smooth domain (Kikuchi, 1983).

The vorticity ω is a very important quantity for the Euler problem

$$\omega = \operatorname{curl} \mathbf{v} = \left(\frac{\partial v_2}{\partial x} - \frac{\partial v_1}{\partial y} \right) \tag{3.7}$$

The vorticity equation is

$$\frac{\partial \omega}{\partial t} + \mathbf{v} \cdot \nabla \omega = \mathbf{0} \tag{3.8}$$

• If $\omega_0 \in L^1\left(\mathbb{R}^2\right) \cap L^\infty\left(\mathbb{R}^2\right)$, then for all time, there exists a unique weak-solution of the $2D$ Euler equations. (A.Majda and A.Bertozzi [38])

• The existence (and the uniqueness) of weak solutions with $\omega_0 \in L^\infty$ in bounded domains was first proved by Yudovich (1963).
• If $\omega_0 \in L^1 \cap L^p(\Omega)$ (with $p > 1$) then there exists a unique weak-solution for all time to the Euler equations while the domain is smooth (Diperna-Majda, 1987).

3.2 Formulation of the Bartropic Equation as an Integrodifferential Equation for the Particle Trajectories

In this section, we show that for sufficiently smooth solutions, the particle-trajectory formulation in (3.24) below is equivalent to the Barotropic equations in (2.39).

3.2.1 Particle Trajectories

The particle-trajectory maping $X(\cdot, t) : \alpha \in \mathbb{R}^2 \longrightarrow X(\alpha, t) \in \mathbb{R}^2$. Given a fluid velocity $\mathbf{v}(z, t)$, $X(\alpha, t) = (X_1, X_2)^t$ is the location of a fluid particle at time t placed at the point $\alpha = (\alpha_1, \alpha_2)$ at time $t = 0$, where $t \in [0, T]$. The following nonlinear ordinary differential equation defines particle-trajectory mapping:

$$\begin{cases} \dfrac{dX}{dt}(\alpha, t) = \mathbf{v}(X(\alpha, t), t) \\ X(0) = \alpha \end{cases} \tag{3.9}$$

The particle-trajectory mapping X has a useful interpretation: An initial domain $\Omega \subseteq \mathbb{R}^2$ in a fluid evolves in time to $X(\Omega, t) = \{X(\alpha, t) : \alpha \in \Omega\}$ with the vector $\mathbf{v}$ tangent to the particle trajectory, (see figure3.1).

3.2.2 The Vorticity-Stream Formulation of the Barotropic Equations

Recall that taking the curl of the Barotropic equations (2.39) leads to the following evolution equation for the potential vorticity :

$$\omega = \operatorname{curl} \mathbf{v} + y \tag{3.10}$$

$$\frac{D\omega}{Dt} = 0 \tag{3.11}$$

For 2D flows the velocity field is $\mathbf{v} = (u, v, 0)^t$, the relative vorticity $\overline{\omega} = (0, 0, \partial_x v - \partial_y u)^t$.

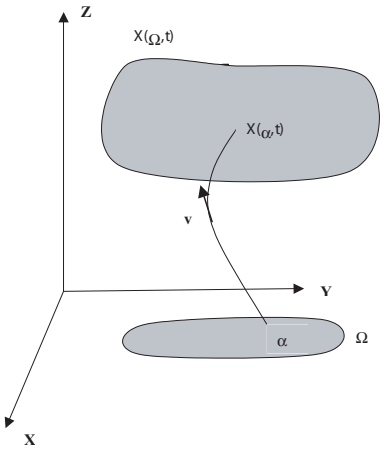

Figure 3.1: The particle-trajectory map.

To simplify the notation we denote the velocity field by $\mathbf{v} = (u, v)^t$ and the scalar relative vorticity by $\overline{\omega} = \partial_x v - \partial_y u$. Thus vorticity equation (3.11) reduces to the scalar vorticity equation

$$\frac{D\omega}{Dt} = 0 \tag{3.12}$$

This equation implies conservation of vorticity along particle trajectories.

$$\omega\left(X\left(\alpha, t\right), t\right) = \omega_0\left(\alpha\right) \tag{3.13}$$

Now we show that for arbitrary 2D flows we can eliminate the velocity from vorticity equation (3.11) to yield a self-contained equation for ω. Because div $\mathbf{v} = 0$, there exists a (unique up to an additive constant) stream function $\psi(x, y, t)$ such that

$$\mathbf{v} = (-\partial_y \psi, \partial_x \psi)^t = \nabla^{\perp} \psi \tag{3.14}$$

Computing the curl of Eq. (3.14) and we use (3.10), we get the Poisson equation for $\psi(x, y, t)$:

$$\Delta \psi = \omega - y. \tag{3.15}$$

Finally the vorticity-stream formulation for $2D$ barotropic equations:

$$\begin{cases} \frac{D\omega}{Dt} = 0 \; in \Omega \times [0, \quad +\infty) \\ \Delta\psi = \omega - y \;\; \in \Omega \times [0, \quad +\infty) \\ \omega\left(x, y, 0\right) = \omega_0 \;\; \in \Omega. \end{cases} \tag{3.16}$$

where $\frac{D}{Dt} = \frac{\partial}{\partial t} + \sum_{j=1}^{2} v^j \frac{\partial}{\partial x_j}$.

For the resolution of the poisson equation in (3.15) and for existence and uniqueness of the solutions of Barotropic equations in 2D channel, we need to give some elementary properties of the Green function for a 2D channel $\Omega = (0,\ L_1) \times (0,\ L_2)$, where L_1 is the period in ox direction. We know that the Green function depends on the form of the domain. In our case, as we will see, the Green function can be written in terms of a series of trigonometric functions in x and y. For details and proofs of these problems we refer to [44].

The Green function for the channel is the solution $G = G(z;p)$ of the following system:

$$\begin{cases} -\Delta G = \delta(z-p) \; in \; \Omega \\ G \text{ periodic in } x \\ G = 0 \text{ at } y = 0 \text{ and } y = L_2 \end{cases} \tag{3.17}$$

where the Laplacian Δ operates in the $z = (x;y)$ variable and $p = (p_1;p_2) \in \Omega$ is fixed, δ is the Dirac function on Ω. We can prove by using the spectral method see [44] that the solution of the problem in (3.17) is

$$G(z,p) = \sum_{m=0}^{\infty}\sum_{n=1}^{\infty} \varepsilon_m \frac{4}{L_1 L_2}\frac{1}{\lambda_{n,m}} \cos\left(\frac{2m\pi}{L_1}(x-p_1)\right) \sin\left(\frac{n\pi y}{L_2}\right) \sin\left(\frac{n\pi p_2}{L_2}\right) \tag{3.18}$$

where we define ε_m as being equal to 1 when $m = 1$ and to $\frac{1}{2}$ when $m = 0$, and $\lambda_{n,m}$ is given by

$$\lambda_{n,m} = \left(\frac{2m\pi}{L_1}\right)^2 + \left(\frac{n\pi}{L_2}\right)^2.$$

The properties of the Green function for a 2D channel, as stated in the following Theorem.

Theorem 3.2.1 *(a) The Green function G for the 2D channel with periodic and homogeneous Dirichlet boundary conditions is continuous on $\overline{\Omega} \times \overline{\Omega}$, excepet at $p = z$.*

(b) G has continuous first -order partial derivatives with respect to p, except at $p = z$, in the neighborhood of which the following estimate holds:

$$|D_p G(p,z)| \leq K |p-z|^{-1} \tag{3.19}$$

(c) G is symmetrical in z and p.

3. EXISTENCE AND UNIQUENESS OF SOLUTIONS OF BAROTROPIC EQUATIONS

By the above results the solution of equation (3.15) in a 2D channel with periodic and homogeneous Dirichlet boundary conditions is given by

$$\psi(x,y,t) = \int_{\Omega} G(x,y;p)\,(\omega(p,t) - p_2)\,dp. \tag{3.20}$$

and

$$\mathbf{v}(x,y,t) = \operatorname{curl} \int_{\Omega} G(x,y;p)\,(\omega(p,t) - p_2)\,dp \tag{3.21}$$

In our case the 2D flows is inviscid , the vorticity cannot amplify because it is conserved on particle trajectories. We have according to (3.13)

$$\omega(X(\alpha,t),t) = \omega_0(\alpha)$$

and hence the velocity in (3.21) is:

$$\mathbf{v}(x,y,t) = \int_{\Omega} \operatorname{curl} G\left((x,y);X\left(\alpha',t\right)\right)\left(\omega_0\left(\alpha'\right) - X_2\left(\alpha',t\right)\right)d\alpha' \tag{3.22}$$

The 2D integrodifferential equation for the particle trajectories $X(\alpha,t)$ is

$$\begin{cases} \dfrac{dX}{dt}(\alpha,t) = \displaystyle\int_{\Omega} \operatorname{curl} G\left(X(\alpha,t);X\left(\alpha',t\right)\right)\left(\omega_0\left(\alpha'\right) - X_2\left(\alpha',t\right)\right)d\alpha' \\ X(0) = \alpha \end{cases} \tag{3.23}$$

A solution $X(\alpha,t)$ to equation (3.23) defines a velocity $\mathbf{v}$ either from equation (3.22) and a vorticity from (3.13). To complete this section, we give a result that for smooth solutions, the particule trajectory formulation is equivalent to the barotropic equation.

Proposition 3.2.2 *Let* $\mathbf{v}_0(x,y)$ *be a smooth velocity field satisfying* $\operatorname{div}\mathbf{v}_0 = 0$,*and* $\omega_0 = \operatorname{curl}\mathbf{v}_0 + y$. *Let* $X(\alpha,t)$ *solve*

$$\begin{cases} \dfrac{dX}{dt}(\alpha,t) = \displaystyle\int_{\Omega} \operatorname{curl} G\left(X(\alpha,t);X\left(\alpha',t\right)\right)\left(\omega_0\left(\alpha'\right) - X_2\left(\alpha',t\right)\right)d\alpha' \\ X(0) = \alpha. \end{cases} \tag{3.24}$$

Define the velocity $\mathbf{v}$ *by*

$$\mathbf{v}(x,y,t) = \int_{\Omega} \operatorname{curl} G\left((x,y);X\left(\alpha',t\right)\right)\left(\omega_0\left(\alpha'\right) - X_2\left(\alpha',t\right)\right)d\alpha' \tag{3.25}$$

Then integrodifferential equation (3.24) *for the particle trajectories is equivalent to the barotropic equation in* (2.39) *for sufficiently smooth solutions.*

Proof The derivation of particle-trajectory equation (3.24) shows that if a smooth velocity $\mathbf{v}$ solves the Barotropic equations in (2.39), then the particle trajectories X defined by (3.9), solve integrodifferential equation (3.24). For prove the converse, we have showed above the Barotropic equations is equivalent to the vorticity-stream formulation; hence it suffices to show that the solution to equation (3.24) yields a $\mathbf{v}(x, y, t)$ and an $\omega(x, y, t)$ such that

$$\begin{array}{ll} \operatorname{curl} \mathbf{v} = \omega - y & \operatorname{div} \mathbf{v} = 0 \\ \frac{D\omega}{Dt} = 0 & \omega(x, y, 0) = \omega_0 \end{array}$$

The remain of the proof of the converse, follows the same steps as in the case of 2D Euler equation in the book of A.Majda and A.Bertozzi [38].

□

3.3 Barotropic Equations in a 2D channel

In this section we consider the Barotropic equations in (2.39) in a 2D channel with the non-penetration boundary condition and we give a result of the existence and uniqueness of classical solution for all time. The main steps to prove the existence and uniqueness are based on the reference [44].

3.3.1 Barotropic problem

The barotropic equations in a 2D channel $\Omega_\infty = \mathbb{R} \times (0,\ L_2)$ considered here:

$$\begin{cases} \dfrac{\partial \mathbf{v}}{\partial t} + \mathbf{v} \cdot \nabla \mathbf{v} + y\mathbf{v}^\perp + \bigtriangledown p = 0, \\ \operatorname{div} \mathbf{v} = 0 \end{cases} \tag{3.26}$$

where $\mathbf{v} \equiv (u, v)$ is the two dimensional velocity of the fluid, p is the scalar pressure, while the term $y\mathbf{v}^\perp = y(-v, u)$ represents the horizontal components of the Coriolis force due to the vertical component of Earth's rotation (beta effect).
We also consider $\Omega = (0, X) \times (0, Y)$, where X is periode in the Ox direction and $Y > 0$. For a function $\mathbf{v}$ given in Ω, we denote by $\widetilde{\mathbf{v}}$ its periodic extension to Ω_∞. We supplement the system (3.26) with the initial condition:

$$\mathbf{v}(x, y, 0) = \mathbf{v}_0 \quad (x, y) \in \Omega \tag{3.27}$$

The boundary conditions for this system are:

$$\begin{array}{l} \mathbf{v}\cdot n=0 \text{ sur } \Gamma_2=\{y=0\ ,\ y=Y\} \\ \mathbf{v} \text{ periodic en } x \end{array} \tag{3.28}$$

Remark 3.3.1 *Because of the periodicity in the x direction, it is convenient to introduce the average of u over Ω,*

$$m_u=\frac{1}{XY}\int_\Omega u\left(x,y,t\right)dx.$$

We can suppose from the beginning that we work with flows having $m_u=0$.

For a function given in Ω, we denote by $\widetilde{\mathbf{v}}$ its periodic extension to Ω_∞. The main result of this section is the following:

Theorem 3.3.2 *Let X,Y,T be given positive and arbitrary, and let $\Omega=(0,X)\times(0,Y)$. Let $\mathbf{v}_0$ be given such that its periodic extension $\widetilde{\mathbf{v}}_0$ belongs to $C^{1+\alpha,0}\left(\Omega_\infty\right)$ and satisfies $\operatorname{div}\widetilde{\mathbf{v}}_0=0$ and $\widetilde{\mathbf{v}}_0\cdot n=0$ at $y=0$ and $y=L_2$, with $0<\alpha<1$. Then there exists a unique solution $\mathbf{v}$ periodic and a unique solution up to a function in time p of problem (3.26) such that:*

$$\mathbf{v}\in\mathbf{C}^1\left(Q_T\right),\quad \nabla p\in C\left(Q_T\right).$$

where $Q_T=\overline{\Omega}\times[0,T]$.

We recall here the definition of the Hölder spaces and of their norms.

Définition 3.3.3 *Let $Q_T=\overline{\Omega}\times[0,T]$ and $\alpha\in\left]0,1\right]$. For all $f\in C^0\left(Q_T\right)$, we put*

$$H_z^\alpha\left(f\right)=\sup\left\{\frac{\left|f\left(z_1,t\right)-f\left(z_2,t\right)\right|}{\left\|z_1-z_2\right\|^\alpha},z_1,z_2\in\overline{\Omega}\ ,z_1\neq z_2,t\in[0,T]\right\}$$

$$H_t^\alpha\left(f\right)=\sup\left\{\frac{\left|f\left(z,t_1\right)-f\left(z,t_2\right)\right|}{\left\|t_1-t_2\right\|^\alpha},t_1,t_2\in[0,T]\ \ ,t_1\neq t_2,z\in\overline{\Omega}\right\}$$

Then we define

$$C^{\alpha,\alpha}\left(Q_T\right)=\left\{\ f\in C^0\left(Q_T\right)/\ H_z^\alpha\left(f\right)\ \text{ and } H_t^\alpha\left(f\right)\ \text{ are finite.}\ \right\}$$

Remark 3.3.4 *Then $\forall f\in C^{\alpha,\alpha}\left(Q_T\right)$, $\exists C>0$ such that ,*

$$\left|f\left(z_1,t\right)-f\left(z_2,t\right)\right|\leq C\left(\left\|z_1-z_2\right\|^\alpha+\left|t_1-t_2\right|^\alpha\right),\forall\ z_1,z_2\in\Omega,\ \forall t_1,t_2\in[0,T]$$

The norms is defined as:

$$|f|_{\alpha,Q_T} = |f|_{0,Q_T} + H_z^{\alpha}(f) + H_t^{\alpha}(f),$$

where $|\cdot|_{0,Q_T}$ is the norm of $C(Q_T)$.

Définition 3.3.5 *(**Hölder spaces** $C^{k+\alpha}(\overline{\Omega})$)*

Let $\alpha \in]0,1]$, and $k \in \mathbb{N}$. Then we define

$$C^{k+\alpha}(\overline{\Omega}) = \left\{ f \in C^k(\overline{\Omega}) \,/\, ;\ f \text{ bounded and } \forall \nu \ \ |\nu| \leq k \ \Rightarrow D^{\nu} f \ \in C^{\alpha,0}(\overline{\Omega}). \right\}$$

The norme of $C^{k+\alpha}(\overline{\Omega})$ is defined as

$$\|f\|_{\alpha,k} = \sum_{|\nu| \leq k} \left(\|D^{\nu} f\|_{\infty} + \sup_{z \neq p} \frac{|f^{\nu}(z) - f^{\nu}(p)|}{\|z-p\|^{\alpha}} \right)$$

3.3.2 Existence and uniqueness of the solution for all time

In this section we prove Theorem 3.3.1. The proof of existence of solutions is based on Schauder's fixed point theorem.
We introduce the potential vorticity

$$\omega = \frac{\partial v}{\partial x} - \frac{\partial u}{\partial y} + y$$

and we take the rotationnel in the first equation in (3.26), we obtain the two following problems

$$\begin{cases} \frac{\partial \omega}{\partial t} + \mathbf{v} \cdot \nabla \omega = 0 \\ \omega \text{ is periodic in } x \\ \omega(x,y,0) = \omega_0(x,y) = \operatorname{curl} \mathbf{v}_0 + y \end{cases} \tag{3.29}$$

$$\begin{cases} \operatorname{curl} \mathbf{v} = \omega - y \\ \operatorname{div} \mathbf{v} = 0 \\ \mathbf{v} \text{ is periodic in } x; \mathbf{v} \cdot n = \mathbf{0} \text{ at } y = 0 \text{ and } y = Y \\ m_u = 0 \end{cases} \tag{3.30}$$

Note here that without the condition $m_u = 0$, the flow $\mathbf{v}$ would be determined up to a constant.

3.3.2.1 Preliminary results

We have showed above that the problems (3.29) and (3.30) is equivalent to (3.26) and we will find the solution $\mathbf{v}$ of problems (3.29) and (3.30) as the fixed point of the mapping $\wedge$ defined below. In order to define the mapping $\wedge$, we start with a given function ω^0 and determine a function $\mathbf{v}^1$ from (3.30); then setting $\mathbf{v} = \mathbf{v}^1$ in(3.29), we find the vorticity ω^1 from (3.29). We thus define the function $\wedge$ by

$$\wedge : \bigcup_{0<\varepsilon<1} C^{\varepsilon,0}(Q_T) \longrightarrow C(Q_T), \wedge\left(\omega^0\right) = \omega^1 \tag{3.31}$$

and, as mentioned before, we show that $\wedge$ has a fixed point ω which is the solution of our problem (3.26).

For problem(3.30), we have $\operatorname{div}\mathbf{v} = 0$, there exists a stream function ψ such that $\mathbf{v} = \operatorname{curl}\psi$. We thus need to determine ψ as the solution of the poisson equation

$$\begin{cases} -\Delta\psi = \omega - y = \varpi \\ \psi \text{ periodic in } x \\ \psi = 0 \text{ at } y = 0 \text{ and } y = L_2 \end{cases} \tag{3.32}$$

We find

$$\mathbf{v}(x,y,t) = \operatorname{curl}\int_{\Omega} G(x,y;p)\,\varpi(p,t)\,dp \tag{3.33}$$

where G is the Green function for the Dirichlet problem for the channel given in (3.18). Now we show the quasi-Lipschitz condition is satisfed by the velocity given in (3.33).

Lemma 3.3.6 *If $\overline{\omega} \in L^{\infty}(\Omega)$, then the two following inequalities hold for every p, p' in Ω :*

$$|\mathbf{v}(p)| \leq K\|\overline{\omega}\|_{\infty} \tag{3.34}$$

$$\left|\mathbf{v}(p) - \mathbf{v}\left(p'\right)\right| \leq K\|\overline{\omega}\|_{\infty}\Phi\left(\left|p - p'\right|\right) \tag{3.35}$$

where $\|.\|_{\infty}$ is the $L^{\infty}(\Omega)$-norm, K is a constant depending only on Ω and the function Φ is:

$$\Phi(r) = \begin{cases} r(1 - \ln r), & \text{if } r < 1, \\ 1\ , & \text{if } r \geq 1. \end{cases}$$

Proof For the inequality (3.34), we use the property (3.19) of the Green function G:

$$|\mathbf{v}(p)| = \left| \int_\Omega \operatorname{curl}_p G(p;z)\,\overline{\omega}(z,t)\,dz \right| \leq \|\overline{\omega}\|_\infty \int_\Omega |\operatorname{curl}_p G(p;z)\,\overline{\omega}(z,t)|\,dz \tag{3.36}$$
$$\leq \|\overline{\omega}\|_\infty \int_\Omega \frac{K}{|p-z|}dz < \infty.$$

In order to prove (3.35) , we set $r = |p-p'|$. If $r \geq 1$ then

$$\left|\mathbf{v}(p) - \mathbf{v}(p')\right| \leq \|\overline{\omega}\|_\infty \int_\Omega \left|\operatorname{curl}_p G(p;z)\,\overline{\omega}(z,t) - \operatorname{curl}_{p'} G(p';z)\,\overline{\omega}(z,t)\right| dz \tag{3.37}$$
$$\leq K\|\overline{\omega}\|_\infty \left(\int_\Omega \frac{1}{|p-z|}dz + \int_\Omega \frac{1}{|p'-z|}dz \right) \leq K\|\overline{\omega}\|_\infty$$

If $r < 1$, we consider $B = B(x, 2r)$ the ball centred at x of radius $2r$ and write:

$$\begin{aligned} &\int_\Omega \left|\operatorname{curl}_p G(p;z)\,\overline{\omega}(z,t) - \operatorname{curl}_{p'} G(p';z)\,\overline{\omega}(z,t)\right| dz = \\ &\int_{\Omega\cap B} \left|\operatorname{curl}_p G(p;z)\,\overline{\omega}(z,t) - \operatorname{curl}_{p'} G(p';z)\,\overline{\omega}(z,t)\right| dz + \\ &\int_{\Omega - B} \left|\operatorname{curl}_p G(p;z)\,\overline{\omega}(z,t) - \operatorname{curl}_{p'} G(p';z)\,\overline{\omega}(z,t)\right| dz \end{aligned} \tag{3.38}$$

For the first integral from (3.38), we use (3.19):

$$\begin{aligned} \int_{\Omega\cap B} \left|\operatorname{curl}_p G(p;z)\,\overline{\omega}(z,t) - \operatorname{curl}_{p'} G(p';z)\,\overline{\omega}(z,t)\right| dz &\leq K\left(\int_{\Omega\cap B} \frac{1}{|p-z|}dz + \int_{\Omega\cap B} \frac{1}{|p'-z|}dz \right) \\ &\leq K \int_{|p-z|\leq 2r} \frac{1}{|p-z|}dz + K \int_{|p'-z|\leq 3r} \frac{1}{|p'-z|}dz \\ &\leq 2Kr. \end{aligned}$$

In order to estimate the second integral from (3.38), we choose a particular point $\overline{p}$ on

the segment pp', such that:

$$\begin{aligned}
&\int_{\Omega-B} \left|\operatorname{curl}_p G(p;z)\,\overline{\omega}(z,t) - \operatorname{curl}_{p'} G(p';z)\,\overline{\omega}(z,t)\right| dz \\
&= \int_{\Omega-B} \left|p-p'\right| \left|\nabla_{(pp')} \operatorname{curl}_p G(\overline{p};z)\,\overline{\omega}(z,t)\right| dz \\
&\leq rK \int_{\Omega-B} \frac{1}{|\overline{p}-z|^2} dz
\end{aligned}$$

where $\nabla_{(pp')}$ is the derivative in the direction (pp'). We see for z outside the ball $B, |\overline{p}-z| > |p-z|/2$ so the integral is bounded by

$$\begin{aligned}
4rK \int_{\Omega-B} \frac{1}{|p-z|^2} dz &\leq rK \int_{2r\leq|p-z|\leq R} \frac{1}{|p-z|^2} dz \\
&\leq 8\pi rK \ln(R/2r)
\end{aligned}$$

where R is the diameter of the domain Ω. Gathering the above relations we find (3.35). □

Now we give some regularity results for the function $\mathbf{v}$ given by (3.33). For the proof and details, we refer the interested reader to [44]. We have:

Lemma 3.3.7 *Let $0<\beta<1$. If $\omega \in C^{\beta,0}(Q_T)$, then $\mathbf{v} \in C^{1+\beta',0}(Q_T)$ for an $\beta'<\beta$. If $\omega \in C^{\beta,\varepsilon}(Q_T)$, then $\mathbf{v} \in C^{1+\beta',\varepsilon'}(Q_T)$ for an $\beta'<\beta$, $\varepsilon'<\varepsilon<1$.*

The equation in (3.29) is a first-order partial differential equation for ω, which equivalent to solving the ordinary differential equation (see the previous section)

$$\begin{cases} \dfrac{dX}{dt} = \mathbf{v}(X,t) \\ X(s) = z \end{cases} \tag{3.39}$$

where $0 \leq s \leq t$, $X = X(t,z,s)$. The solutions of (3.39) are the trajectoires of the flow $\mathbf{v}$. Then the solution of (3.29) is determined from the formula:

$$\omega(X(t,z,s),t) = \omega_0(X(0,z,s)) \tag{3.40}$$

We now need to study the existence of the fluid trajectories and their properties.

Lemma 3.3.8 *Let us consider the Cauchy problem in* $\mathbb{R}^n$

$$\begin{cases} \dfrac{dX}{dt} = \mathbf{b}(X,t) \\ X(0) = X_0 \end{cases} \tag{3.41}$$

with $\mathbf{b} \in C(\mathbb{R}^n \times [0,T])$*, uniformly bounded and satisfying the condition*

$$|\mathbf{b}(X,t) - \mathbf{b}(Y,t)| \leq K_0 \Phi(|X-Y|), \tag{3.42}$$

where K_0 *is a positive constant independent of* t *and* Φ *is the function defined above. Then problem* (3.41) *has a unique solution* $X = X(t)$*.*

Proof see [44] □

Lemma 3.3.9 *The differential equation* (3.39) *has a unique global solution* $X(t,z,s)$ *existing for* $0 \leq t \leq T$*,for any initial condition* $X(s) = z$ *where* $0 \leq s \leq T$ *and* $z \in \Omega$*.*

Proof The proof of this result is based on the previous lemma 3.3.7. Because of (3.34) and (3.35) the property (3.42) is satisfied. The velocity $\mathbf{v}$ given by (3.33), is a continuous function in (x,y) and in t by lemma 3.3.6. □

Lemma 3.3.10 *Let* $X = X(t,z,s)$ *be the solution of* (3.39)*. Then* X *is continuously differentiable as a function of the three variables. For* s *and* t *fixed, the function* X *is a one-to-one, measure preserving map of the domain into itself, with:*

$$\begin{aligned} X(t, X(s,z,t), s) &= X(t,z,t) = z, \\ X(s, X(t,z,r), t) &= X(s,z,r). \end{aligned} \tag{3.43}$$

Proof The properties follows from the theory of ordinary differential equations and from the fact that $\operatorname{div} \mathbf{v} = 0$. The result is known as the Liouville theorem. □

We now need to see in what sense the vorticity given by formula (3.40) is a solution of equation (3.29).

Définition 3.3.11 *We say that* ω *is a weak solution of equation* (3.29) *if for all* $\psi \in C^1(\overline{\Omega})$ *we have*

$$\frac{d}{dt}(\omega, \psi) = (\omega, \mathbf{v} \cdot \nabla \psi)$$

where $(.,.)$ *is the inner product in* $L^2(\Omega)$*.*

We have the following result:

Lemma 3.3.12 *If $\omega_0 \in C\left(\overline{\Omega}\right)$, then ω is a weak solution of equation (3.29), meaning that for every $\psi \in C^1\left(\overline{\Omega}\right)$ we have*

$$\frac{d}{dt}(\omega, \psi) = (\omega, \mathbf{v} \cdot \nabla\psi) \tag{3.44}$$

Proof From formula (3.40) and by lemma 3.3.9 ,we can written ω as

$$\omega(z,t) = \omega_0(X(0,z,t)) \tag{3.45}$$

$$(\omega, \psi) = \int_\Omega \omega_0\left(X\left(0,z',t\right)\right)\psi\left(z'\right)dz', \tag{3.46}$$

we make the change of variable $z' = X(t,z,0)$ in (3.46) and we use the lemma 3.3.9, we obtain:

$$(\omega, \psi) = \int_\Omega \omega_0\left(X\left(0,z',t\right)\right)\psi\left(z'\right)dz' = \int_\Omega \omega_0(z)\,\psi(X(t,z,0))\,dz, \tag{3.47}$$

Taking the derivative in time of (3.47), we find

$$\begin{aligned}\frac{d}{dt}(\omega,\psi) &= \int_\Omega \omega_0(z)\,\frac{d}{dt}\psi(X(t,z,0))\,dz \\ &= \int_\Omega \omega_0(z)\,\nabla\psi(X(t,z,0))\cdot\mathbf{v}(X(t,z,0),t)\,dz\end{aligned} \tag{3.48}$$

we make the change of variable $z = X(0,z',t)$ in (3.48) and we use the lemma 3.3.9, we obtain:

$$\begin{aligned}\frac{d}{dt}(\omega,\psi) &= \int_\Omega \omega_0\left(X\left(0,z',t\right)\right)\nabla\psi\left(z'\right)\cdot\mathbf{v}\left(z',t\right)dz' \\ &= (\omega, \mathbf{v}\cdot\nabla\psi)\end{aligned}$$

□

3.3.2.2 A priori estimates and regularity

Here we are interested to schow some in priori estimates for the velocity , the trajectoires and the vorticity, in order to prove that we can apply the Schauders fixed point theorem to the function $\wedge$ defined by (3.31). For the velocity were already given in (3.34). For the trajectoires we have the following estimates:

Lemma 3.3.13 *Let $X(t,z,s)$ be the solution of equation (3.39). Then the following estimate holds for $|z_1 - z_2| \leq 1$, $|t_1 - t_2| \leq 1$, $|s_1 - s_2| \leq 1$*

$$|X(t_1,z_1,s_1) - X(t_2,z_2,s_2)| \leq C\left(\left\|\omega^0 - y\right\|_\infty\right)\left(|z_1 - z_2|^\delta + |t_1 - t_2|^\delta + |s_1 - s_2|^\delta\right) \tag{3.49}$$

where $\delta << 1$, which depends on the $L^\infty(Q_T)$ norm of ω^0.

Proof (i) Let us consider two arbitrary points p_1,p_2 and the corresponding trajectories $X(t,p_1,s)$ and $X(t,p_2,s)$. Setting $z(t) = X(t,p_1,s) - X(t,p_2,s)$, z satisfies the equation

$$\begin{cases} \dfrac{dz}{dt} = & \mathbf{v}(X(t,p_1,s),t) - \mathbf{v}(X(t,p_2,s),t) \\ z(s) = & p_1 - p_2 \end{cases} \tag{3.50}$$

We assume that $|p_1 - p_2| < 1$, which mean $|z(s)| < 1$. Then, there existe a maximal subinterval I in $[0,T]$ containing s such that $|z(t)| < 1$ for all $t \in I$. Since z is a continuous function, the interval I is open. From (3.50) and using lemma 3.3.5, we have

$$\begin{aligned} \left|\frac{dz}{dt}\right| &= |\mathbf{v}(X(t,p_1,s),t) - \mathbf{v}(X(t,p_2,s),t)| \\ &\leq K\left\|\omega^0 - y\right\|_\infty \chi(|X(t,p_1,s) - X(t,p_2,s)|) \\ &= C_1\chi(|z(t)|) \end{aligned} \tag{3.51}$$

where $C_1 = K\left\|\omega^0 - y\right\|_\infty$. We also have

$$\frac{d}{dt}|z(t)| \leq C_1\chi(|z(t)|) \tag{3.52}$$

since by Stampacchia's Theorem we know that:

$$\left|\frac{d}{dt}|z(t)|\right| = \left|\frac{dz(t)}{dt}\right| \tag{3.53}$$

In view of lemma 3.3.13 below, we need the solution of the following ordinary differential equation:

$$\begin{aligned} \frac{dm}{dt} &= C_1 m\left(1 - m\ln m\right) \\ m\left(s\right) &= \left|p_1 - p_2\right| \end{aligned} \tag{3.54}$$

which is found to be $m\left(t\right) = e^{1-e^{C_1(s-t)}}\left|p_1 - p_2\right|^{e^{C_1(s-t)}}$.

We can apply Lemma 3.3.13 below as long as $m\left(t\right) < 1$ and we obtain:

$$\begin{aligned} \left|z\left(t\right)\right| &\leq e^{1-e^{C_1(s-t)}}\left|p_1 - p_2\right|^{e^{C_1(s-t)}} \\ &\leq e\left|p_1 - p_2\right|^{e^{C_1(s-t)}} < 1 \end{aligned} \tag{3.55}$$

for $0 < s, t < T$, if $\left|p_1 - p_2\right| < e^{-e^{C_1 T}} < 1$.

The interval I coincides with $\left[0, T\right]$. Indeed, if $I = (t_0, t_1)$, with $0 \leq t_0 \leq t_1 < T$ is the maximal interval containing s on which $\left|z\left(t\right)\right| < 1$,then by continuity of the solution, we have:

$$\left|z\left(t_1\right)\right| \leq e^{1-e^{C_1 T}}\left|p_1 - p_2\right|^{e^{C_1|s-t_1|}} < 1 \tag{3.56}$$

This contradicts the maximality of the interval I.

Finally the restriction $\left|p_1 - p_2\right| < e^{-e^{C_1 T}} < 1$ can be removed by increasing the constant in (3.49) and thus the estimation (3.49) is valid for $t_1 = t_2$, $s_1 = s_2$, $\left|p_1 - p_2\right| \leq 1$, and $\delta = e^{-C_1 T}$.

(ii) Let us consider two arbitrary points t_1,t_2 and the corresponding trajectories $X\left(t_1, p, s\right)$ and $X\left(t_2, p, s\right)$.Taking the difference between these function, we find:

$$\begin{aligned} \left|X\left(t_1, p, s\right) - X\left(t_2, p, s\right)\right| &= \left|\int_s^{t_1} \mathbf{v}\left(X\left(r, p, s\right), r\right) dr - \int_s^{t_2} \mathbf{v}\left(X\left(r, p, s\right), r\right) dr\right| \\ &= \left|\int_{t_1}^{t_2} \mathbf{v}\left(X\left(r, p, s\right), r\right) dr\right| \leq \left\|\mathbf{v}\right\|_\infty \left|t_1 - t_2\right| \\ &\leq K\left\|\omega^0 - y\right\|_\infty \left|t_1 - t_2\right| \end{aligned} \tag{3.57}$$

where we used (3.33) for the last inequality.

(*iii*) It now remains to estimate the trajectoiries in s. As before, Let us consider two arbitrary points s_1,s_2 and the corresponding trajectories $X\left(t, p, s_1\right)$ and $X\left(t, p, s_2\right)$.

We set $a = X(t,p,s_1), b = X(t,p,s_2)$ and $c = X(s_1,p,s_2)$. Then, by Lemma 3.3.9, we also known that $b = X(t,c,s_1)$, and we find:

$$\begin{aligned} |a-b| &= |X(t,p,s_1) - X(t,p,s_2)| \\ &= |X(t,p,s_1) - X(t,c,s_1)| \\ &\leq C'\left(\left\|\omega^0 - y\right\|_\infty\right)|p-c|^\delta \end{aligned} \tag{3.58}$$

where $\delta = e^{-C_1 T}$. Using now (3.57) from point (ii), we compute:

$$\begin{aligned} |p-c| &= |X(s_2,p,s_2) - X(s_1,p,s_2)| \\ &\leq C''(\left\|\omega^0 - y\right\|_\infty)|s_2 - s_1| \end{aligned} \tag{3.59}$$

Equations (3.57) and (3.58) lead to:

$$|X(t,p,s_1) - X(t,p,s_2)| \leq C'''\left(\left\|\omega^0 - y\right\|_\infty\right)|s_2 - s_1|^\delta \tag{3.60}$$

Taking into account (i), (ii) and (iii), we obtain:

$$|X(t_1,p_1,s_1) - X(t_2,p_2,s_2)| \leq C''''\left(\left\|\omega^0 - y\right\|_\infty\right)\left(|t_1 - t_2|^\delta + |p_1 - p_2| + |s_2 - s_1|^\delta\right) \tag{3.61}$$

which proves lemma. □

Lemma 3.3.14 *Let $u \in C([0,T];\mathbb{R}_+)$ and let $\varphi \in C(\mathbb{R}_+,\mathbb{R}_+)$ be a nondecreasing function, such that:*

$$u(t) \leq u(0) + \int_0^t \varphi(u(s))\,ds, \quad t \leq T, \tag{3.62}$$

and let $v = v(t)$ be the solution of the initial value problem:

$$\begin{aligned} \frac{dv}{dt} &= \varphi(v) \\ v(0) &= u(0). \end{aligned} \tag{3.63}$$

Then

$$u(t) \leq v(t) \quad \text{for any } t \in [0,T]. \tag{3.64}$$

Proof [44]. □

It remains to estimate the vorticity. We have the following result

Lemma 3.3.15 *If* $\omega^1 = \Lambda\left(\omega^0\right)$, $\omega_0 \in C^\alpha\left(\overline{\Omega}\right)$, *then the following inequalities hold:*

$$\left|\omega^1(x,y,t)\right| \leq \|\omega_0\|_\infty \tag{3.65}$$

$$\left|\omega^1(z_1,t_1) - \omega^1(z_2,t_2)\right| \leq C'\left(\left\|\omega^0 - y\right\|_\infty, |\omega_0|_\alpha\right)\left(|z_1 - z_2|^{\delta'} + |t_1 - t_2|^{\delta'}\right) \tag{3.66}$$

for $|z_1 - z_2| \leq 1$, $|t_1 - t_2| \leq 1$, *where* $\delta' = \alpha\delta$ *and* δ *is the same as in lemma 3.3.13.*

Proof Let use consider two points z_1, z_2 and the corresponding trajectories $X(t, z_1, s), X(t, z_2, s)$. We find:

$$\left|\omega^1(z_1,t) - \omega^1(z_2,t)\right| \leq \left|\omega_0(X(0,z_1,t)) - \omega_0(X(0,z_2,t))\right| \tag{3.67}$$

Since $\omega_0 \in C^\alpha\left(\overline{\Omega}\right)$, then

$$\begin{aligned}\left|\omega_0(X(0,z_1,t)) - \omega_0(X(0,z_2,t))\right| &\leq H_z^\alpha(\omega_0)\left|X(0,z_1,t) - X(0,z_2,t)\right|^\alpha \\ &\leq H_z^\alpha(\omega_0)\, C\left(\left\|\omega^0 - y\right\|_\infty\right)|z_1 - z_2|^{\delta\alpha}\end{aligned} \tag{3.68}$$

where in the last inequality we made use of lemma 3.3.13. Let use consider two arbitrary instants of time t_1 and t_2. We write:

$$\left|\omega^1(z,t_1) - \omega^1(z,t_2)\right| \leq \left|\omega_0(X(0,z,t_1)) - \omega_0(X(0,z,t_2))\right| \tag{3.69}$$

Using lemma 3.3.13. and $\omega_0 \in C^\alpha\left(\overline{\Omega}\right)$ in (3.69), we have

$$\left|\omega_0(X(0,z,t_1)) - \omega_0(X(0,z,t_2))\right| \leq H_z^\alpha(\omega_0)\, C\left(\left\|\omega^0 - y\right\|_\infty\right)|t_1 - t_2|^{\delta\alpha} \tag{3.70}$$

Gathering the above relations (3.68) and (3.70), we find (3.66). □

3.3.3 Application of the Schauder fixed point theorem

From (3.65), we have:

$$\left\|\omega^1\right\|_\infty \leq \|\omega_0\|_\infty \leq M \tag{3.71}$$

We definie S as the subset of $C(Q_T)$ consisting of the functions ω satisfying $\|\omega\|_\infty \leq M$ and

$$\left|\omega(z_1,t_1) - \omega(z_2,t_2)\right| \leq C''(M)\left(|z_1 - z_2|^{\delta''} + |t_1 - t_2|^{\delta''}\right) \tag{3.72}$$

when $|z_1 - z_2| \leq 1$, $|t_1 - t_2| \leq 1$; δ" was obtained by replacing $\left\|\omega^0 - y\right\|_\infty$ by M in the definition of δ' and $C''(M)$ was obtained by the same manner from (3.66). The set S is a convex compact subset of $C(Q_T)$,(S compact because it is closed, bounded and equicontinuous in $C(Q_T)$ and using the Arze-Ascoli Theorem we have S compact). The function Λ defined by (3.31) maps the set S into itself. In order to apply the Schauder fixed point theorem, we have the following result :

Lemma 3.3.16 *The function Λ is continuous on S for the topology of $C(Q_T)$.*

Proof Consider a sequence ω_n^0, $n \in \mathbb{N}$ and ω^0 all $\in S$ and assume that ω_n^0 converges to ω^0 in the topology of $C(Q_T)$. Then $\overline{\omega_n^0} = \omega_n^0 - y$ converges to $\overline{\omega^0} = \omega^0 - y$ and by lemma 3.3.5 $\mathbf{v}_n$ converge to $\mathbf{v}$ in the topology of $C(Q_T)$.

Now we need to study the behavior of the trajectories corresponding respectively to $\mathbf{v}_n$ and $\mathbf{v}$.we have

$$\begin{aligned} |X_n(t,z,s) - X(t,z,s)| &\leq \int_s^t \left|\mathbf{v}_n\left(X_n\left(t',z,s\right),t'\right) - \mathbf{v}\left(X\left(t',z,s\right),t'\right)\right| dt' \qquad (3.73)\\ &\leq \int_s^t \left|\mathbf{v}_n\left(X_n\left(t',z,s\right),t'\right) - \mathbf{v}_n\left(X\left(t',z,s\right),t'\right)\right| dt' \\ &+ \int_s^t \left|\mathbf{v}_n\left(X\left(t',z,s\right),t'\right) - \mathbf{v}\left(X\left(t',z,s\right),t'\right)\right| dt' \end{aligned}$$

For the last term in the right hand side of (3.73) we have:

$$\int_s^t \left|\mathbf{v}_n\left(X\left(t',z,s\right),t'\right) - \mathbf{v}\left(X\left(t',z,s\right),t'\right)\right| dt' \leq T\left\|\mathbf{v}_n - \mathbf{v}\right\|_\infty \qquad (3.74)$$

using the lemma 3.3.5 for the first term in the right hand side of (3.73) we obtain:

$$\begin{aligned} &\int_s^t \left|\mathbf{v}_n\left(X_n\left(t',z,s\right),t'\right) - \mathbf{v}_n\left(X\left(t',z,s\right),t'\right)\right| dt' \qquad (3.75)\\ &\leq K\left\|\omega_n^0\right\|_\infty \int_s^t \mathbf{\Phi}\left(\left|X_n\left(t',z,s\right) - X\left(t',z,s\right)\right|\right) dt' \end{aligned}$$

by using the following estimate

$$\Phi(r) \leq (-\ln\varepsilon)\, r + \varepsilon;\ \text{for all } r > 0 \text{ and } 0 < \varepsilon < 1 \qquad (3.76)$$

we obtain

$$|X_n(t,z,s) - X(t,z,s)| \leq T\left(\|\mathbf{v}_n - \mathbf{v}\|_\infty + C'\varepsilon\right)\frac{e^{C'L_\varepsilon T}}{C'L_\varepsilon} \tag{3.77}$$

where $L_\varepsilon = -\ln\varepsilon\ \forall\varepsilon < 1$, and C' is a canstant depending only on $\|\omega_0\|_\infty$.

Taking the limit in (3.77) when $n \longrightarrow \infty$, we find

$$\lim_{n\longrightarrow\infty}\sup_{t,y,s}|X_n(t,z,s) - X(t,z,s)| \leq T\varepsilon\frac{e^{C'L_\varepsilon T}}{L_\varepsilon} = T\frac{\varepsilon^{1-C'T}}{L_\varepsilon}\ \forall\varepsilon > 0$$

for T small ($C'T < 1$), we have:

$$|X_n(t,z,s) - X(t,z,s)| \longrightarrow 0, \text{ when } n \longrightarrow \infty \tag{3.78}$$

uniformly in t, z and s.

Since $\omega_n^1 = \Lambda\left(\omega_n^0\right)$ and $\omega^1 = \Lambda\left(\omega^0\right)$, by the formula (3.40), we have

$$\begin{aligned}\left|\omega_n^1(X_n,t) - \omega^1(X,t)\right| &= |\omega_0(X_n(0,z,t)) - \omega_0(X(0,z,t))| \\ &\leq H_x^{\delta"}(\omega_0)\,|X_n(0,z,t) - X(0,z,t)|^{\delta"} \\ &\leq |\omega_0|_{\delta",Q_T}\,|X_n(0,z,t) - X(0,z,t)|^{\delta"}\end{aligned} \tag{3.79}$$

then

$$\left\|\omega_n^1 - \omega^1\right\|_{\infty,Q_T} \leq |\omega_0|_{\delta",Q_T}\,|X_n(0,z,t) - X(0,z,t)|^{\delta"} \tag{3.80}$$

taking the limit in (3.80) when $n \longrightarrow \infty$, we prove ω_n^1 converge to ω^1 in the topology of $C(Q_T)$. which proves the Lemma. We can now apply the Schauder fixed point theorem, and conclude that there exists a fixed point $\omega \in S$, $\Lambda(\omega) = \omega$. Since $\omega \in C^{\delta"}(Q_T)$ by the lemma 3.3.6, we have $\mathbf{v} \in C^{1+\varepsilon,\varepsilon}(\Omega \times [0,T])$ for $0 < \varepsilon < \delta"$. □

Lemma 3.3.17 *The derivative in time of the velocity* $\mathbf{v}$ *exists and belongs to* $C(Q_T)$.

Proof By (3.33) the velocity is given

$$\mathbf{v}(z,t) = \text{curl}_z \int_\Omega G(z;p)\,\overline{\omega}(p,t)\,dp \tag{3.81}$$

we set $\Upsilon(\overline{\omega}) = \int_\Omega G(z;p)\,\overline{\omega}(p,t)\,dp$; $\mathbf{v} = \text{curl}_z\,\Upsilon(\overline{\omega})$.

For a function $\Psi \in C^2(\Omega)$, Ψ periodic in x, we have:

$$(\mathbf{v},\Psi) = (\operatorname{curl} \Upsilon(\overline{\omega}),\Psi) = (\Upsilon(\overline{\omega}), \operatorname{curl} \Psi) = (\overline{\omega},\Upsilon(\operatorname{curl} \Psi)) \tag{3.82}$$

Taking the time derivative of (3.82) and using lemma 3.3.11, we obtain:

$$\begin{aligned}
\frac{\partial}{\partial t}(\mathbf{v},\Psi) &= \frac{\partial}{\partial t}(\overline{\omega},\Upsilon(\operatorname{curl} \Psi)) = \frac{\partial}{\partial t}(\omega - y,\Upsilon(\operatorname{curl} \Psi)) \\
&= \frac{\partial}{\partial t}(\omega,\Upsilon(\operatorname{curl} \Psi)) - \frac{\partial}{\partial t}(y,\Upsilon(\operatorname{curl} \Psi)) \\
&= \frac{\partial}{\partial t}(\omega,\Upsilon(\operatorname{curl} \Psi)) - \frac{\partial}{\partial t}(\operatorname{curl}(\Upsilon(y)),\Psi) \\
&= (\omega, \mathbf{v}\cdot\nabla\Upsilon(\operatorname{curl} \Psi)) - \left(\frac{\partial}{\partial t}\operatorname{curl}(\Upsilon(y)),\Psi\right) \\
&= (\omega\mathbf{v}, \nabla\Upsilon(\operatorname{curl} \Psi)) - \left(\frac{\partial}{\partial t}\operatorname{curl}(\Upsilon(y)),\Psi\right) \\
&= -(\operatorname{curl}\Upsilon(\operatorname{div}(\omega\mathbf{v})),\Psi) - \left(\frac{\partial}{\partial t}\operatorname{curl}(\Upsilon(y)),\Psi\right) \\
&= -(\operatorname{curl}\Upsilon(\operatorname{div}(\omega\mathbf{v})),\Psi)
\end{aligned} \tag{3.83}$$

because $\left(\frac{d}{dt}\operatorname{curl}(\Upsilon(y)),\Psi\right) = 0 \ \forall\Psi \in C^2(\Omega)$ .We have

$$\Upsilon(\operatorname{div}(f))(z) = -\int_\Omega \nabla_p G(z,p)\cdot f(p)\,dp, \forall f \in C^1(\Omega) \tag{3.84}$$

We thus find

$$\frac{\partial}{\partial t}\mathbf{v} = -\operatorname{curl}\Upsilon(\operatorname{div}(\omega\mathbf{v})) \tag{3.85}$$

and the right-hand-side of (3.85) belongs to $C(Q_T)$. □

We also need to prove the existence of the pressure. This result is given by the following Lemma:

Lemma 3.3.18 *There exists a scalar function $p \in C^{1,0}(Q_T)$ such that $(\mathbf{v},p)$ is solution of problem (3.26).*

Proof For $\theta \in C^1(\Omega)$, θ periodic in x with $\theta = 0$ at $y = 0$ and $y = L_2$,we have

$$\frac{\partial}{\partial t}(\mathbf{v}, \operatorname{curl}\theta) = -\frac{\partial}{\partial t}(\operatorname{curl}\mathbf{v},\theta) = -\frac{\partial}{\partial t}(\omega - y,\theta) = -\frac{\partial}{\partial t}(\omega,\theta) \tag{3.86}$$

using lemma 3.3.7,we obtain:

$$\frac{\partial}{\partial t}(\mathbf{v}, \operatorname{curl}\theta) = -(\omega, \mathbf{v}\cdot\nabla\theta) = (\operatorname{curl}\mathbf{v}+y, \mathbf{v}\cdot\nabla\theta) \tag{3.87}$$

$$= -(\operatorname{curl}\mathbf{v}, \mathbf{v}\cdot\nabla\theta) - (y, \mathbf{v}\cdot\nabla\theta) \tag{3.88}$$

or

$$(\operatorname{curl}\mathbf{v}, \mathbf{v}\cdot\nabla\theta) = ((\mathbf{v}\cdot\nabla)\mathbf{v}, \operatorname{curl}\theta) \tag{3.89}$$

and

$$(y, \mathbf{v}\cdot\nabla\theta) = \left(y\mathbf{v}^{\perp}, \operatorname{curl}\theta\right) \tag{3.90}$$

Then

$$\frac{\partial}{\partial t}(\mathbf{v}, \operatorname{curl}\theta) = -((\mathbf{v}\cdot\nabla)\mathbf{v}, \operatorname{curl}\theta) - \left(y\mathbf{v}^{\perp}, \operatorname{curl}\theta\right) \tag{3.91}$$

we can written (3.91) as

$$\left(\frac{\partial\mathbf{v}}{\partial t} + (\mathbf{v}\cdot\nabla)\mathbf{v} + \mathbf{y}\mathbf{v}^{\perp}, \operatorname{curl}\theta\right) = 0 \tag{3.92}$$

these equality implie, $\exists p \in C^{1,0}(\Omega)$ such that:

$$\frac{\partial\mathbf{v}}{\partial t} + (\mathbf{v}\cdot\nabla)\mathbf{v} + \mathbf{y}\mathbf{v}^{\perp} + \nabla p = 0$$

As we announced in Theorem3.2.1., the solution (u, p) is unique. The proof of the uniqueness is classical, one can chose two different solutions and taking the difference between them, prove that the difference vanishes. Indeed,we suppose that there two solutions $\mathbf{v}_j$ $(j = 1, 2)$ with the same initial velocity $\mathbf{v}_0 \in C^{1+\alpha,0}$.

The velocity $\mathbf{v}_j$ solve the $2D$ barotropic equation in a distribution sense

$$\begin{cases} \dfrac{\partial\mathbf{v}_j}{\partial t} + (\mathbf{v}_j\cdot\nabla)\mathbf{v}_j + \mathbf{y}\mathbf{v}_j^{\perp} = -\nabla p_j,\ j = 1, 2 \\ \operatorname{div}\mathbf{v}_j = 0 \end{cases} \tag{3.93}$$

Let $U = \mathbf{v}_1 - \mathbf{v}_2$ and

$$E(t) \equiv \int_{\Omega} (U(x, y, t))^2 \, dxdy = \|U\|^2_{L^2(\Omega)} < \infty \tag{3.94}$$

U satisfies the following equation:

$$\frac{\partial U}{\partial t} + (\mathbf{v}_1.\nabla)U + (U.\nabla)\mathbf{v}_2 + \mathbf{y}U^{\perp} = -\nabla(p_1 - p_2) \tag{3.95}$$

in the sens of distribution, taking the L^2 inner product of this equation with U and integrating by parts give

$$\frac{1}{2}\frac{d}{dt}\|U\|^2_{L^2(\Omega)}-\frac{1}{2}\int_\Omega U^2 \operatorname{div}\mathbf{v}_1 dxdy+\int_\Omega (U.\nabla)\mathbf{v}_2 U dxdy+\int_\Omega yU^\perp U dxdy=\int_\Omega (p_1-p_2)\operatorname{div}(U)\,dxdy \tag{3.96}$$

we use the incompressibility condition in the last equation we obtain:

$$\frac{1}{2}\frac{d}{dt}\|U\|^2_{L^2(\Omega)}+\int_\Omega (U.\nabla)\mathbf{v}_2 U dxdy=0 \tag{3.97}$$

we have

$$\|(U.\nabla)\mathbf{v}_2\|_{L^2(\Omega)}\leq \|U\|_{L^2(\Omega)}\|\nabla\mathbf{v}_2\|_{L^\infty(\Omega)}$$

and this implies by Cauchy-Schwarz

$$\frac{1}{2}\frac{d}{dt}\|U\|^2_{L^2(\Omega)}=-\int_\Omega (U.\nabla)\mathbf{v}_2 U dxdy\leq \|U\|^2_{L^2(\Omega)}\|\nabla\mathbf{v}_2\|_{L^\infty(\Omega)} \tag{3.98}$$

by the Gronwall lemma, we conclude that $\|U\|^2_{L^2(\Omega)}=0\ \forall t\in[0,T]$ so that $\mathbf{v}_1=\mathbf{v}_2$ almost everywhere and by continuity of velocity we have equality everywhere in Q_T.

We can use the second following prove in the case where $\nabla\mathbf{v}\notin L^\infty(\Omega)$. The HÖlder inequality in (3.97) implies that

$$\frac{1}{2}\frac{d}{dt}\|U\|^2_{L^2(\Omega)}\leq \|\nabla\mathbf{v}_2\|_{L^p(\Omega)}\|U(.,t)\|^{\frac{2}{p}}_{L^\infty(\Omega)}\|U\|^{2\left(\frac{p-1}{p}\right)}_{L^2(\Omega)} \tag{3.99}$$

By using the expression of velocity in (3.31) , we can show the following estimate:

$$\|\nabla\mathbf{v}(.,t)\|_{L^p(\Omega)}\leq pK'\left(\|\omega_0\|_{L^\infty(\Omega)}\right)\quad\forall p\in[2,+\infty) \tag{3.100}$$

and by using the Lemma 3.3.5 we have the following estimate

$$\|\mathbf{v}(.,t)\|_{L^\infty(\Omega)}\leq K''\left(\|\omega_0\|_{L^\infty(\Omega)}\right) \tag{3.101}$$

Finally we have

$$\frac{1}{2}\frac{d}{dt}\|U\|^2_{L^2(\Omega)}\leq K'''\|U\|^{2-\frac{2}{p}}_{L^2(\Omega)} \tag{3.102}$$

or

$$\frac{d}{dt}\|U\|^2_{L^2(\Omega)}\leq pK'''.\|U\|^{2-\frac{2}{p}}_{L^2(\Omega)} \tag{3.103}$$

where $K''' = 2K'\left(\|\omega_0\|_{L^\infty(\Omega)}\right)K''\left(\|\omega_0\|_{L^\infty(\Omega)}\right)$ is positive constant depend only of $\|\omega_0\|_{L^\infty(\Omega)}$.

We want to conclude that $E(t) = \|U\|^2_{L^2(\Omega)} = 0$ for all $t > 0$. Because $E(0) = 0$ and $E(T) = 0$ is a trivial solution to inequality (3.103). However this inequality does note have unique solution. However, the maximal solution $\overline{E}(t) = (K'''t)^p$ and any solution $E(t)$ of (3.103) satisfies $E(t) \leq \overline{E}(t)$. Now we take an interval $[0, T^\star]$ such that $K'''T^\star < \frac{1}{2}$. We have

$$E(t) \leq \left(\frac{1}{2}\right)^p \searrow 0 \text{ as } p \nearrow \infty \tag{3.104}$$

so $E(t) \equiv 0, \forall t \in [0, T^\star]$. Repeating these arguments, we conclude that $E(t) = 0$, $\forall t \in [0, T]$ so that $\mathbf{v}_1 = \mathbf{v}_2$ almost everywhere and by continuity of velocity we have equality everywhere in Q_T. □

Lemma 3.3.19 *If* $\mathbf{v}$ *and* p *satisfy* (3.26)*, then:*

$$\begin{cases} \Delta p = & -\sum_{1\leq i,j\leq 2} \frac{\partial \mathbf{v}_i}{\partial x_j}\frac{\partial \mathbf{v}_j}{\partial x_i} - \operatorname{div}\left(y\mathbf{v}^\perp\right) \\ \frac{\partial p}{\partial n} = & \sum_{1\leq i,j\leq 2} \mathbf{v}_j \frac{\partial \mathbf{v}_i}{\partial x_j} n_i - yun_1 \text{ on } \Gamma_2 = \{y = 0, \quad y = Y\} \\ p & \text{periodic in } x \end{cases} \tag{3.105}$$

Proof The first equation in (3.105) is immediately obtained by applying the divergence operator to the first equation in (3.26), the second equation in (3.105) is obtained by taking the scalar product of the first equation in (3.26) with n on Γ_2. □

Remark 3.3.20 *The probleme* (3.105) *has a unique solution up to a function in time.*

In the next chapter, we study the numerical methods needed for solving the equatorial beta-plane barotropic equations.

Chapter 4

Numerical Methods

In Khouider and Majda [28], Equations (2.50) are solved with the non-oscillatory central scheme of Levy and Tadmor [17]. Here we propose to develop other high order and conservative numerical methods for the barotropic Equations (2.50) to compare and analyze the behavior of some of their simple exact and asymptotic solutions. Namely we consider two different numerical approaches: The Arakawa Jacobian method [1], which conserves both energy and enstrophy and a fourth-order ENO scheme of Osher and Shu [41]. The latter is originally designed for hyperbolic conservation laws as well as the Hamilton-Jacobi equations.It is also used to track sharp fronts.

4.1 Finite Differences

We define the first order forward difference approximation of u' at point x as :

$$u'(x) = \frac{u(x+h) - u(x)}{h} + O(h) \tag{4.1}$$

Likewise, we can define the first order backward difference approximation of u' at point x as :

$$u'(x) = \frac{u(x) - u(x-h)}{h} + O(h) \tag{4.2}$$

and the second order central difference approximation of u' at point x as

$$u'(x) = \frac{u(x+h) - u(x-h)}{2h} + O\left(h^2\right) \tag{4.3}$$

4.2 High-order approximations

Here we give a second-order approximation of the second derivative and a fourth-order approximation of the first and second derivative, respectively,

$$u''(x) = \frac{u(x+h) - 2u(x) + u(x-h)}{h^2} + O\left(h^2\right) \tag{4.4}$$

$$u'(x) = \frac{-u(x+2h) + 8u(x+h) - 8u(x-h) + u(x-2h)}{12h^2} + O\left(h^4\right) \tag{4.5}$$

$$u''(x) = \frac{-u(x+2h) + 16u(x+h) - 30u(x) - 16u(x-h) + u(x-2h)}{12h^2} + O\left(h^4\right) \tag{4.6}$$

Using this approch, a linear differential equation may be transformed to a finite linear system and solved with a method from linear Algebra. (Gaus elimination, LU Factorization, iterative methods .....).

The most widely used numerical methods for solving differentially equation for pratical applications involve the use of the Fast Fourier Transform (FFTs) which is a spectral method. We shall use these method for solving the Poisson equation in (2.50) .

4.3 Stability, Consistency and Convergence

In this section we give the definition of stability, consistency and convergence, these three important concepts are often used in numerical simulations of ODEs and PDEs. For more details see [23, 33].

Suppose we are given a well-posed problem that consist of a partial differential equation

$$\begin{cases} \dfrac{\partial u}{\partial t} = Lu \\ u(0,x) = u_0 \\ \text{and appropriate boundary condition} \end{cases} \tag{4.7}$$

where L is a differential operateur and u_0 is the initial conditions.

We are interested in a numerical scheme based on the finite difference method to solve the well-posed problem (4.7) .

Let $v(x,t)$ be the exact solution of the problem (4.7). The numerical solution of this equation via finite differences requires the replacement of continuous derivatives

with discrete approximations, and the confinement with the solution of a problem at a discret set of space and time points. Hence the numerical solution denoted by u will be determined at the discrete space points $x_j = j\Delta x$, and time points $t_n = n\Delta t$. We will us the notation $u_j^n = u\left(x_j, t_n\right)$.

The approximation must be consistent, stable and convergent to be useful in modeling physical problems. We now give the definition of these important concepts.

4.3.1 Convergence

Let $e_j^n = u_j^n - v_j^n$ denote the error between the numerical and analytical solution of the PDE at time t_n and point x_j . If this error tends to 0 as the grid and time steps are decreased, the finite difference solution converges to the analytical solution. Moreover, a finite difference scheme is said to be convergent of order (p, q) if

$$\|e\| \leq O\left((\Delta t)^p, (\Delta x)^q\right) \tag{4.8}$$

as $\Delta t, \Delta x \longrightarrow 0$.

4.3.2 Truncation Error

If the analytical solution is inserted in the finite defference scheme, we expect a small residual to remain. This residual characterizes the error in approximating the continuous form by a discrete form. By performing a Taylor series analysis we can derive an expression for the residual in terms of higher order derivatives of the solution.

4.3.3 Consistency

The notion of consistency adresses the problem of whether the finite difference approximation is really representing the partial differential equations. We say that a finite difference approximation is consistent with a differential equation if the discrete form equation converges to the orginal equation as the time and space grid are refined. Hence, if the trunction error goes to zero as $\Delta t, \Delta x \longrightarrow 0$, we conclude that the scheme is consitent.

Example 4.3.1 *we consider the scalar advection equation in one single space dimension*

$$\frac{\partial u}{\partial t} + c\frac{\partial u}{\partial x} = 0 \tag{4.9}$$

where $c > 0$ is the advection speed. A simple finite difference scheme that would advance the solution in time for time level n to $n+1$ is to use a Forward Euler scheme for the time derivative, and a backward Euler scheme for the space derivative. We get the following approximation to the PDE at point (x_j, t_n)

$$\frac{u_j^{n+1} - u_j^n}{\Delta t} + c\frac{u_j^n - u_{j-1}^n}{\Delta x} = 0 \tag{4.10}$$

Equation (4.10) provides a simple formula for updating the solution at time level $n+1$ from the values at time n

$$u_j^{n+1} = (1-\mu)\, u_j^n + \mu u_{j-1}^n \tag{4.11}$$

where

$$\mu = \frac{c\Delta t}{\Delta x} \tag{4.12}$$

We now evaluate the consistency of the scheme (4.10). We let

$$P\varphi = \frac{\partial \varphi}{\partial t} + c\frac{\partial \varphi}{\partial x}$$

and

$$P_{\Delta x, \Delta t}\varphi = \frac{\varphi_j^{n+1} - \varphi_j^n}{\Delta t} + c\frac{\varphi_j^n - \varphi_{j-1}^n}{\Delta x}$$

where φ is a smooth function and $\varphi_j^n = \varphi(x_j, t_n)$. We begin by setting the Taylor expansion of the function φ in t and x about (x_n, t_n)

$$\varphi_j^{n+1} = \varphi_j^n + (\Delta t)\,\varphi_t + \frac{1}{2}(\Delta t)^2\,\varphi_{tt} + O(\Delta t)^3$$

$$\varphi_j^n = \varphi_{j-1}^n + (\Delta x)\,\varphi_x + \frac{1}{2}(\Delta x)^2\,\varphi_{xx} + O(\Delta x)^3$$

This give us

$$P_{\Delta x, \Delta t}\varphi = \varphi_t + c\varphi_x + \frac{1}{2}(\Delta t)\,\varphi_{tt} + \frac{1}{2}c(\Delta x)\,\varphi_{xx} + O(\Delta t)^2 + O(\Delta x)^2.$$

Thus

$$P_{\Delta x, \Delta t}\varphi - P\varphi = \frac{1}{2}(\Delta t)\,\varphi_{tt} + \frac{1}{2}c(\Delta x)\,\varphi_{xx} + O(\Delta t)^2 + O(\Delta x)^2 \tag{4.13}$$

and

$$P_{\Delta x, \Delta t}\varphi - P\varphi \longrightarrow 0 \text{ as } (\Delta t, \Delta x) \longrightarrow 0.$$

Thus, this scheme is consistent. All terms on the right hand side are part of the truncation error.

4.3.4 Stability

Our primary concern here is to make sure that numerical errors do not swamp the analytical solution. One way to ensure that is to require the numerical solution to remain bounded by the initial data. Hence a definition of stability is to require the following.

$$\|u^n\| \leq C_T \|u_0\| \tag{4.14}$$

where C_T depends only of the final integration time T, $(0 \leq t_n \leq T)$.

4.3.5 Lax-Richtmeyer Equivalence Theorem

The Lax-Richtmyer Equivalence Theorem is often called the Fundamental Theorem of Numerical Analysis, even though it is only applicable to the small subset of linear numerical methods for well-posed, linear partial differential equations. We have the following equivalence:

$$\text{consistency} + \text{stability} \Leftrightarrow \text{convergence}.$$

This theorem's value is that it guarantees convergence provided two simpler conditions are satisfied, namely consistency and stability.

4.4 The CFL condition

A neccessary stability condition for any numerical method is that the domain of dependance of the finite difference method should include the domain of dependence of the PDE, at least in the limit $\Delta t, \Delta x \longrightarrow 0$. This condition is known as the CFL condition after Courant, Fredrich and Levy. The CFL condition is a necessary condition for stability, not sufficient. In the example above the variable μ in (4.12) is the dimensionless number, called the Courant number. It will figure prominently in the study of the stability of the scheme.

The courant number has different forms for different PDEs. We have the following equivalence

$$0 \leq \mu \leq 1 \Leftrightarrow \text{ CFL condition is achieved.}$$

4.5 Poisson's equation

We consider the poisson equation on a 2-dimensional x-periodic domain $D = [0, X] \times [-Y, Y]$:

$$\begin{cases} \Delta\psi(x,y) = \zeta(x,y) \\ \psi(0,y) = \psi(P,y) \\ \zeta(0,y) = \zeta(P,y) \end{cases} \tag{4.15}$$

where $\zeta(x,y) = \xi(x,y) - y$. We may represent the 2-dimensional Laplacian using the second and the fourth order centred finite differences in both directions, respectively as

$$\Delta_{i,j}\psi = \frac{\psi_{i+1,j} - 2\psi_{i,j} + \psi_{i-1,j}}{\Delta x^2} + \frac{\psi_{i,j+1} - 2\psi_{i,j} + \psi_{i,j-1}}{\Delta y^2} = \xi_{i,j} - y_j. \tag{4.16}$$

or

$$\begin{aligned} \Delta_{i,j}\psi = & \frac{-\psi_{i+2,j} + 16\psi_{i+1,j} - 30\psi_{i,j} - 16\psi_{i-1,j} - \psi_{i-2,j}}{12\Delta x^2} \\ & + \frac{-\psi_{i,j+2} + 16\psi_{i,j+1} - 30\psi_{i,j} + 16\psi_{i,j-1} - \psi_{i,j-2}}{12\Delta y^2} \\ & = \xi_{i,j} - y_j, \end{aligned} \tag{4.17}$$

where $\Delta x = \frac{X}{N}$ and $\Delta y = \frac{2Y}{M}$ for an $N \times M$ grid.

We need these two discretization for solving the system (2.50) by the second-order method of Arakawa Jacobian and the fourth order method of ENO-4 developed in the next sections. The idea of the spectral method is to use a truncated series of orthogonal functions in order to represent the solution of the problem in (4.15). Due to the speed of the Fast Fourier Transform (FFT) algorithms [46], the discrete version of the Fourier transform has become a very useful method. The discrete Fourier transform of a funcion $u(x,y)$ with respect to x is defined by

$$\mathcal{F}(u_{i,k}) = \hat{u}_{i,k} = \sum_{j=0}^{N-1} u_{i,k} e^{-i2\pi jl/N} \tag{4.18}$$

and the inverse discrete Fourier transform,

$$\mathcal{F}^{-1}(\hat{u}_{l,k}) = u_{j,k} = \frac{1}{N} \sum_{l=0}^{N-1} \hat{u}_{l,k} e^{i2\pi jl/N} \tag{4.19}$$

An approximation to the second derivative of a function $u(x)$ can be represented using the discrete Fourier transform as

$$\mathcal{F}\left(u''_{j,k}\right) = \lambda_k \hat{u}_{l,k}, \tag{4.20}$$

where

$$\lambda_k = \frac{2\left(\cos\left(2\pi k/N\right) - 1\right)}{\left(\Delta x\right)^2} \tag{4.21}$$

We use the discrete Fourier transform described above to transfom Poisson's equation into a second order ordinary differential equation:

$$\lambda_k \hat{\psi}_{l,k} + \frac{\hat{\psi}_{l,k+1} - 2\hat{\psi}^n_{l,k} + \hat{\psi}_{l,k-1}}{\Delta y^2} = \hat{\xi}_{i,j} - y_j, \tag{4.22}$$

or

$$\lambda_k \hat{\psi}_{l,k} + \frac{-\hat{\psi}_{i,j+2} + 16\hat{\psi}_{i,j+1} - 30\hat{\psi}_{i,j} + 16\hat{\psi}_{i,j-1} - \hat{\psi}_{i,j-2}}{12\Delta y^2} = \hat{\xi}_{i,j} - y_j, \tag{4.23}$$

The central finite difference formula in Eqts (4.22) and (4.23) are second and fourth order in the spatial direction y, respectively. The FFT method is infinite order. The tridiagonal (4.22) and pentadiagonal (4.23) systems can be solved using the transformed boundary condition via Gaussian elimination and LU Factorization, respectively. Application of the inverse discrete Fourier transform yields the solution to the Poisson's equation.

4.6 The Arakawa method for the barotropic equation

4.6.1 Free Equatorial Barotropic Vorticity Equation

The free equatorial barotropic vorticity equation can be written either in an advective form

$$\frac{\partial \xi}{\partial t} + u\frac{\partial \xi}{\partial x} + v\frac{\partial \xi}{\partial y} = 0, \tag{4.24}$$

or in the conservative form,

$$\frac{\partial \xi}{\partial t} + \frac{\partial\left(u\xi\right)}{\partial x} + \frac{\partial\left(v\xi\right)}{\partial y} = 0. \tag{4.25}$$

Even though it is simple to code the advective form (4.24) is not often used in practice because it lacks the conservative property and may result in instabilities which can grow with time. The numerical treatment of the conservative form, on the other hand, allows solutions that contain shocks. Khouider and Majda [28] adapted a central scheme [31] using both the advective and conservative forms (4.24)-(4.25) to avoid this problem. At each time step a piecewise approximation uses staggered averaging results in smooth

numerical fluxes, to avoid discontinuous Riemann fans. The results of Khouider and Majda [28] are used as a benchmark to validate the two methods considered here. We consider the vorticity-stream function equation in the generic form,

$$\frac{\partial \xi}{\partial t} + J(\psi, \xi) = 0. \tag{4.26}$$

Under suitable boundary conditions, this equation has the useful feature of conserving both domain integrated enstrophy and domain integrated kinetic energy. It is natural to require these same conservation properties during the discretization of the Jacobian in the (4.26). In additions to conserving these important physical quantities, this would guaranty the stability of the numerical scheme. The method used in [28] ensures stability by relying on the machinery of high-resolution methods for conservation laws. The Arakawa Jacobian method on the other hand achieves stability by conserving energy and enstrophy.

4.6.2 Arakawa Jacobian

A naive way to discretize the Jacobian would be to use centred differences to approximate the derivatives in

$$J_1(\psi, \xi) = \frac{\partial \psi}{\partial x}\frac{\partial \xi}{\partial y} - \frac{\partial \xi}{\partial x}\frac{\partial \psi}{\partial y}. \tag{4.27}$$

However, it was noted by Phillips [45] that this scheme is subject to instabilities stemming from the misrepresentation of wavelengths shorter than two grid intervals. This misrepresentation is called aliasing. It is not due to a poor choice of boundary conditions or to an inappropriately large time step but is rather an inherent feature of the scheme. The instabilities resulting from aliasing can grow without bound in a finite amount of time.

Alternatively, one would discretize either of the following equivalent formulations of the Jacobian.

$$\begin{aligned} J_2(\psi, \xi) &= \frac{\partial}{\partial x}\left(\psi\frac{\partial \xi}{\partial y}\right) - \frac{\partial}{\partial y}\left(\psi\frac{\partial \xi}{\partial x}\right), \\ J_3(\psi, \xi) &= \frac{\partial}{\partial y}\left(\xi\frac{\partial \psi}{\partial x}\right) - \frac{\partial}{\partial x}\left(\xi\frac{\partial \psi}{\partial y}\right). \end{aligned} \tag{4.28}$$

Using a judicious combination of J_1, J_2 and J_3, Arakawa was able to propose a discrete Jacobian that conserves the numerical analogues of the domain-integrated kinetic

energy, domain-integrated enstrophy, and average wavenumber. We introduce the standard notation of centred differences:

$$\begin{aligned} \delta_i(\psi)^j &= \psi_{i+1,j} - \psi_{i-1,j}, \\ \delta_j(\xi)^i &= \xi_{i,j+1} - \xi_{i,j-1}. \end{aligned} \tag{4.29}$$

The most obvious discretization of the Jacobian is given by

$$J_{++}(\psi,\xi) = \frac{1}{\Delta x \Delta y}\left(\delta_i(\psi)^j \delta_j(\xi)^i - \delta_j(\psi)^i \delta_i(\xi)^j\right), \tag{4.30}$$

which corresponds to centered difference for the continuum form $J_1(\psi,\xi)$. The flux form Jacobian,

$$J_{+\times}(\psi,\xi) = \frac{1}{\Delta x \Delta y}\left(\delta_i\left(\psi\delta_j(\xi)^i\right)^j - \delta_j\left(\psi\delta_i(\xi)^j\right)^i\right), \tag{4.31}$$

corresponds to the continuum form $J_2(\psi,\xi)$ and the flux form Jacobian,

$$J_{\times+}(\psi,\xi) = \frac{1}{\Delta x \Delta y}\left(\delta_j\left(\xi\delta_i(\psi)^j\right)^i - \delta_i\left(\xi\delta_j(\psi)^i\right)^j\right), \tag{4.32}$$

corresponds to the continuum form $J_3(\psi,\xi)$. As can be seen from the figure below, a nine point stencil is required for this Jacobian.

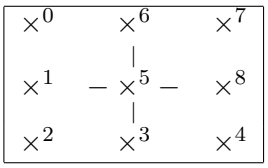

Five point stencil for centred differences Jacobian

The finite difference analogue of the Jacobian at the grid (i,j) may be written, in the most general form

$$J_{i,j}(\psi,\xi) = \sum_{i',j'}\sum_{i'',j''} C_{j,k,i',j',i'',j''}\xi_{i+i',j+j'}\psi_{i+i'',j+j''}, \tag{4.33}$$

where $\xi_{i+i',j+j'}$ is the vorticity at a neighboring grid point $(i+i', j+j')$ and $\psi_{i+i'',j+j''}$ is the stream function at a neighboring grid point $(i+i'', j+j'')$. If we define a linear combination of velocity components by finite differences of the stream function

$$a_{i,j,i+i',j+j'} = \sum_{i'',j''} C_{i,j,i',j',i'',j''}\psi_{i+i'',j+j''}, \tag{4.34}$$

Multiplying (4.33) by $2\xi_{i,j}$, we obtain

$$2\xi_{i,j}J_{i,j}(\psi,\xi) = \sum_{i',j'} 2a_{i,j,i+i',j+j'}\xi_{i,j}\xi_{i+i',j+j'}, \tag{4.35}$$

From the BVE in (2.50), we see that the left hand side of (4.35) is time change of $\xi_{i,j}^2$ due to advection. Therefore, the term $2a_{i,j,i+i',j+j'}\xi_{i,j}\xi_{i+i',j+j'}$ can be interpreted as the enstrophy gain at the grid point (i,j) due to interaction with the grid point $(i+i',j+j')$. Similarly, $2a_{i+i',j+j',i,j}\xi_{i+i',j+j'}\xi_{i,j}$ can be interpreted as the enstrophy gain at the grid point $(i+i',j+j')$ due to interaction with the grid point (i,j). These two quantities must have the same magnitude and opposite sign, regardless of the values of $\xi_{i,j}$ and $\xi_{i+i',j+j'}$, in order to avoid false production of enstrophy. Therfore, we have the requirement

$$a_{i+i',j+j',i,j} = -a_{i,j,i+i',j+j'} \tag{4.36}$$

if the enstrophy is to be conserved in the finite difference scheme. Consider again the general formulation of the finite difference Jacobian as a linear combination of $J_{i,j}^{++}$, $J_{i,j}^{+\times}$, and $J_{i,j}^{\times+}$:

$$J_{i,j}(\psi,\xi) = \alpha J_{i,j}^{++}(\psi,\xi) + \beta J_{i,j}^{+\times}(\psi,\xi) + \gamma J_{i,j}^{\times+}(\psi,\xi) \tag{4.37}$$

where $\alpha+\beta+\gamma = 1$. Using this linear combination, we calculate the following coefficients representing interactions of the grid point (i,j) with its neighbours:

$$a_{i,j,i+1,j} = \frac{1}{4\Delta x\Delta y}\left[-\alpha\left(\psi_{i,j+1}-\psi_{i,j-1}\right) - \gamma\left(\psi_{i+1,j+1}-\psi_{i+1,j-1}\right)\right] \tag{4.38}$$

$$a_{i,j,i-1,j} = \frac{1}{4\Delta x\Delta y}\left[\alpha\left(\psi_{i,j+1}-\psi_{i,j-1}\right) + \gamma\left(\psi_{i-1,j+1}-\psi_{i-1,j-1}\right)\right] \tag{4.39}$$

$$a_{i,j,i,j+1} = \frac{1}{4\Delta x\Delta y}\alpha\left[\left(\psi_{i+1,j}-\psi_{i-1,j}\right) + \gamma\left(\psi_{i+1,j+1}-\psi_{i-1,j+1}\right)\right] \tag{4.40}$$

$$a_{i,j,i,j-1} = \frac{1}{4\Delta x\Delta y}\left[-\alpha\left(\psi_{i+1,j}-\psi_{i-1,j}\right) - \gamma\left(\psi_{i+1,j-1}-\psi_{i-1,j-1}\right)\right] \tag{4.41}$$

$$a_{i,j,i+1,j+1} = \left[\frac{1}{4\Delta x\Delta y}\beta\left(\psi_{i+1,j}-\psi_{i,j+1}\right)\right] \tag{4.42}$$

$$a_{i,j,i-1,j-1} = \left[\frac{1}{4\Delta x\Delta y}\beta\left(\psi_{i-1,j}-\psi_{i,j-1}\right)\right] \tag{4.43}$$

$$a_{i,j,i-1,j+1} = \left[\frac{1}{4\Delta x\Delta y}\beta\left(\psi_{i-1,j}-\psi_{i,j-1}\right)\right] \tag{4.44}$$

$$a_{i,j,i+1,j-1} = \left[\frac{1}{4\Delta x\Delta y}\beta\left(\psi_{i,j-1} - \psi_{i+1,j}\right)\right] \tag{4.45}$$

From these equations, we can derive a subsequent set of equations for the interaction of neighbouring points with the grid point (i, j) :

$$a_{i+1,j,i,j} = \frac{1}{4\Delta x\Delta y}\left[\alpha\left(\psi_{i+1,j+1} - \psi_{i+1,j-1}\right) + \gamma\left(\psi_{i+1,j+1} - \psi_{i,j-1}\right)\right] \tag{4.46}$$

$$a_{i-1,j,i-1,j} = \frac{1}{4\Delta x\Delta y}\left[\alpha\left(\psi_{i-1,j+1} - \psi_{i,j-1}\right) - \gamma\left(\psi_{i,j+1} - \psi_{i,j-1}\right)\right] \tag{4.47}$$

$$a_{i,j+1,i,j} = \frac{1}{4\Delta x\Delta y}\alpha\left[\left(\psi_{i+1,j+1} - \psi_{i-1,j+1}\right) - \gamma\left(\psi_{i+1,j} - \psi_{i-1,j}\right)\right] \tag{4.48}$$

$$a_{i,j-1,i,j} = \frac{1}{4\Delta x\Delta y}\left[-\alpha\left(\psi_{i+1,j-1} - \psi_{i-1,j}\right) + \gamma\left(\psi_{i+1,j} - \psi_{i-1,j}\right)\right] \tag{4.49}$$

$$a_{i-1,j-1,i,j} = \left[\frac{1}{4\Delta x\Delta y}\beta\left(\psi_{i,j-1} - \psi_{i-1,j}\right)\right] \tag{4.50}$$

$$a_{i+1,j+1,i,j} = \left[\frac{1}{4\Delta x\Delta y}\beta\left(\psi_{i,j+1} - \psi_{i+1,j}\right)\right] \tag{4.51}$$

$$a_{i+1,j-1,i,j} = \left[\frac{1}{4\Delta x\Delta y}\beta\left(\psi_{i+1,j} - \psi_{i,j-1}\right)\right] \tag{4.52}$$

$$a_{i-1,j+1,i,j} = \left[\frac{1}{4\Delta x\Delta y}\beta\left(\psi_{i-1,j} - \psi_{i,j+1}\right)\right] \tag{4.53}$$

Comparaison of (4.38) with (4.46), (4.40) with (4.48), (4.42) with (4.51) and (4.53) with (4.44) reveals that

$$\alpha = \gamma \tag{4.54}$$

is required in order to satisfy (4.36) . Thus, the sheme $\alpha J_{i,j}^{++}\left(\psi,\xi\right) + \beta J_{i,j}^{+\times}\left(\psi,\xi\right) + \gamma J_{i,j}^{\times+}\left(\psi,\xi\right)$, where $2\alpha+\beta = 1$, is an enstrophy conserving scheme. In a similar way, it can be shown by considering the finite difference analogue of $\psi J\left(\psi,\xi\right)$ that

$$\alpha = \beta \tag{4.55}$$

$J(\psi,\xi)$	J^{++}	$J^{\times+}$	$J^{+\times}$	$\frac{J^{++}+J^{\times+}+J^{+\times}}{3}$
$J(\psi,\xi)=-J(\xi,\psi)$	$\surd$			$\surd$
K.E. conserved		$\surd$		$\surd$
Enstrophy conserved			$\surd$	$\surd$

Table 4.1: Properties of Typical Jacobians.

is required for conservation of the kinetic energy. Thus, the scheme $\alpha J_{i,j}^{++}(\psi,\xi) + \beta J_{i,j}^{+\times}(\psi,\xi) + \gamma J_{i,j}^{\times+}(\psi,\xi)$, where $2\alpha+\gamma=1$, is an energy conserving scheme. The scheme which satisfies both the conservation of enstrophy and the conservation of energy is given in the third column of Table 4.1.

$$\alpha=\beta=\gamma=\frac{1}{3} \tag{4.56}$$

As a consequence, We proved that the combination

$$J=\frac{1}{3}\left(J_{++}+J_{+\times}+J_{\times+}\right), \tag{4.57}$$

conserves both energy and ensotrophy as well as the mean wavenumber, which as already mentioned, prevents numerical instabilities from occurring. This is what is called the Arakawa Jacobian. A summary of conservation properties is contained in the Table 4.1.

4.6.3 Basic discretization

On a uniform grid with grid points $(x_i,y_j)=(x_0+ih,y_0+jh)$ $i=0,\cdots,N$, $j=0,\cdots,M$, we can discretize (2.50) in space by second-order centered finite differences combined with a second order Runge-Kutta predictor-corrector method in time:

$$\frac{\xi_{i,j}^{n+1}-\xi_{i,j}^{n}}{\Delta t}+J_{i,j}^{n}\left(\psi^{n},\xi^{n}\right)=0, \tag{4.58}$$

$$\Delta_{i,j}^{n}\psi^{n}=\frac{\psi_{i+1,j}^{n}-2\psi_{i,j}^{n}+\psi_{i-1,j}^{n}}{\Delta x^{2}}+\frac{\psi_{i,j+1}^{n}-2\psi_{i,j}^{n}+\psi_{i,j-1}^{n}}{\Delta y^{2}}=\xi_{i,j}^{n}-y_{j}. \tag{4.59}$$

Here $J_{i,j}^{n}$ is the Arakawa Jacobian given in (4.57). The use of the Arakawa Jacobian ensures conservation of discrete analogues of (2.52) and (2.53), as detailed in [1]. $\Delta_{i,j}^{n}$ is the usual five-point approximation of the Laplacian. The Arakawa method for the barotropic system (2.50) is achieved by combining the discretization equation of

potential vorticity in (4.58) with a solver for the stream-function Poisson equation in (4.59). We solve the difference equation in (4.59) by combining the FFT method for the periodic x-direction and a direct method in y [28]. The Poisson equation in (4.59) is closed by the periodic boundary conditions in x and the Neumann boundary condition in y,

$$\frac{\partial \psi}{\partial x}(x, \pm Y) = 0, \tag{4.60}$$

dictated by the no-flow condition in (2.51). The Fourier method,

$$\psi_{i,j} = \sum_{k=1}^{N} \overset{\wedge}{\psi}_{k,j} \exp\left(I\,(i-1)\,(k-1)\,2\pi\Delta x\right), \quad I^2 = -1, \tag{4.61}$$

applied to the difference equation in (4.59), leads to a tridiagonal system for each Fourier mode with the homogeneous Dirichlet boundary conditions, $\overset{\wedge}{\psi}_{k,0} = \overset{\wedge}{\psi}_{k,M} = 0$, for all the modes, $2 \leq k \leq N$, except for the first mode, $k = 1$. We obtain a boundary condition for the first mode by relying on the conservation of the zonal mean wind at the north-south boundaries. In fact, the zonal averaging of Equation (4.24) combined with the no-flow condition (2.51) leads to [28]

$$\frac{\partial}{\partial t}\left(\frac{1}{P}\int_0^P u\,(x, y, t)\,dx\right) = 0 \text{ at } y = \pm Y. \tag{4.62}$$

This condition is used during the coding of the Poisson solver. The complete algorithm for solving the barotropic system (2.38) is as follows: From ξ^n, compute ψ^n by inverting $\Delta^n_{i,j}\psi^n = \xi^n - y$, compute the Jacobian $J^n(\psi^n, \xi^n)$ then compute $\xi^{n+1} = \xi^n - \Delta t J^n(\psi, \xi)$, increment n and repeat the cycle. Homogeneous Dirichlet boundary conditions are used at the walls for the potential vorticity,

$$\overline{\omega} = \xi - y = 0 \text{ at } y = \pm Y, \tag{4.63}$$

and combined with periodic boundary conditions in x. The validation of Arakawa's method is given in Chapter 5.

4.7 Fourth-order Essentially Non-oscillatory scheme for the baroropic equations

Essentially non-oscillatory schemes were developed by Harten *et al.* in 1987 [19, 20] when working on the numerical solution of nonlinear hyperbolic conservation laws

(HCL). The solution of a system of HCL involves discontinuities. Interpolating across these discontinuities leads to Gibbs phenomenon which results in loss of accuracy and ultimately numerical instabilities. The ENO interpolation scheme is a data dependent, nonlinear reconstruction technique which can eliminate the Gibbs phenomenon. ENO schemes for Hamilton-Jacobi equations were developed in [41].

4.7.1 ENO Interpolation

The key idea is an adaptive stencil interpolation which automatically selects the locally smoothest region, and hence yields a uniformly high-order essentially non-oscillatory approximation for piecewise smooth functions. Given point values $G(x_j),\ j = 0, \pm1, \pm2, \cdots$ of a (piecewise smooth) function G at discrete nodes x_j, we associate an m-th degree polynomial $P_m^{j+\frac{1}{2}}$ with each interval $[x_j, x_{j+1}]$. The ENO scheme selects the smoothest possible region of the domain by choosing the $m+1$ interpolation points, in the neighbourhood of the cell $[x_j, x_{j+1}]$ (including x_j and x_{j+1}), that achieve the smallest divided differences $G[x_1, x_2, \cdots, x_k]$, of all order $k, 1 \leq k \leq m+1$.
1)$P_1^{j+\frac{1}{2}}\ (x) = G[x_i] + G[x_j, x_{j+1}](x - x_j) \quad k_{\min}^1 = j$
2) If $k_{\min}^{(m-1)}$ et $P_{m-1}^{j+\frac{1}{2}}\ (x)$ are both defined, then let:

$$a^{(m)} = G\left[x_{k_{\min}^{(m-1)}}, ..., x_{k_{\min}^{(m-1)}+m}\right],$$

$$b^{(m)} = G\left[x_{k_{\min}^{(m-1)}-1}, ..., x_{k_{\min}^{(p-1)}m-1}\right],$$

i) If $\left|a^{(m)}\right| \geq \left|b^{(m)}\right| \Longrightarrow c^{(m)} = b^{(m)},\ k_{\min}^{(m)} = k_{\min}^{(m-1)} - 1$ otherwise $c^{(m)} = a^{(m)},\ k_{\min}^{(m)} = k_{\min}^{(m-1)}$
ii) $P_m^{j+\frac{1}{2}}\ (x) = P_{m-1}^{j+\frac{1}{2}}\ (x) + c^{(m)} \prod_{i=k_{\min}^{(m-1)}}^{k_{\min}^{(m-1)}+m-1} (x - x_i)$

In the above procedure $G[...]$ are the usual Newton divided differences. Note that we start from the first degree polynomial $P_1^{j+\frac{1}{2}}$ with a stencil of two point, which would generate a first order monotone scheme in the procedure below.

The ENO interpolation procedure starts with a base stencil containing two grid points, then adaptively adds one point to the stencil at each stage, which is either the left neighboring point or the right neighboring point to the current stencil depending

on which would yield a smaller divided differences value. The ENO interpolation procedure results in a high order approximation that avoids spurious oscillations. More precisely, we can show that the total variation of the interpolation polynomial is at most $O(\Delta x^r), r > 0$ larger than the total variation of the piecewise smooth function being interpolated. Thus the ENO procedure is especially suited for problems with singular but piecewise smooth functions, such as solutions of nonlinear conservation laws and Hamilton-Jacobi equations. When combined with an exact or approximate Riemann solver the ENO reconstruction results in a TVB (total variation bounded) stable numerical scheme.

4.7.2 Construction of the fourth-order ENO polynomial

In what follows, we give explicit algorithms to compute Φ_x by ENO schemes of order $1, 2, 3$ and 4. In these algorithms, we use an integer index k^1 in generic formulas as:

$$\begin{cases} \text{if } k^1 = i-1 \text{ then the final result is } \Phi_x^- \\ \text{if } k^1 = i \qquad \text{then the final result is } \Phi_x^+ \end{cases}$$

The two-dimensional space is chosen and the mesh considered is presented in the following figure:

	$\circ$ $i,j+1$	
$\circ$ $i-1,j$	$\circ$ i,j	$\circ$ $i+1,j$
	$\circ$ $i,j-1$	

At a point (i, j) of the grid space and the Algorithm comput an approximation of $\Phi_x^{+,-}(x_i, y_j)$ following Shu and Osher (1989). The idea is to construct the polynomial interpolation of the solution as regular as possible and to get the drift $\Phi_x^{+,-}$. The same technique applied in the direction j, to compute $\Phi_y^{+,-}$.

ENO 1

1) $Q^0(x) = \Phi_{i,j}$

2) For $k^1 = \{i-1, i\}$ we compute:

a) $Q^1(x) = \dfrac{\Phi_{k^1+1,j} - \Phi_{k^1,j}}{\Delta x}(x - x_i)$.

b) $\begin{cases} \text{if } k^1 = i-1 \text{ then the final result is } \Phi_x^- = \dfrac{dQ^1}{dx} = \dfrac{\Phi_{i,j} - \Phi_{i-1,j}}{\Delta x}(x - x_i) \\ \text{if } k^1 = i \qquad \text{then the final result is } \Phi_x^+ = \dfrac{dQ^1}{dx} = \dfrac{\Phi_{i+1,j} - \Phi_{i,j}}{\Delta x}(x - x_i) \end{cases}$.

ENO 2

1) $Q^0(x) = \Phi_{i,j}$

2) For $k^1 = \{i-1, i\}$

a) $Q^1(x) = \dfrac{\Phi_{k^1+1,j} - \Phi_{k^1,j}}{\Delta x}(x - x_i)$.
$d_{i,j}^{(1)} = \dfrac{\Phi_{k^1+1,j} - \Phi_{k^1,j}}{\Delta x}$

b) We compute:

i) $\begin{cases} a^1 = \dfrac{\Phi_{k^1+1,j} - 2\Phi_{k^1,j} + \Phi_{k^1-1,j}}{2(\Delta x)^2} \\ b^1 = \dfrac{\Phi_{k^1+2,j} - 2\Phi_{k^1+1,j} + \Phi_{k^1,j}}{2(\Delta x)^2} \end{cases}$

ii) $C^1 = \begin{cases} a^1 & \text{if } \left|a^1\right| \le \left|b^1\right| \\ b^1 & \text{otherwise} \end{cases}$

$k^2 = \begin{cases} k^1 - 1 & \text{if } \left|a^1\right| \le \left|b^1\right| \\ k^1 & \text{otherwise} \end{cases}$

iii)

$$Q^2(x) = Q^1(x) + C^1\left(x^2 - (x_{k^1} + x_{k^1+1})x + x_{k^1}x_{k^1+1}\right)$$

c)

$$\frac{dQ^2}{dx} = \frac{dQ^1}{dx}(x_i) + C^1\left(2\left(i - k^1\right) - 1\right)\Delta x = d_{i,j}^{(2)}\left(k^1\right)$$

$$\begin{cases} \text{If } k^1 = i-1 \text{ then } \Phi_x^- = \dfrac{dQ^2}{dx} = d_{i,j}^{(1)} + C^1\Delta x \\ \text{If } k^1 = i \qquad \text{then } \Phi_x^+ = \dfrac{dQ^2}{dx} = d_{i,j}^{(1)} - C^1\Delta x \end{cases}$$

ENO 3

1) $Q^0(x) = \Phi_{i,j}$

2) For $k^1 = \{i-1, i\}$ we compute :

a) $Q^1(x) = \dfrac{\Phi_{k^1+1,j} - \Phi_{k^1,j}}{\Delta x}(x - x_i)$.

$\dfrac{dQ^1}{dx} = d_{i,j}^{(1)} = \dfrac{\Phi_{k^1+1,j} - \Phi_{k^1,j}}{\Delta x}$

b) We compute two iterations :

First step

i)

$$\begin{cases} a^1 = \dfrac{\Phi_{k^1+1,j} - 2\Phi_{k^1,j} + \Phi_{k^1-1,j}}{2(\Delta x)^2} \\ b^1 = \dfrac{\Phi_{k^1+2,j} - 2\Phi_{k^1+1,j} + \Phi_{k^1,j}}{2(\Delta x)^2} \end{cases}$$

ii)

$$C^1 = \begin{cases} a^1 & \text{if } \left|a^1\right| \leq \left|b^1\right| \\ b^1 & \text{otherwise} \end{cases}$$

$$k^2 = \begin{cases} k^1 - 1 & \text{if } \left|a^1\right| \leq \left|b^1\right| \\ k^1 & \text{otherwise} \end{cases}$$

$$d_{i,j}^{(2)}\left(k^1\right) = d_{i,j}^{(1)} + C^1\left(2\left(i - k^1\right) - 1\right)\Delta x$$

Second step

i)

$$\begin{cases} a^2 = \dfrac{\Phi_{k^2+2,j} - 3\Phi_{k^2+1,j} + 3\Phi_{k^2,j} + \Phi_{k^2-1,j}}{6(\Delta x)^3} \\ b^2 = \dfrac{\Phi_{k^2+3,j} - 3\Phi_{k^2+2,j} + 3\Phi_{k^2+1,j} + \Phi_{k^2,j}}{6(\Delta x)^3} \end{cases}$$

ii)

$$C^2 = \begin{cases} a^2 & \text{if } \left|a^2\right| \leq \left|b^2\right| \\ b^2 & \text{otherwise} \end{cases}$$

$$k^3 = \begin{cases} k^2 - 1 & \text{if } \left|a^2\right| \leq \left|b^2\right| \\ k^2 & \text{otherwise} \end{cases}$$

iii)

$$Q^3(x) = Q^2(x) + C^2(x - x_{k^2})(x - x_{k^2+1})(x - x_{k^2+2})$$

c)

$$\frac{dQ^3}{dx} = \frac{dQ^2}{dx}(x_i) + C^2\left(3\left(i-k^2\right)^2 - 6\left(i-k^2\right) + 2\right)(\Delta x)^2 = d_{i,j}^{(3)}\left(k^1, k^2\right)$$

$$d_{i,j}^{(3)}\left(k^1, k^2\right) = d_{i,j}^{(1)} + C^1\left(2\left(i-k^1\right) - 1\right)\Delta x + C^2\left(3\left(i-k^2\right)^2 - 6\left(i-k^2\right) + 2\right)(\Delta x)^2$$

$$\begin{cases} \text{If } k^1 = i-1 \text{ then } \Phi_x^- = \dfrac{dQ^3}{dx} = d_{i,j}^{(3)}\left(k^1, k^2\right) \\ \text{If } k^1 = i \qquad \text{then } \Phi_x^+ = \dfrac{dQ^3}{dx} = d_{i,j}^{(3)}\left(k^1, k^2\right) \end{cases}$$

ENO 4

1) $Q^0(x) = \Phi_{i,j}$

2) For $k^1 = \{i-1, i\}$ we compute :

a) $Q^1(x) = \dfrac{\Phi_{k^1+1,j} - \Phi_{k^1,j}}{\Delta x}(x - x_i)$.

$\dfrac{dQ^1}{dx} = \dfrac{\Phi_{k^1+1,j} - \Phi_{k^1,j}}{\Delta x} = d_{i,j}^{(1)}$

b) Compute the following three iterations :

First step

i)

$$\begin{cases} a^1 = \dfrac{\Phi_{k^1+1,j} - 2\Phi_{k^1,j} + \Phi_{k^1-1,j}}{2(\Delta x)^2} \\ b^1 = \dfrac{\Phi_{k^1+2,j} - 2\Phi_{k^1+1,j} + \Phi_{k^1,j}}{2(\Delta x)^2} \end{cases}$$

ii)

$$C^1 = \begin{cases} a^1 & \text{if } \left|a^1\right| \leq \left|b^1\right| \\ b^1 & \text{otherwise} \end{cases}$$

$$k^2 = \begin{cases} k^1 - 1 & \text{if } \left|a^1\right| \leq \left|b^1\right| \\ k^1 & \text{otherwise} \end{cases}$$

$$d_{i,j}^{(2)}\left(k^1\right) = d_{i,j}^{(1)} + C^1\left(2\left(i - k^1\right) - 1\right)\Delta x$$

Second step

i)

$$\begin{cases} a^2 = \dfrac{\Phi_{k^2+2,j} - 3\Phi_{k^2+1,j} + 3\Phi_{k^2,j} + \Phi_{k^2-1,j}}{6(\Delta x)^3} \\ b^2 = \dfrac{\Phi_{k^2+3,j} - 3\Phi_{k^2+2,j} + 3\Phi_{k^2+1,j} + \Phi_{k^2,j}}{6(\Delta x)^3} \end{cases}$$

ii)

$$C^2 = \begin{cases} a^2 & \text{if } \left|a^2\right| \leq \left|b^2\right| \\ b^2 & \text{otherwise} \end{cases}$$

$$k^3 = \begin{cases} k^2 - 1 & \text{if } \left|a^2\right| \leq \left|b^2\right| \\ k^2 & \text{otherwise} \end{cases}$$

$$d_{i,j}^{(3)}\left(k^1, k^2\right) = d_{i,j}^{(1)} + C^1\left(2\left(i - k^1\right) - 1\right)\Delta x + C^2\left(3\left(i - k^2\right)^2 - 6\left(i - k^2\right) + 2\right)(\Delta x)^2$$

Third step

i)

$$\begin{cases} a^3 = \dfrac{\Phi_{k^3+3,j} - 4\Phi_{k^3+2,j} + 6\Phi_{k^3+1,j} - 4\Phi_{k^3,j} - \Phi_{k^3-1,j}}{24(\Delta x)^4} \\ b^3 = \dfrac{\Phi_{k^3+4,j} - 4\Phi_{k^3+3,j} + 6\Phi_{k^3+2,j} - 4\Phi_{k^3+1,j} - \Phi_{k^3,j}}{24(\Delta x)^4} \end{cases}$$

ii)

$$C^3 = \begin{cases} a^3 & \text{if } \left|a^3\right| \leq \left|b^2\right| \\ b^3 & \text{otherwise} \end{cases}$$

$$k^4 = \begin{cases} k^3 - 1 & \text{if } \left|a^3\right| \leq \left|b^3\right| \\ k^3 & \text{otherwise} \end{cases}$$

iii)

$$Q^4(x) = Q^3(x) + C^3(x - x_{k^3})(x - x_{k^3+1})(x - x_{k^3+2})(x - x_{k^3+3})$$

c)

$$\frac{dQ^4}{dx} = \frac{dQ^3}{dx}(x_i) + C^3\left(4\left(i-k^3\right)^3 - 18\left(i-k^3\right)^2 + 22\left(i-k^3\right) - 6\right)(\Delta x)^3 = d_{i,j}^{(4)}\left(k^1, k^2, k^3\right)$$

$$d_{i,j}^{(4)}\left(k^1, k^2, k^3\right) = d_{i,j}^{(1)} + C^1\left(2\left(i-k^1\right) - 1\right)\Delta x + C^2\left(3\left(i-k^2\right)^2 - 6\left(i-k^2\right) + 2\right)(\Delta x)^2 + C^3\left(4\left(i-k^3\right)^3 - 18\left(i-k^3\right)^2 + 22\left(i-k^3\right) - 6\right)(\Delta x)^3$$

$$\begin{cases} \text{If } k^1 = i-1 \text{ then } \Phi_x^- = \dfrac{dQ^4}{dx} = d_{i,j}^{(4)}\left(k^1, k^2, k^3\right) \\ \text{If } k^1 = i \quad \text{then } \Phi_x^+ = \dfrac{dQ^4}{dx} = d_{i,j}^{(4)}\left(k^1, k^2, k^3\right). \end{cases}$$

High-order ENO schemes for Hamilton-Jacobi equations use a monotone flux as a building block and the ENO interpolation procedure to approximate the left and right derivatives at the cell center. For the barotropic Equations (2.38), we propose to adapt the fourth-order ENO scheme introduced and used in [41] by Osher and Shu for Hamilton-Jacobi equations. The advective form of the potential vorticity equation (4.24) is thus regarded as a Hamilton-Jacobi equation:

$$\frac{\partial \xi}{\partial t} + H(\xi_x, \xi_y) = 0, \tag{4.64}$$

where $H(\xi_x, \xi_y)$ represents the Hamiltonian of ξ:

$$H(\xi_x, \xi_y) = -\frac{\partial \psi}{\partial y}\frac{\partial \xi}{\partial x} + \frac{\partial \psi}{\partial x}\frac{\partial \xi}{\partial y}. \tag{4.65}$$

Both the conservative and advective forms were exploited in [28] where the central scheme for conservation laws is used.

4.7.3 Scheme construction

For mesh sizes $\Delta x, \Delta y, \Delta t$, the numerical approximation to the potential vorticity solution ξ of (4.64) is denoted $\xi_{i,j}^n$. We also use the standard notation

$$\xi_{x,i,j}^{\pm} = \pm \frac{(\xi_{i\pm1,j} - \xi_{i,j})}{\Delta x}, \quad \xi_{y,i,j}^{\pm} = \pm \frac{(\xi_{i,j\pm1} - \xi_{i,j})}{\Delta y}.$$

The numerical scheme for the equation of the potential vorticity in (4.64), in its Euler form, is

$$\frac{\xi_{i,j}^{n+1} - \xi_{i,j}^{n}}{\Delta t} = -H_{LLF}^{n}\left(\xi_{x,i,j}^{+}, \xi_{x,i,j}^{-}, \xi_{y,i,j}^{+}, \xi_{y,i,j}^{-}\right) \tag{4.66}$$

where H_{LLF}^n is the local Lax Friedrichs numerical Hamiltonian [41]:

$$H_{LLF}^{n}\left(\xi_x^+, \xi_x^-, \xi_y^+, \xi_y^-\right) = H\left(\frac{\xi_x^+ + \xi_x^-}{2}, \frac{\xi_y^+ + \xi_y^-}{2}\right) - \frac{1}{2}\alpha^x\left(\xi_x^+, \xi_x^-\right)\left(\xi_x^+ - \xi_x^-\right) - \frac{1}{2}\alpha^y\left(\xi_y^+, \xi_y^-\right)\left(\xi_y^+ - \xi_y^-\right)$$

and

$$\alpha^x = \max_{\substack{r \in I\left(\xi_x^-, \xi_x^+\right) \\ C \le q \le D}} \left|H_1\left(r, q\right)\right|, \qquad \alpha^y = \max_{\substack{q \in I\left(\xi_y^-, \xi_y^+\right) \\ A \le r \le B}} \left|H_2\left(r, q\right)\right|,$$

which is a Lipschitz continuous monotone flux consistent with H in PDE (4.64) [17]:

$$H_{LLF}^{n}\left(r, r, s, s\right) = H\left(r, s\right).$$

Here $H_i\left(r, q\right)$ is the partial derivative of H with respect to the i-th argument, or the Lipschitz constant of H with respect to the i-th argument. Monotonicity here means that H_{LLF}^n is nonincreasing in its first and third arguments and nondecreasing in the other two ($H_{LLF}^n\left(\downarrow, \uparrow, \downarrow, \uparrow\right)$).

Lemma 4.7.1 *H^{LLF} is monotone.*

Proof H^{LLF} in one dimension is defined by

$$H^{LLF}\left(u^+, u^-\right) = H\left(\frac{u^+ + u^-}{2}\right) - \frac{1}{2}\max_{u \in I\left(u^-, u^+\right)} \left|H'\left(u\right)\right|\left(u^+ - u^-\right).$$

(a) We assume $u_1^+ > u_2^+$ and want to prove $H^{LLF}\left(u_1^+, u^-\right) \le H^{LLF}\left(u_2^+, u^-\right)$. let $D = H^{LLF}\left(u_1^+, u^-\right) - H^{LLF}\left(u_2^+, u^-\right)$. This equals

$$H\left(\frac{u_1^+ + u^-}{2}\right) - H\left(\frac{u_2^+ + u^-}{2}\right) - \frac{1}{2}\max_{u \in I\left(u^-, u_1^+\right)} \left|H'\left(u\right)\right|\left(u_1^+ - u^-\right) + \frac{1}{2}\max_{u \in I\left(u^-, u_2^+\right)} \left|H'\left(u\right)\right|\left(u_2^+ - u^-\right).$$

Case 1: $u_1^+ > u_2^+ > u^-$. We have, for $u^- \le \frac{u_2^+ + u^-}{2} \le \xi \le \frac{u_1^+ + u^-}{2} \le u_1^+$,

$$\begin{aligned} D &= \frac{1}{2}\left[H'(\xi)\left(u_1^+ - u_2^+\right) - \max_{u^- \le u \le u_1^+}\left|H'(u)\right|\left(u_1^+ - u^-\right) + \max_{u^- \le u \le u_2^+}\left|H'(u)\right|\left(u_2^+ - u^-\right)\right] \\ &\le \frac{1}{2}\left[H'(\xi)\left(u_1^+ - u_2^+\right) - \max_{u^- \le u \le u_1^+}\left|H'(u)\right|\left(u_1^+ - u^-\right) + \max_{u^- \le u \le u_1^+}\left|H'(u)\right|\left(u_2^+ - u^-\right)\right] \\ &= \frac{1}{2}\left(u_1^+ - u_2^+\right)\left[H'(\xi) - \max_{u^- \le u \le u_1^+}\left|H'(u)\right|\right] \le 0; \end{aligned}$$

Case 2: $u^- > u_1^+ > u_2^+$, similar to case 1.

(b) We assume $u_1^- > u_2^-$

Case 1 $u^+ > u_1^- > u_2^-$, and for $u_2^- \le \xi \le u^+$ we have

$$\begin{aligned} D &= \frac{1}{2}\left[H'(\xi)\left(2u_1^- - u_2^- - u^+\right) + \max_{u_2^- \le u \le u^+}\left|H'(u)\right|\left(u^+ - u_2^-\right)\right] \\ &= \frac{1}{2}\left(u^+ - u_1^-\right)\left[\max_{u_2^- \le u \le u^+}\left|H'(u)\right| - H'(\xi)\right] + \frac{1}{2}\left(u_1^- - u_2^-\right)\left[\max_{u_2^- \le u \le u^+}\left|H'(u)\right| + H'(\xi)\right] \ge 0 \end{aligned}$$

Case 2 $u_1^- > u^+ > u_2^-$, and, since $H\left(u_1^-\right) \ge H\left(u^+\right)$ due to the fact that $H'(u) \ge 0$ in $\left[u^+, u_1^-\right]$, we have, for $u^+ \ge \xi \ge \frac{\left(u^+ + u_2^-\right)}{2} \ge u_2^-$,

$$\begin{aligned} D &= H\left(u_1^-\right) - H^{LLF}\left(u^+, u_2^-\right) \ge H\left(u^+\right) - H^{LLF}\left(u^+, u^-\right) \\ &= \frac{1}{2}\left[H'(\xi)\left(u^+ - u_2^-\right) + \max_{u_2^- \le u \le u^+}\left|H'(u)\right|\left(u^+ - u_2^-\right)\right] \\ &= \frac{1}{2}\left(u^+ - u_2^-\right)\left[H'(\xi) + \max_{u_2^- \le u \le u^+}\left|H'(u)\right|\right] \ge 0 \end{aligned}$$

We have proved $H^{LLF}(\cdot, \uparrow)$ and similarly for $H^{LLF}(\downarrow, \cdot)$. □

The scheme (4.66) with a monotone numerical Hamiltonian is called a monotone scheme. It is proven in [17] that monotone schemes have the following favorable properties:

- Monotone schemes are stable in the L1 norm;
- Monotone schemes are convergent to the viscosity solution of (4.64);

• The error between the numerical solution of a monotone scheme and the exact viscosity solution of (4.64), measured in the L1 norm, is at least half order $\bigcirc\left(\sqrt{\Delta x}\right)$.

We now begin the description of the fourth-order ENO scheme. The monotone flux described above play the role of building blocks. The ENO interpolation described in subsection 3-4-1 is used to compute fourth-order approximations to the left and right derivatives $\xi_x^{\pm}$ and $\xi_y^{\pm}$. The fourth order centered difference scheme is used to compute fourth-order approximations to the derivatives ψ_x and ψ_y. These values are then put into the monotone flux $H_{LLF}^n\left(\xi_x^+, \xi_x^-, \xi_y^+, \xi_y^-\right)$. Time accuracy is obtained by a class of TVD Runge-Kutta type time discretizations [16, 57, 58]. The algorithm can be summarized as follows:
(1) At any node (x_i, y_j), fix j to compute a derivative along the x-direction, by using the ENO interpolation procedure

$$\xi_x^{\pm} = \frac{d}{dx} P_4^{j\pm\frac{1}{2}}\ (x_i)\,.$$

(2) Similarly, at the node (x_i, y_j), fix i to compute along the y-direction, by using the ENO interpolation procedure

$$\xi_y^{\pm} = \frac{d}{dx} P_4^{j\pm\frac{1}{2}}\ (y_j)\,.$$

Then let

$$L_{i,j} = -\Delta t H_{LLF}^n\left(\xi_x^+, \xi_x^-, \xi_y^+, \xi_y^-\right),$$

(3) obtain ξ^{n+1} from ξ^n by the following forth-order Runge-Kutta method:

$$\begin{aligned} \xi_{i,j}^{(0)} &= \xi_{i,j}^n, \\ \xi_{i,j}^{(k)} &= \sum_{l=0}^{k-1} (\alpha_{k,l}\xi_{i,j}^{(l)} + \beta_{k,l} L_{i,j}^{(l)}), \quad k = 1, 2, 3, 4, \\ \xi_{i,j}^{(n+1)} &= \xi_{i,j}^{(4)}, \end{aligned} \tag{4.67}$$

where $\alpha_{k,l}$ and $\beta_{k,l}$ are given in Table 4.2.

Remark 4.7.2 *[57]*
we define the total variation of the numerical solution (U_i^n) *by*

$$TV\left(U_i^n\right) = \sum_i \left|U_{i+1}^n - U_i^n\right|.$$

$\alpha_{k,l}$				$\beta_{k,l}$			
1				$\frac{1}{2}$			
$\frac{1}{2}$	$\frac{1}{2}$			$-\frac{1}{4}$	$\frac{1}{2}$		
$\frac{1}{9}$	$\frac{2}{9}$	$\frac{2}{3}$		$-\frac{1}{9}$	$-\frac{1}{3}$	1	
0	$\frac{1}{3}$	$\frac{1}{3}$	$\frac{1}{3}$	0	$\frac{1}{6}$	0	$\frac{1}{6}$

Table 4.2: Coefficients of a TVD Runge-Kutta scheme for the ENO-4 scheme [41].

It is said the scheme is total variation diminishing (TVD) if :

$$TV\left(U_i^{n+1}\right) \leq TV\left(U_i^n\right).$$

It is said the scheme is total variation bounded (TVB) for $t \in [0,T]$ *if*

$$TV\left(U_i^n\right) \leq B$$

where B *depends only on* $TV\left(U_i^0\right)$ *and* $t = n\Delta t \in [0,T]$.

The method (4.67) can be proven total variation diminishing, under the CFL condition [57]:

$$\frac{\Delta t}{\min(\Delta x, \Delta y)} \leq C_4 \lambda_0 \tag{4.68}$$

where

$$\lambda_0 = \frac{1}{\max(u,v)} \text{ and } C_4 = \frac{2}{3}.$$

As remarked in [41], when implementing the ENO-4 interpolation described in subsection 4-6-1 we use undivided differences [41]:

$$\phi(i,j,0) = \xi_{i,j}, \tag{4.69}$$

for $k = 1,5$

$$\phi(i,j,k) = \phi(i+1,j,k-1) - \phi(i,j,k-1). \tag{4.70}$$

The computation of (4.70) can be easily vectorized. The ENO stencil-choosing process is as follows. For computing ξ_x^+, starting with $k_{\min}^1 = i$

$$\text{if } \left|\phi\left(k_{\min}^1 - 1, j, k\right)\right| < \left|\phi\left(k_{\min}^1, j, k\right)\right|,$$

then

$$k_{\min}^1 = k_{\min}^1 - 1,$$

for $k = 2, 3, 4$ where $k^1_{\min}$ is the leftmost point in the stencil for $P_4^{j+\frac{1}{2}}(x)$. This can also be vectorized. Finally,

$$(\xi_x)^+_{i,j} = \frac{1}{\Delta x}\sum_{k=1}^{4} C\left(k^1_{\min} - i, k\right).\phi\left(k^1_{\min}, j, k\right),$$

where

$$C(4,k) = \frac{1}{k!}\sum_{s=4}^{k+3}\prod_{l=4, l\neq s}^{k+3}(-l).$$

Note that the small matrix C, which is independent of ξ is computed only once, and then stored. The fourth-order essentially non-oscillatory scheme (ENO-4) for the barotropic system (2.50) is achieved by combining the discrete equation for potential vorticity in (4.67) with a fourth-order Poisson solver for the stream-function. We use a nine point stencil for the Poisson equation:

$$\begin{aligned}\Delta^n_{i,j}\psi^n = &\frac{-\psi^n_{i+2,j} + 16\psi^n_{i+1,j} - 30\psi^n_{i,j} - 16\psi^n_{i-1,j} - \psi^n_{i-2,j}}{12\Delta x^2} \\ &+\frac{-\psi^n_{i,j+2} + 16\psi^n_{i,j+1} - 30\psi^n_{i,j} - 16\psi^n_{i,j-1} - \psi^n_{i,j-2}}{12\Delta y^2} \\ &= \xi^n_{i,j} - y_j,\end{aligned} \tag{4.71}$$

$0 \leq i \leq N$ et $0 \leq j \leq M$. The method of resolution of Equation (4.71) is similar to the method used with the second-order Poisson equation in (4.59) using the same boundary conditions for the stream-function in (4.60) and the same boundary conditions for the potential vorticity in (4.63) . The validation of the ENO-4 scheme and Arakawa's method are given in the next chapter.

Chapter 5

Validation Tests

Here, the numerical solutions of the equatorial barotropic vorticity equation using the Arakawa Jacobian and the fourth-order essentially non-oscillatory scheme are validated through two typical known exact solutions, a smooth Rossby wavepacket and a discontinuous shear. Comparaisons are made with the exact solutions and between the two methods.

5.1 Rossby waves packets

We consider the Rossby wave packets used in [28]

$$\psi(x, y, t) = \cos(k_1 x - \omega t)\sin(k_2 y) \tag{5.1}$$

with k_1 is the zonal wavenumber, k_2 is the meridional wavenumber, and $\omega = \dfrac{-k_1}{k_1^2 + k_2^2}$ is the dispersion relation. These wave packets are defined on a periodic channel of zonal length $X = 40000\ km$ and meridional width $2Y = 10000\ km$ and they solve the nonlinear barotropic equations (2.38) exactly. It can be seen that these wave packets have vanishing meridional velocity v at the channel walls ($y = \pm Y$) provided k_2 is chosen to be a multiple of $\dfrac{\pi}{Y}$. The solutions described by (5.1) represent a traveling wave packet which propagates in the zonal direction at the speed $\dfrac{\omega}{k_1}$. We set $k_1 = 8\pi/X$ and $k_2 = \pi/Y$, which we may abbreviate by writing $k_1 \equiv 4$ and $k_2 \equiv 1$. We fix the initial magnitude of the wind such that

$$\max_{x,y} \sqrt{\left(u^2(x, y, 0) + v^2(x, y, 0)\right)} = 5m/s.$$

Grid	5 days	10 days	15 days	20 days	50 days	100 days
128×75	$2.47E-02$	$4.89E-02$	$7.32E-02$	$9.82E-02$	$2.41E-01$	$4.61E-01$
256×150	$6.34E-03$	$1.25E-02$	$1.87E-02$	$2.51E-02$	$6.25E-02$	$1.24E-01$
Order of accuracy	1.97	1.97	1.97	1.97	1.95	1.90

Table 5.1: L^1-norm relative error between the exact and the numerical potential vorticity using the Arakawa method.

Grid	5 days	10 days	15 days	20 days	50 days	100 days
128×75	$3.93E-07$	$6.97E-07$	$1.05E-06$	$1.42E-06$	$4.07E-06$	$1.08E-05$
256×150	$2.72E-08$	$4.67E-08$	$7.24E-08$	$9.86E-08$	$2.88E-07$	$7.76E-07$
Order of accuracy	3.87	3.91	3.87	3.86	3.83	3.81

Table 5.2: Same as Table 5.1 but with the ENO-4 scheme.

and we run the barotropic code described in the previous chapter forward in time. A second and a fourth order Runge-Kutta method is used, where Euler's method is used to make the initial prediction at each time step. this is an explicit method, where we use information at time step n to calculate time step $n+1$. (The second and fourth order Runge-Kutta methods correspond to a trunction after two and four terms respectiveley of the Taylor series expansion of the time derivative.)
A CFL condition with Courant number 0.8 is used to calculate the time step Δt from the given grid spacing Δx and Δy, and velocities (u, v). We choose $\Delta t = 0.8 \times (\min(\Delta x, \Delta y) / \max(u, v))$ in Arakawa method and $\Delta t = 0.8 \times C_4 \times (\min(\Delta x, \Delta y) / \max(u, v))$ in ENO-4 scheme. Notice that the Rossby wave packet in (5.1) satisfies the Dirichlet boundary condition in (4.63).

We report in table 5.1 the L^1-norm relative error, with respect to the potential vorticity ξ, between the exact and numerical solutions for two different grids, 128×75 and 256×150 at six consecutive times, $5, 10, 15, 20, 50$ and 100 days, using the Arakawa Jacobian method.

The same relative errors computed using the fourth-order essentially non-oscillatory scheme are shown in table 5.2. An examination of the rate of convergence, found by taking the ratio of errors of the two grids at a given time, suggests that both methods are able to capture the large scale dispersive wave with an overall second order and fourth-order accuracy for Arakawa Jacobian method and fourth-order essentially non-

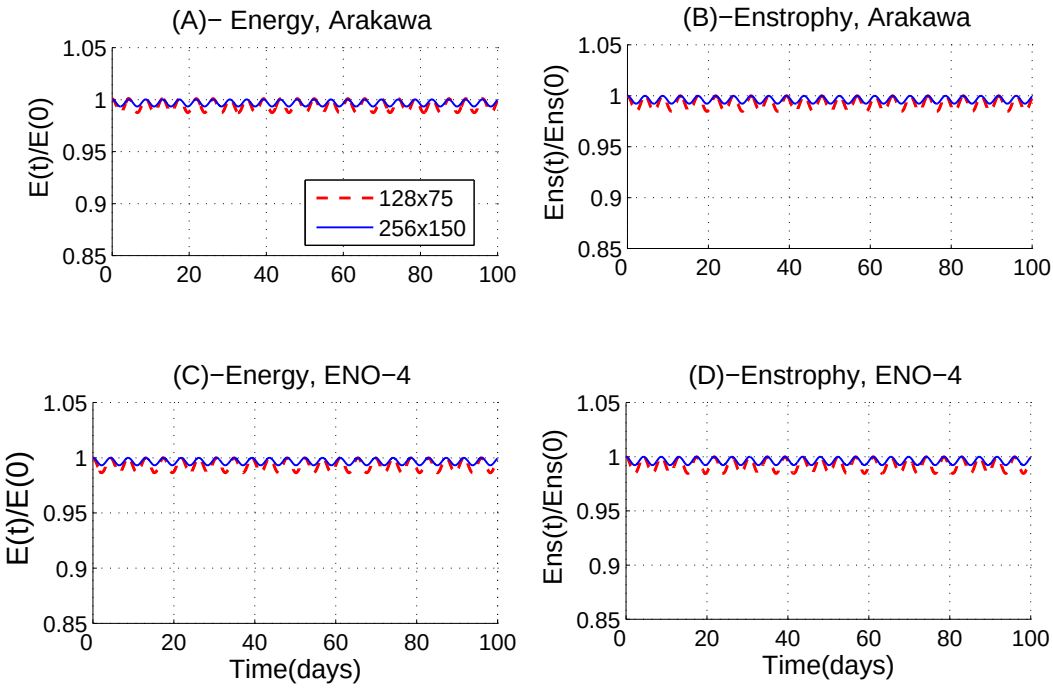

Figure 5.1: (A) and (B): Energy and Enstrophy time plots using 128x75 and 256x150 grid points using Arakawa method. (C) and (D) same as in (A) and (B) but with ENO-4 scheme.

oscillatory scheme, respectively.

Energy-time series plots in Figure 5.1 show that energy remains relatively constant in time for the Arakawa method and the fourth-order essentially non-oscillatory scheme, regardless of the number of grid points. In Figure 5.2, a zonal slice of the vorticity $\overline{\omega} = \xi - y$ at $y \approx 1600$ km at $t = 20$ days are shown for the grids 128×75 and 256×150 using the Arakawa Jacobian method and fourth-order essentially non-oscillatory scheme and is compared with the exact solution. From this plots, it is apparent that the phase speed obtained by Arakawa method and ENO-4 scheme is nearly identical of the phase speed of Rossby wave packets, unlike the central scheme that suffered from apparent phase lag [28].

Though, at coarse resolution, the Arakawa solution seems to be moving slightly slower that the exact wave solution while the ENO-4 method is faster. Recall that the wave is moving westward, i.e, to the left. Note that with $k_1 = 4$, there are only 32 and 64 grid points per wavelength, respectively for the two grids in figure 5.2

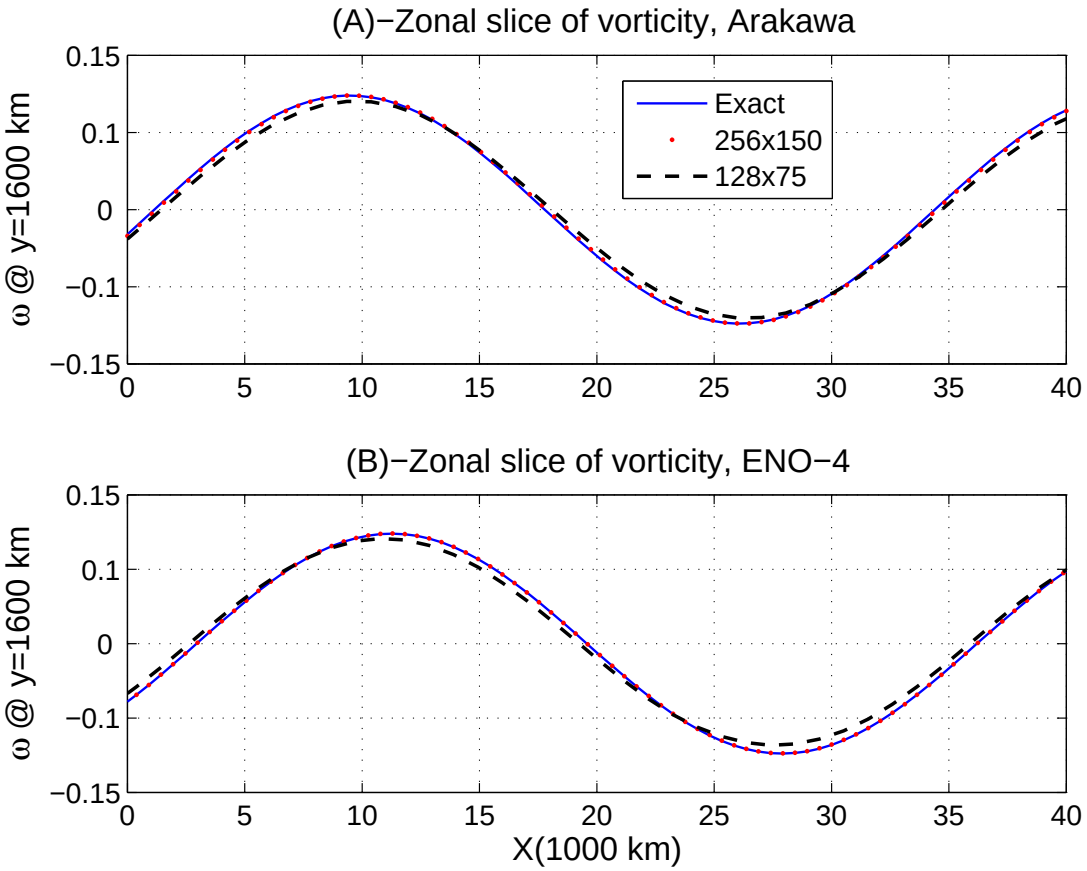

Figure 5.2: One wavelength zonal slice plot at t=20 days of the vorticity $\overline{\omega}$ at $y \approx 1600$ km. (A) -Arakawa method,(B)-ENO-4 scheme.

In figure 5.3, contour plots of the vorticity $\overline{\omega}$ are shown for the different grids and the exact solution at $t = 20$ days. Velocity profiles are also superimposed. It appears that the structure and velocity field of the wave packet is nearly identical in all three cases.

The y-plots of the L^1-norm errors in x-direction for the two grids at 5 days for both methods in figure 5.4 show that we have no error accumulation at the walls. This is most likely due to the fact that at each time step, the Arakawa Jacobian and the Hamiltonian of $\overline{\xi}$ vanish at the boundary $y = \pm Y$.

5.2 A discontinuous shear flow

As an extreme test case, we consider a discontinuous shear flow given by

$$\mathrm{v} = (\mathrm{u}(y), 0) \tag{5.2}$$

where

$$\mathrm{u}(y) = \begin{cases} 1 & y > 0 \\ -1 & y < 0. \end{cases} \tag{5.3}$$

From the last equations in (2.50) we have:

$$u = \mathrm{u}(y) = -\frac{\partial \psi}{\partial y} \text{ and } v = 0 = \frac{\partial \psi}{\partial x},$$

which gives

$$\psi(y) = \begin{cases} -y & y > 0 \\ y & y < 0 \end{cases} \tag{5.4}$$

and

$$\xi(y) = \Delta\psi + y = -2\delta_0 + y, \tag{5.5}$$

where δ_0 is the Dirac delta function at $y = 0$. Before we proceed to validation runs, particular care needs to be taken with regards to the solutions given in (5.4) and (5.5). We note that the discontinous shear flow is a solution to the barotropic equations in the weak sense, i.e, in the sense of distributions. Thus, the Dirac delta function is replaced by a regularization sequence (ρ_ε), which converges towards δ_0 when $\varepsilon \to 0$. Let

$$\rho_\varepsilon(y) = \begin{cases} 0 & |y| > \varepsilon \\ \frac{1}{\varepsilon^2} y + \frac{1}{\varepsilon} & -\varepsilon \le y \le 0 \\ -\frac{1}{\varepsilon^2} y + \frac{1}{\varepsilon} & 0 \le y \le \varepsilon, \end{cases} \tag{5.6}$$

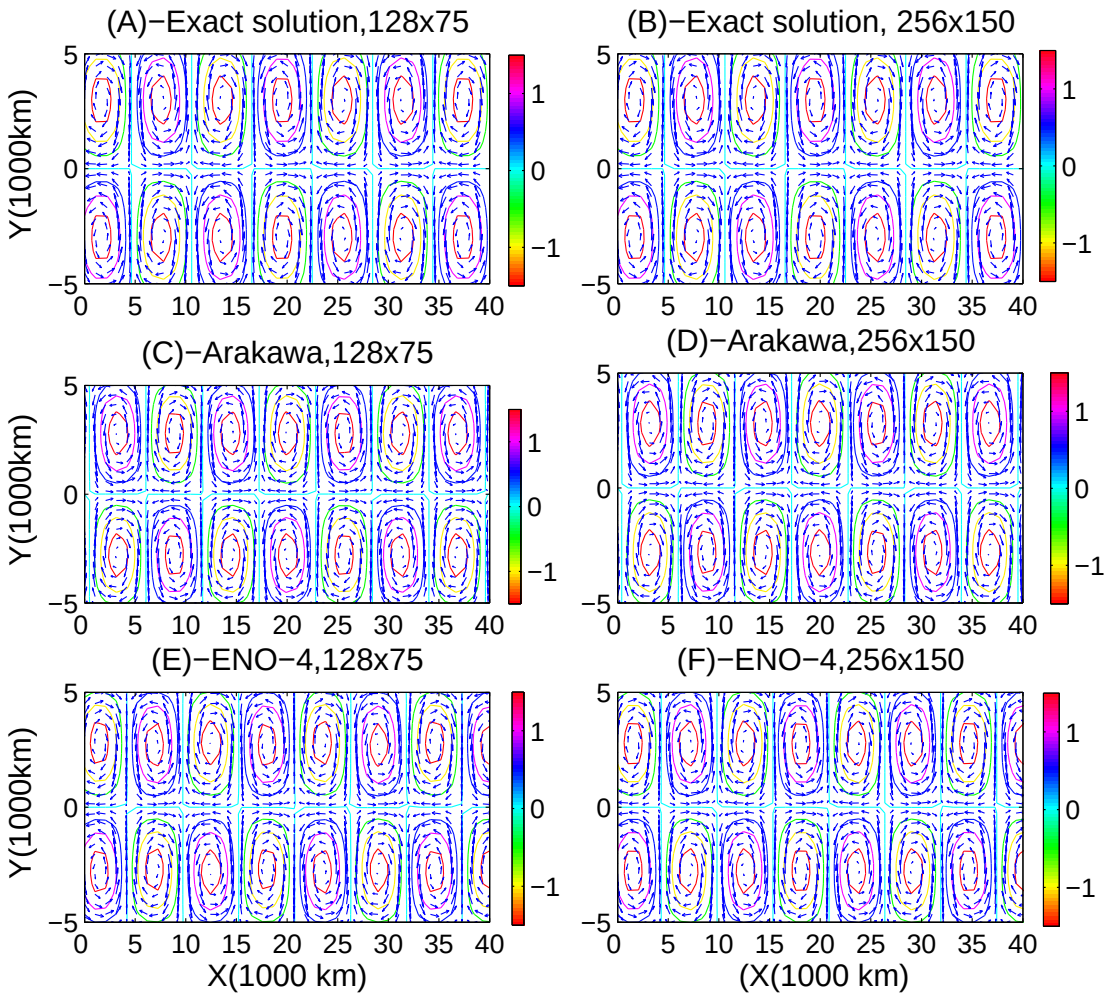

Figure 5.3: 2D structure of Rossby wave packet with $k_1 \equiv 4$ and $k_2 \equiv 1$. at time $t = 20$ days. Contours of the vorticity and velocity profile (arrows) for (C) and (D), using Arakawa method,(A) and (B) exact solution, and (E) and (F) ENO-4 scheme.

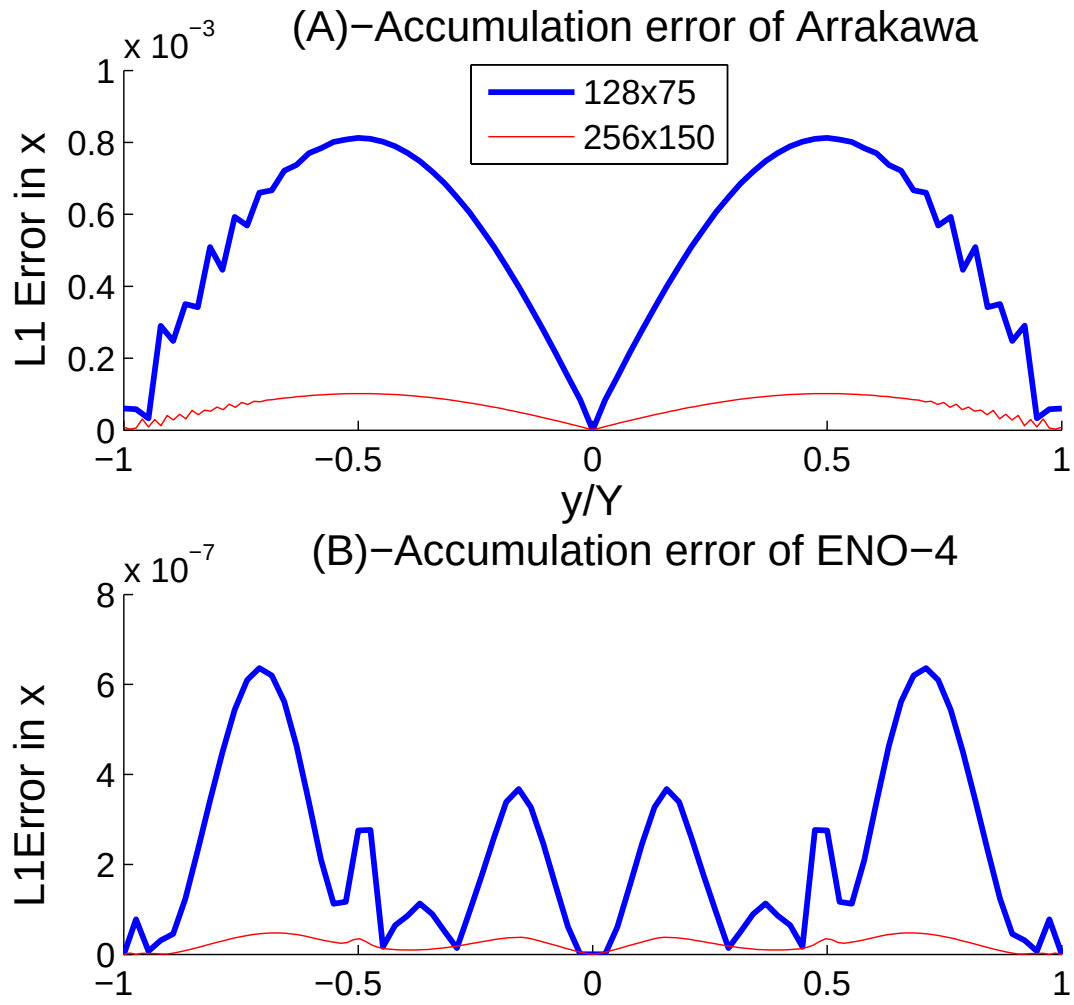

Figure 5.4: (A): L^1-norm error in x-direction versus y at time $t = 5$ days for Arakawa method. (B): same as in (A) but with ENO-4 scheme.

Grid	L_1 Error (at 20 days)	order of accuracy
64×38	$6.41E-04$	1.88
128×75	$1.75E-04$	2.00
256×150	$4.35E-05$	

Table 5.3: L^1-norm relative error between the exact and the numerical streamfunction using the Arakawa method in the case of the discontinuous shear.

	Whole domain		Smooth regions	
Grid	L_1 Error	order of accuracy	L_1 Error	order of accuracy
64×38	$1.31E-03$	2.62	$8.12E-04$	3.22
128×75	$2.15E-04$	2.93	$8.77E-05$	3.26
256×150	$2.83E-05$		$9.23E-06$	

Table 5.4: Same as Table 5.3 but with the ENO-4 scheme. L_1 error on the whole domain and its restriction to the smooth regions $|y| > 8\Delta y$.

where ε is a small positive number. In our numerical solution, we take $\varepsilon = \Delta y$ for the second-order method that couples the Arakawa Jacobian and the second order Poisson solver, and $\varepsilon = 8\Delta y$ for the fourth-order method (ENO-4). Where Δy is the grid spacing in the North-South direction. These are the smallest ε values that work for the two methods, respectively. Non-homogeneous Neumann and homogeneous Dirichlet boundary conditions are used at the wall for the stream-function and the potential vorticity, respectively:

$$\frac{\partial \psi}{\partial y}(Y) = -1, \quad \frac{\partial \psi}{\partial y}(-Y) = 1 \tag{5.7}$$

$$\overline{\omega} = \xi - y = 0 \quad \text{at } y = \pm Y. \tag{5.8}$$

We report in table 5.3 the L^1-norm relative error, with respect to the streamfunction ψ, between the exact and numerical solutions for three different grids, 64×38, 128×75 and 256×150 at time 20 days, using the Arakawa Jacobian method for the discontinuous shear flow. The same relative errors computed using the fourth-order essentially non-oscillatory scheme are shown in table 5.4. Note that in Table 5.4, both the L_1 error on the whole domain and its restriction to the smooth region away from $y = 0$, and the associated order of accuracy, are reported. In Figure 5.5, the smoothed vorticity and streamfunction of the "exact" and numerical solutions are shown for the grid 128×75

using the Arakawa Jacobian method. Figure 5.6 is the same as Figure 5.5 but for the ENO-4 scheme.

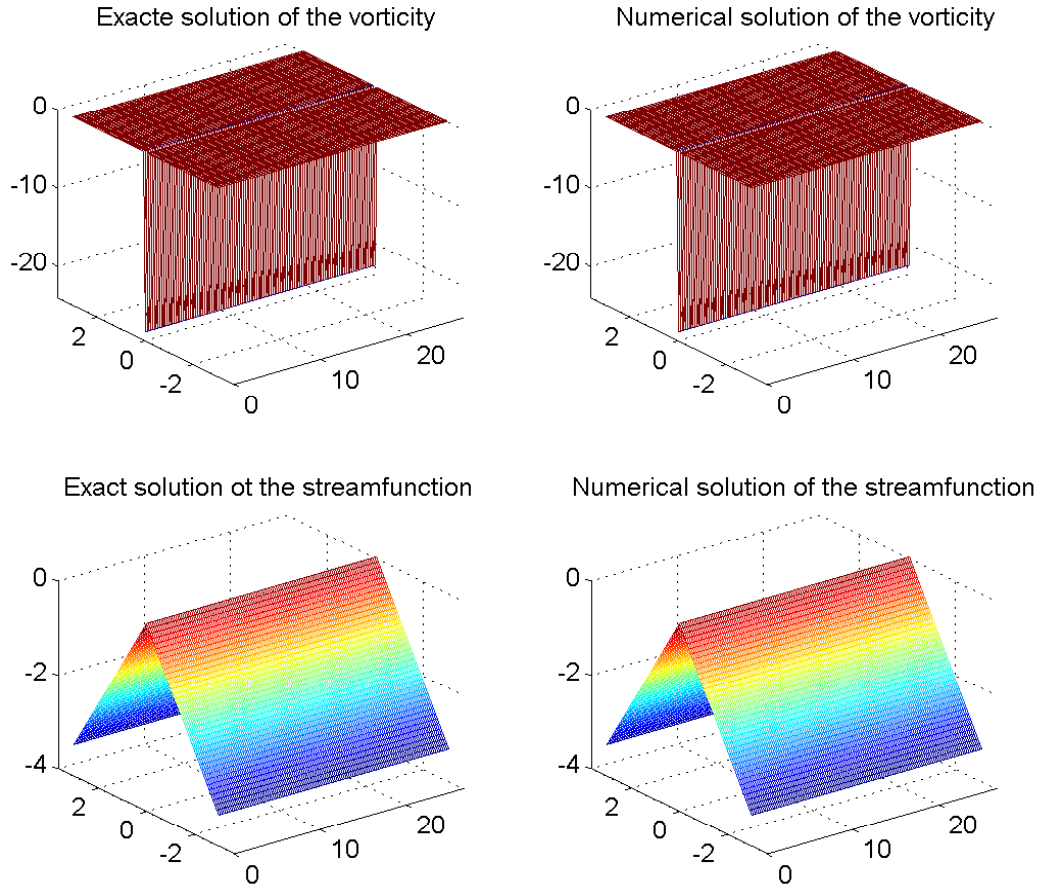

Figure 5.5: Three dimensional plots of the exact and numerical solutions, 128×75 grid points using Arakawa method in the case of the discontinuous Shear.

We note that in this case of the discontinuous shear (exact) solution, none of the schemes is expected to return its theoretical order of accuracy. However, as we can see from Tables 5.4 and 5.5 and Figures 5.5 and 5.6, both the Arakawa Jacobian and the ENO-4 methods reproduce the discontinuous shear solution with great accuracy. However, it is interesting to note here that while Arakawa's method recovers the formal second order convergence (as shown on the last column of Table 5.4), the actual order of accuracy is less than 3 i.e way below the theoretical fourth order convergence rate,

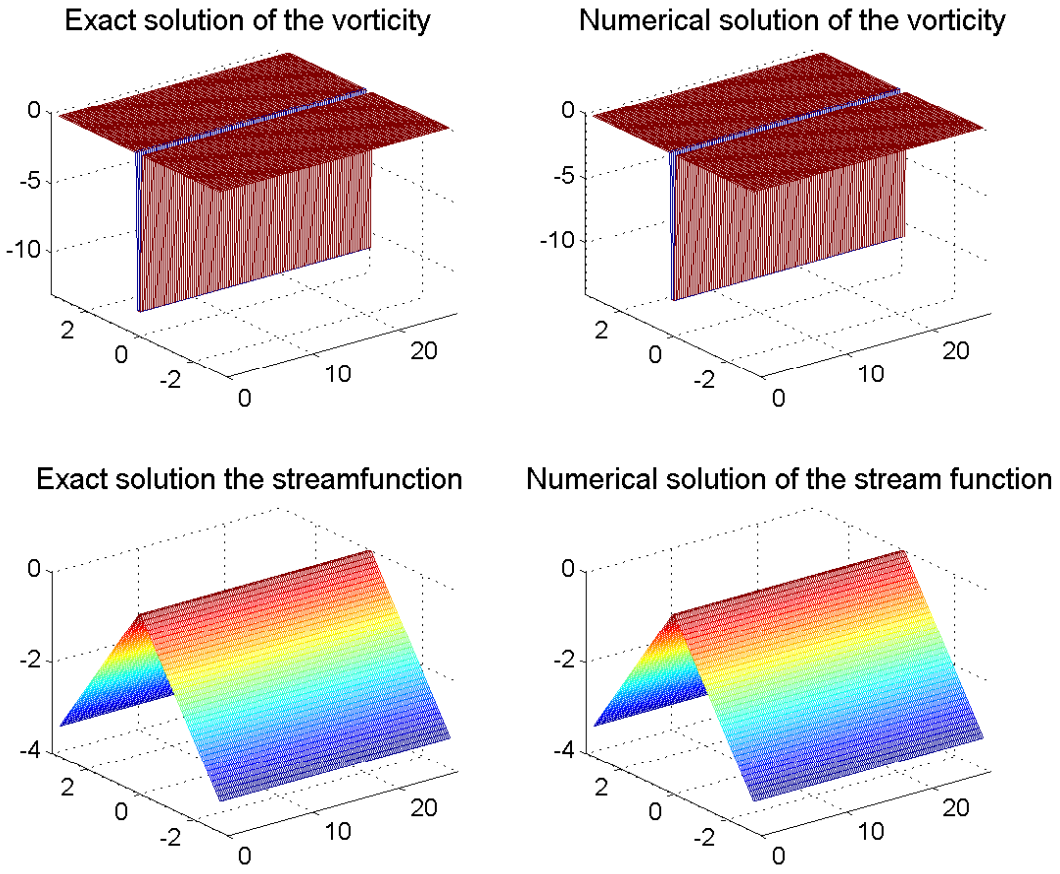

Figure 5.6: Same as in figure 5.5 but with ENO-4 scheme.

unlike the smooth case in Table 5.3. This can be explained in part by the fact that the Arakawa method uses a smoother $\varepsilon = \Delta y$ while ENO-4 necessitates $\varepsilon = 8\Delta y$. But for all practical purposes, both methods seem to yield adequate results. When the error calculation for the ENO scheme is restricted to the region of the domain where the solution is smooth, we recover an order of accuracy larger than 3 but still smaller than 4. Due to the ellipticity of the Poisson equation, the numerical "inaccuracy" which is otherwise concentrated near the singularity propagates (with an infinite speed) to the rest of the domain. This explains in part why even within the smooth regions of the domain fourth order accuracy is not achieved as shown in Table 5.4.

Chapter 6

Barotropic instability

6.1 Introduction

The common approach for analyzing the instability of linear geophysical flow requires examining the long term time dependence of the solution. In particular, for a stream function $\psi(x, y, t)$ of a linear system, the normal mode solution can be written as

$$\psi(x, y, t) = \hat{\psi}(y) \exp i(kx - \omega t) = \hat{\psi}(y) \exp[ik(x - ct)],$$

where $c = \dfrac{\omega}{k}$ is the phase speed of propagation. We can assess the stability of the solution based on the generalized dispersion relation $\omega = \omega(k)$. If we consider a complex phase speed and break up c into real and imaginary components, $c = c_r + ic_i$, then we can deduce the time dependent nature of the solution based on the magnitude and sign of c_i. The three possibilities are

$c_i = 0$ periodic solution

$c_i < 0$ stable solution. $\psi \longrightarrow 0$ as $t \longrightarrow \infty$

$c_i > 0$ unstable solution. $\psi \longrightarrow \infty$ as $t \longrightarrow \infty$.

Let us use the above analysis for some basic barotropic geophysical systems. In the following sections, we provide analytic solutions and necessary conditions for the barotropic instability for a prescribed shear flow in the vicinity of the equator, following the standard textbook linear analysis found for example in [5].

6.2 Waves in a shear flow

To begin, we rewrite the system in (2.38) in terms of the velocity components $\mathbf{v} = (u, v)$:

$$\begin{cases} \dfrac{\partial u}{\partial t} + u\dfrac{\partial u}{\partial x} + v\dfrac{\partial u}{\partial y} - \beta y v = -\dfrac{\partial p}{\partial x} & (6.1.1) \\ \dfrac{\partial v}{\partial t} + u\dfrac{\partial v}{\partial x} + v\dfrac{\partial v}{\partial y} + \beta y u = -\dfrac{\partial p}{\partial y} & (6.1.2) \\ \dfrac{\partial u}{\partial x} + \dfrac{\partial v}{\partial y} = 0 & (6.1.3) \end{cases} \tag{6.1}$$

For the basic state, we choose a zonal current with an arbitrary meridional profile: $u = \overline{u}(y)$, $v = 0$. This is an exact solution of (6.1) as long as the associated pressure profile, $p = \overline{p}$, satisfies the geostrophic balance

$$(\beta y)\,\overline{u}(y) = -\frac{\partial \overline{p}}{\partial y}. \tag{6.2}$$

6.3 The perturbation equations

We now add a small perturbation, which is meant to represent an arbitrary wave of weak amplitude. We write

$$\begin{cases} u = \overline{u}(y) + u'(x, y, t) & (6.3.1) \\ v = v'(x, y, t) & (6.3.2) \\ p = \overline{p}(y) + p'(x, y, t), & (6.3.3) \end{cases} \tag{6.3}$$

where the perturbation (u',v', p') is assumed to be relatively smaller than the basic flow formed by $(\bar{u}(y), 0, \bar{p}(y))$.

Substitution in Equations (6.3.1) , (6.3.2) and (6.3.3) and subsequent linearization, taking advantage of the smallness of the perturbation and using (6.2) yield:

$$\begin{cases} \dfrac{\partial u'}{\partial t} + \overline{u}\dfrac{\partial u'}{\partial x} + v'\dfrac{\partial \overline{u}}{\partial y} - \beta y v' = -\dfrac{\partial p'}{\partial x} & (6.4.1) \\ \dfrac{\partial v'}{\partial t} + \overline{u}\dfrac{\partial v'}{\partial x} + \beta y u' = -\dfrac{\partial p'}{\partial y} & (6.4.2) \\ \dfrac{\partial u'}{\partial x} + \dfrac{\partial v'}{\partial y} = 0. & (6.4.3) \end{cases} \tag{6.4}$$

The last equation admits a perturbation streamfunction ψ' such that

$$u' = -\frac{\partial \psi'}{\partial y}\ ,\ v' = \frac{\partial \psi'}{\partial x}. \tag{6.5}$$

A cross-differentiation of the momentum equations (6.4.1) and (6.4.2) and the elimination of the velocity components lead to a single equation for the perturbation streamfunction:

$$\left(\frac{\partial}{\partial t}+\overline{u}\frac{\partial}{\partial x}\right)(\Delta\psi')+\left(\beta-\frac{d^2\overline{u}}{dy^2}\right)\frac{\partial\psi'}{\partial x}=0. \tag{6.6}$$

The domain of the flow is periodic in the x-direction and bounded by rigid walls at $y=\pm Y$. The boundary condition at $y=\pm Y$ is $\dfrac{\partial\psi'}{\partial x}=0.$, i.e, no flow. This equation has coefficients that depend on $\overline{u}$ and, therefore, on the meridional coordinate y. We thus seek wave solutions on the form:

$$\psi'(x,y,t)=\varphi(y)\exp ik(x-ct), \tag{6.7}$$

where k is real and c and $\varphi(y)$ are complex. Substitution provides the following second-order ordinary differential equation for the amplitude $\varphi(y)$:

$$\frac{d^2\varphi}{dy^2}-k^2\varphi+\left(\frac{\beta-\dfrac{d^2\overline{u}}{dy^2}}{\overline{u}-c}\right)\varphi=0. \tag{6.8}$$

We note here that (6.8), which is known as the Raleigh equation, is identical to what is found in [5] for the midlatitude case ($f_0\neq 0$). The second-order, homogeneous problem in (6.8) is an eigenvalue problem where c is the eigenvalue and φ is the associated eigenfunction. In general, c can be complex. Let us thus assume

$$c=c_r+ic_i, \tag{6.9}$$

where the real part c_r represents the phase speed of the wave perturbation while the imaginary part c_i represents its exponential growth.

If $c_i\neq 0$, then the streamfunction ψ' will have a factor of the form $\exp(kc_it)$. If $c_i>0$, the wave will grow in time, and the background flow is said to be unstable. If $c_i<0$ the wave will be damped and the background is stable. However, complex eigenvalues come in pairs. Therefore, we have an instability whenever $c_i\neq 0$.

6.4 The necessary condition for occurrence of unstable waves

In this section we give the necessary condition for instability to occur. We multiply equation (6.8) by the complex conjugate of the stream function amplitude, $\varphi^\star$ and then

integrate across the domain, we obtain:

$$\int_{-Y}^{Y}\left(\left|\frac{d\varphi}{dy}\right|^2+k^2\left|\varphi\right|^2\right)dy-\int_{-Y}^{Y}\left(\frac{\beta-\frac{d^2\overline{u}}{dy^2}}{\overline{u}-c}\right)\left|\varphi\right|^2dy=0, \tag{6.10}$$

Integration by parts has been used for the first term with the no slip condition $\varphi(-Y)=\varphi(Y)=0$. The first term in equation (6.10) is always real but the second term can be either real or complex based on $c=c_r+ic_i$. if there is a complex component of the phase speed, then we know the basic flow is unstable. The imaginary portion of equation (6.10) gives the equation

$$c_i\int_{-Y}^{Y}\left(\beta-\frac{d^2\overline{u}}{dy^2}\right)\frac{\left|\varphi\right|^2}{\left|\overline{u}-c\right|^2}dy=0 \tag{6.11}$$

There are two possibilities of equation (6.11) being equal to 0. The first is that the basic flow admits no growing disturbance and is stable with $c_i=0$. The other possibility is that the basic flow is unstable with

$$\int_{-Y}^{Y}\left(\beta-\frac{d^2\overline{u}}{dy^2}\right)\frac{\left|\varphi\right|^2}{\left|\overline{u}-c\right|^2}dy=0. \tag{6.12}$$

The only way this integral can equal zero is if the quantity

$$\beta-\frac{d^2\overline{u}}{dy^2}=\frac{d}{dy}\left(\beta y-\frac{d\overline{u}}{dy}\right) \tag{6.13}$$

change sign somewhere inside the domain. We conclude that a necessary condition for instability is that expression (6.13) vanish somewhere inside the domain. Conversely, a sufficient condition for stability is that the same expression (6.13) does not vanish anywhere within the domain. Physically, the total vorticity of the basic flow $\beta y-\frac{d\overline{u}}{dy}$ must reach an extremum within the domain to cause instabilities. This result was first derived by Kuo (1949)[30].

This first criterion can be strengthened by considering next the real portion of equation (6.10):

$$\int_{-Y}^{Y}\left(\overline{u}-c_r\right)\left(\beta-\frac{d^2\overline{u}}{dy^2}\right)\frac{\left|\varphi\right|^2}{\left|\overline{u}-c\right|^2}dy=\int_{-Y}^{Y}\left(\left|\frac{d\varphi}{dy}\right|^2+k^2\left|\varphi\right|^2\right)dy. \tag{6.14}$$

If $c_i \neq 0$, the integral in (6.12) vanishes. Multiplying it by $(c_r - \overline{u}_0)$, where $\overline{u}_0$ is any real constant, adding the result to (6.14), and noting that the righ-hand side of (6.14) is always positive for $c_i \neq 0$, we obtain:

$$\int_{-Y}^{Y} (\overline{u} - \overline{u}_0) \left(\beta - \frac{d^2\overline{u}}{dy^2} \right) \frac{|\varphi|^2}{|\overline{u} - c|^2} dy > 0. \tag{6.15}$$

This inequality gives,

$$(\overline{u} - \overline{u}_0) \left(\beta - \frac{d^2\overline{u}}{dy^2} \right) > 0. \tag{6.16}$$

in at least some finite portion of the domain.
Hence, the following two necessary conditions for such an instability to occur [5, 48, 59]:

$\beta - \dfrac{d^2\overline{u}}{dy^2}$ changes sign some where in the domaine (6.17)

and for an constant $\overline{u}_0$

$(\overline{u} - \overline{u}_0) \left(\beta - \dfrac{d^2\overline{u}}{dy^2} \right)$ is positive some where in the domaine. (6.18)

6.5 Bounds on wave speeds and growth rates

Here we determine lower and upper bounds of the growth rate and the phase speed of the perturbations. For simplicity, we will restrict our study to the f-plane ($\beta = 0$) in which case the derivation is due to Howard (1964) [22]. Afterwards we will cite, without demonstration, the result for the beta plane. We start by the change of variable:

$$\varphi = (\overline{u} - c)\, a \tag{6.19}$$

which transforms equation (6.8) into

$$\begin{cases} \dfrac{d}{dy} \left((\overline{u} - c)^2 \dfrac{da}{dy} \right) - k^2 (\overline{u} - c)^2 a = 0 \\ a(-Y) = a(Y) = 0 \end{cases} \tag{6.20}$$

We consider the case of an unstable wave. In this case, c has a non-zero imaginary part, and a is non-zero and complexe. Multiplying by the complex conjugate $a^\star$ and integrating across the domain, we obtain

$$-\int_{-Y}^{Y}\left|\frac{da}{dy}\right|^2(\overline{u}-c)^2\,dy-\int_{-Y}^{Y}k^2\,(\overline{u}-c)^2\,|a|^2\,dy=0 \tag{6.21}$$

or

$$\int_{-Y}^{Y}(\overline{u}-c)^2\,P dy=0 \tag{6.22}$$

where $P=k^2\,|a|^2+\left|\frac{da}{dy}\right|^2$

The real and imaginary parts of equation (6.22) are:

Real part:

$$\int_{-Y}^{Y}\left[(\overline{u}-c_r)^2-c_i^2\right]P dy=0 \tag{6.23}$$

Imaginary part:

$$\int_{-Y}^{Y}(\overline{u}-c_r)\,P dy=0 \tag{6.24}$$

We conclude from (6.24) that $(\overline{u}-c_r)$ must vanish somewhere in the domain, impliying that the phase speed c_r lies between the minimum and maximum values of $\bar{u}(y)$:

$$\overline{u}_{\min}\ <c_r<\overline{u}_{\max} \tag{6.25}$$

Using this following relation:

$$-2c_r\int_{-Y}^{Y}\overline{u}P dy=-2c_r^2\int_{-Y}^{Y}P dy$$

and the equations (6.23) and (6.24), we show that:

$$\int_{-Y}^{Y}\left[\overline{u}^2-\left(c_r^2+c_i^2\right)\right]P dy=0 \tag{6.26}$$

Armed with bounds for the real part of c we now seek bounds for its imaginary part. We introduce the obvious inequality

$$\int_{-Y}^{Y} (\overline{u} - \overline{u}_{\min}\ )\,(\overline{u}_{\max} - \overline{u}\ )\,P dy \geq 0 \tag{6.27}$$

and then expand the expression, replace all linear terms in $\overline{u}$ using (6.24), and replace the quadratic term using (6.26) to arrive at

$$\left[\left(c_r - \frac{\overline{u}_{\min}\ + \overline{u}_{\max}}{2}\right)^2 + c_i^2 - \left(\frac{\overline{u}_{\max}\ - \overline{u}_{\min}}{2}\right)^2\right] \int_{-Y}^{Y} P dy \leq 0 \tag{6.28}$$

Because the integral of P can only be positive, the preceding bracketed quantity must be negative:

$$\left(c_r - \frac{\overline{u}_{\min}\ + \overline{u}_{\max}}{2}\right)^2 + c_i^2 \leq \left(\frac{\overline{u}_{\max}\ - \overline{u}_{\min}}{2}\right)^2 \tag{6.29}$$

This inequality implies that, in the complex plane, the number $c_r + ic_i$ must lie within the circle centred at $\left(\frac{\overline{u}_{\min}\ + \overline{u}_{\max}}{2}, 0\right)$ and of radius $\left(\frac{\overline{u}_{\max}\ - \overline{u}_{\min}}{2}\right)$. This result is called Howard's semicircle theorem. It readily evident from inequality (6.29) that c_i is bounded above by

$$c_i \leq \frac{\overline{u}_{\max}\ - \overline{u}_{\min}}{2}. \tag{6.30}$$

The perturbation's growth kc_i is thus likewise bounded above.

Pedlosky [42] extended this theorem to the β-plane case and showed that the phase speed, c_r, and the growth rate, c_i, of the perturbation satisfy:

$$\overline{u}_{\min} - \frac{\beta L^2}{2\left(\pi^2 + k^2 L^2\right)} < c_r < \overline{u}_{\max} \tag{6.31}$$

$$\left(c_r - \frac{\overline{u}_{\min} + \overline{u}_{\max}}{2}\right)^2 + c_i^2 \leq \left(\frac{\overline{u}_{\max} - \overline{u}_{\min}}{2}\right)^2 + \frac{\beta L^2\left(\overline{u}_{\max} - \overline{u}_{\min}\right)}{2\left(\pi^2 + k^2 L^2\right)}, \tag{6.32}$$

where $L = 2Y$ is the domain's meridional width and k the zonal wavenumber.

6.6 Broken line velocity profiles

The velocity field is represented by a profile in which $\bar{u}(y)$ is either piece-wise linear in y or constant. For zero β this leads to an equation for which the pv gradient is everywhere zero. The equation in (6.8) reduces to

$$\frac{d^2\varphi}{dy^2} - k^2\varphi = 0. \tag{6.33}$$

and all the dynamics of the instability is contained in the correct matching conditions at the points where either the velocity or the shear is discontinuous. It is therefore vitally important to get those conditions correctly. To do so we return to the original equation (6.8)

$$\frac{d^2\varphi}{dy^2} - k^2\varphi + \left(\frac{\beta - \frac{d^2\overline{u}}{dy^2}}{\overline{u} - c}\right)\varphi = 0. \tag{6.34}$$

Imagine a velocity profile which is continuous but which in the neighborhood of a point y_0 will become discontinuous. What conditions does (6.34) place on the solution φ in the neighborhood of that point? We rewrite (6.34) as,

$$\frac{\partial}{\partial y}\left((\overline{u} - c)\frac{d\varphi}{dy} - \frac{d\overline{u}}{dy}\varphi\right) - k^2(\overline{u} - c)\varphi + \beta_0\varphi = 0. \tag{6.35}$$

Now consider the integral of (6.35) across a small region containing the point y_0. If we integrate (6.35) on a infinitly thin layer (i.e from $y_0 - \epsilon$ to $y_0 + \epsilon$ with $\epsilon \underset{>}{\longrightarrow} 0$ and y_0 is the point of discontinuity), we obtain

$$\lim_{\epsilon\to 0}\int_{y_0-\epsilon}^{y_0+\epsilon}\left(k^2(\overline{u} - c)\varphi - \beta_0\varphi\right)dy = \left[(\overline{u} - c)\frac{d\varphi}{dy} - \frac{d\overline{u}}{dy}\varphi\right]_{y_0} \tag{6.36}$$

In (6.36) the square brackets represent the jump in the indicated variable from $y = y_0+\epsilon$ to $y = y_0 - \epsilon$ when $\epsilon \longrightarrow 0$. The integral on the left hand side in (6.36) go to zero as $\epsilon \longrightarrow 0$ due to the continuity of φ and $\overline{u}$ is bounded:

$$\lim_{\epsilon\to 0}\int_{y_0-\epsilon}^{y_0+\epsilon}\left(k^2(\overline{u} - c)\varphi - \beta_0\varphi\right)dy = 0 \tag{6.37}$$

Hence, the first condition is

$$\left[(\overline{u} - c)\frac{d\varphi}{dy} - \frac{d\overline{u}}{dy}\varphi\right]_{y_0} = 0. \tag{6.38}$$

A second condition is obetained by the following equation:

$$\frac{\partial}{\partial y}\left(\frac{\varphi}{\overline{u} - c}\right) = \frac{Y_1(y)}{(\overline{u} - c)^2} \tag{6.39}$$

where $y \mapsto Y_1(y) = (\overline{u} - c)\frac{d\varphi}{dy} - \frac{d\overline{u}}{dy}\varphi$ is a continuous function at y_0. If we integrate (6.39) on a infinitily thin layer, we obtain

$$\lim_{\epsilon \to 0} \int_{y_0-\epsilon}^{y_0+\epsilon} \frac{Y_1(y)}{(\overline{u} - c)^2} dy = \left[\frac{\varphi}{\overline{u} - c}\right]_{y_0} \tag{6.40}$$

The integral of (6.40) implies that

$$\lim_{\epsilon \to 0} \int_{y_0-\epsilon}^{y_0+\epsilon} \frac{Y_1(y)}{(\overline{u} - c)^2} dy = 0 \tag{6.41}$$

and the second condition is:

$$\left[\frac{\varphi}{\overline{u} - c}\right]_{y_0} = 0. \tag{6.42}$$

In physical terms, Equations (6.38) and (6.42) , as well as the continuity of φ across the interface, simply express, the continuity of pressure, the continuity of the displacement of fluid particles on both sides of and parallel to the interface, and the continuity of the meridional velocity, respectively [59, 60]. In fact , according to (6.7) and (6.3) the pressure perturbation is given by

$$p' = (\overline{u} - c)\frac{d\varphi}{dy} + \left(\beta y - \frac{d\overline{u}}{dy}\right)\varphi,$$

the meridional velocity (perturbation) is

$$v' = ik\varphi(y)\exp(ik(x - ct)),$$

and the displacement of fluid particule is given by

$$\eta = F(y)\exp(ik(x - ct)),$$

then the velocity and displacement is related by

$$v' = \frac{D\eta}{Dt} = \left(\frac{\partial}{\partial t} + \overline{u}\frac{\partial}{\partial x}\right)\eta = ik(\overline{u} - c)F(y)\exp(ik(x - ct)),$$

we have,

$$F(y) = \frac{\varphi(y)}{\overline{u} - c}$$

The function $F(y)$ must be the same on each side of the interface, thus $F(y)$ must be continuous across the interface. If the profile break occurs at y_0 this condition is the

equation in (6.42). The second jump condition is that the tangential pressure gradient at the interface be given equally on both sides of the interface, this condition is the equation in (6.38). The application of these matching conditions and the appropriate boundary conditions to the solution in each flow region gives the full solution and the dispersion relation for the complex phase speed $c(k)$.

6.7 The Helmholtz shear layer in a β- plane

We consider a simple Helmholtz shear flow with a discontinuity at $y = 0$ (i.e, at the equator):

$$\overline{u}(y) = \begin{cases} 1 & y > 0 \\ -1 & y < 0. \end{cases} \tag{6.43}$$

This example was discussed in [22, 34, 60, etc] for the general case of a (mid-latitude) beta-plane. The velocity profile and the potential vorticity gradient are shown in figure 6.1. The necessary conditions for barotropic instability in (6.4) and (6.4) are satisfied because the potential vorticity gradient changes sign at least once; since $\dfrac{d^2\overline{u}}{dy^2}$ is the derivative of the Dirac delta function, it jumps from $-\infty$ at $y = 0^-$ to $+\infty$ at $y = 0^+$. The perturbation amplitude equation in (6.8) becomes

$$\frac{d^2\varphi}{dy^2} - k^2\varphi + \frac{\beta}{(\overline{u} - c)}\varphi = 0. \tag{6.44}$$

The solution can be written as

$$\varphi(y) = \begin{cases} a_1 \exp(-l_1 y) & y > 0 \\ a_2 \exp(l_2 y) & y < 0 \end{cases} \tag{6.45}$$

and the streamfunction perturbation is given by

$$\psi'(x, y, t) = \begin{cases} a_1 \exp(-l_1 y + ik(x - ct)) & y > 0 \\ a_2 \exp(l_2 y + ik(x - ct)) & y < 0, \end{cases} \tag{6.46}$$

where a_1 and a_2 are two arbitrary constants, and

$$\begin{aligned} l_1 &= \left(k^2 + \frac{\beta}{c - 1}\right)^{\frac{1}{2}} \\ l_2 &= \left(k^2 + \frac{\beta}{c + 1}\right)^{\frac{1}{2}}. \end{aligned} \tag{6.47}$$

When c is complex, l_1 and l_2 are chosen to have positive real parts so that ψ' stays bounded at $y = \mp Y$. The application of the matching conditions (6.38) and (6.42) at $y = 0$ yields

$$-a_1 l_1 (1-c) = -l_2 (1+c) a_2 \tag{6.48}$$

and

$$\frac{a_1}{(1-c)} = -\frac{a_2}{(1+c)}. \tag{6.49}$$

Combining (6.48) and (6.49) yields,

$$l_1 (1-c)^2 + l_2 (1+c)^2 = 0. \tag{6.50}$$

When we replace l_1 and l_2 in (6.50) by their values in (6.47), we find the dispersion relation:

$$c^3 + \frac{3\beta}{4k^2} c^2 + c + \frac{\beta}{4k^2} = 0. \tag{6.51}$$

There are three roots, one of them is real (neutral) and the other two are complex conjugates. The complex roots correspond to the unstable (growing) and damped (decaying) modes. We note that in the case of complex roots, the imaginary part is non-zero for all k, so all the modes are unstable, because 1) β is not large enough to cause the potential vorticity gradient to be of single sign and 2) even the shortest waves sense the change in sign of $\beta - \frac{d^2\overline{u}}{dy^2}$, since $\frac{d^2\overline{u}}{dy^2}$ has both signs right at the point where the profile breaks. Moreover, when $\frac{\beta}{k^2} \longrightarrow 0$, $c \longrightarrow \pm i$ and when $k = 0$, $c \longrightarrow \pm \frac{i}{\sqrt{3}}$.
The dispersion relation is plotted in Fig. 2, where both c_i and c_r are plotted as functions of the non-dimensional zonal wavenumber $k = \frac{2\pi j L_e}{P}$, where $j = 0, 1, 2..., P = 40000$ km and $L_e \approx 1500$ km. From Figure 6.2, we see that while the growth rate kc_i increases linearly with increasing wavenumber, the phase speed c_r is essentially zero, for all wavenumber $k \geq 1$. The non-zero growth at all wavenumbers is consistent with the observation made in the previous paragraph. Also, from Figure 6.2, only large scale perturbations can grow as propagating waves; they propagate westward as Rossby wave packets according to the negative value of c_r on Figure 6.2. Higher modes can only grow as standing waves. Moreover, since the largest growth rates are achieved at the smallest scales, in practical simulations, a numerical viscosity of some sort is needed in order to damp the potential grid-scale instabilities. This increase of growth rates with

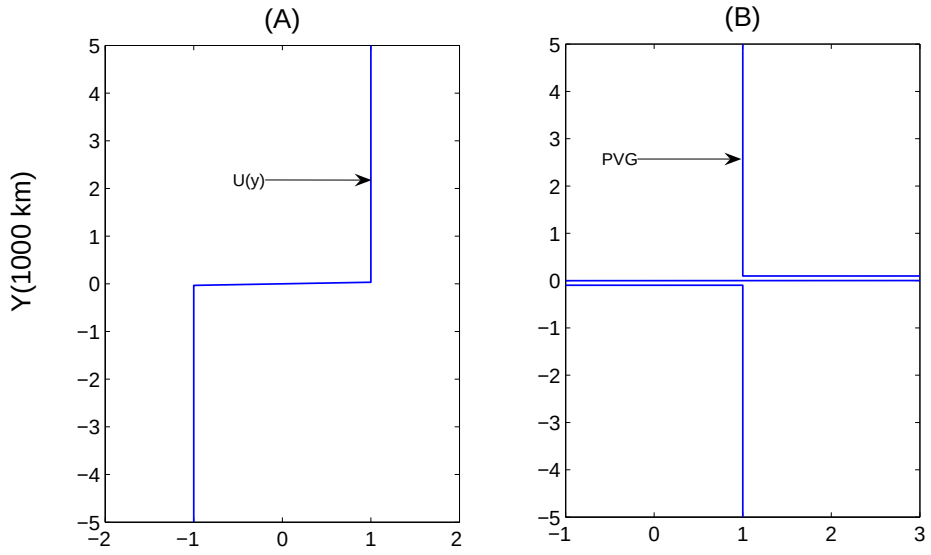

Figure 6.1: The Helmholtz shear layer: (A) $\bar{u}(y)$ and (B) the potential vorticity gradient $\dfrac{\partial \pi}{\partial y} = \beta - \dfrac{\partial^2 \overline{u}}{\partial y^2}$ including a double delta function contribution arising from $\dfrac{\partial^2 \overline{u}}{\partial y^2}$ at the profile break at $y = 0$ [59, 60].

increasing wavenumber is known as the ultra-violet catastrophe in the numerical analysis community. As it is iterated below, for this reason Arakawa's methods necessitates a viscosity term to be added to the vorticity equation.

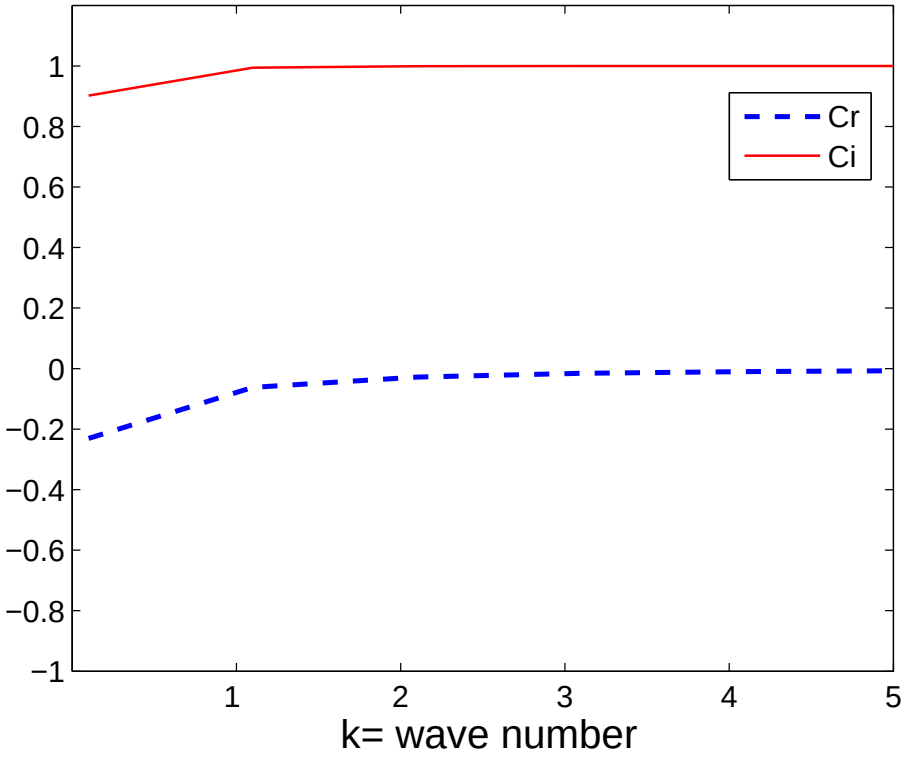

Figure 6.2: Dispersion relation for the Helmholtz instability with $\beta = 1$. The phase speed c_r and the normalized growth rate ci of the unstable mode are plotted as function of the non-dimensional zonal wavenumber **k** [59, 60].

Chapter 7

A Numerical Simulation of the Barotropic instability on the Equatorial β-plane

7.1 Introduction

In this chapter we conduct a numerical investigation of the barotropic instability for the Helmholtz shear layer example described above in the previous chapter by using the two different numerical methods developed in Chapter 3: the Arakawa Jacobian scheme [1], which is specifically designed for the barotropic vorticity Equation (2.50) and which is widely used in the atmosphere-ocean community, and the fourth order essentially non-oscillatory ENO scheme of Osher and Shu [41]. The latter was originally designed for the Hamilton-Jacobi equations and used to track sharp fronts, but in essence it can be implemented for any first order non-linear evolution PDE, and in particular for the vorticity advection Equation (2.50). In the Osher and Shu scheme, in addition to the CFL condition, numerical instabilities are controlled via a fourth order non-linear stencil so that the numerical solution is essentially non-oscillatory. It important to note here that while the ENO-4 scheme is fourth-order accurate in smooth regions and bears a certain amount of numerical viscosity that smooths potential grid scale oscillations that are caused by discontinuities and sharp gradients, the Arakawa Jacobian scheme is a (linear) second-order accurate scheme that preserves energy and enstrophy at machine precision. As such, the addition of an artificial viscosity term $\upsilon\Delta\xi$ to the vorticity

equation, is required to cope with the potential grid-scale instabilities due to growing small scale modes as discussed in the previous chapter. Such term is not needed for the ENO-4 scheme because of the built in numerical viscosity [32]. For time integration, the Osher and Shu scheme is coupled to a (TVD) fourth order Runge-Kutta method (ENO-4) while the Arakawa Jacobian uses a second order Runge-Kutta method. We are mainly interested in the nonlinear evolution of the growing modes found in the linear analysis of the previous chapter and how each one of the methods handles this problem [26].

7.2 Numerical Simulation

We will restrict the domain to a rectangular strip, which is periodic in x, centered at equator, and limited by rigid walls located at a distance $Y = 5000$ km North and South of the equator. The zonal period P is set equal to the perimeter of the earth at the equator: $P = 40000$ km. At this point it is useful to introduce the potential vorticity-stream function formulation (2.50) for the barotropic system (6.1). We rewrite the formulation:

$$\begin{cases} \dfrac{\partial \xi}{\partial t} + J(\psi, \xi) = 0 \\ \Delta \psi = \xi - y \\ u = -\dfrac{\partial \psi}{\partial y}, v = \dfrac{\partial \psi}{\partial x}, \end{cases} \tag{7.1}$$

where ψ is the streamfunction, $\xi = v_x - u_y + y$ is the potential vorticity. Here $J(\psi, \xi)$ represents the Jacobian determinant of ψ and ξ:

$$J(\psi, \xi) = -\frac{\partial \psi}{\partial y}\frac{\partial \xi}{\partial x} + \frac{\partial \psi}{\partial x}\frac{\partial \xi}{\partial y}. \tag{7.2}$$

To solve the coupled system in (7.1) and (7.2) the Arakawa Jacobian scheme [1] is combined with a second-order Poisson solver for the stream-function and the fourth order ENO-4 scheme of Osher and Shu [41] is combined with a fourth-order Poisson solver. Both Poisson solvers are based on centered finite differences of second and fourth order, respectively [28, 33]. Both methods were validated through Rossby wave packets and pure shear flow-exact solutions and the results, were found very satisfactory see [25] or Chapter 5. Let us now get back to the Helmholtz velocity profile of the previous chapter: $(u, v) = (\overline{u}(y), 0)$, which, in theory, is an exact solution for the system (6.1)

despite the discontinuity jump. From Equations (7.2) we have:

$$u = \overline{u}(y) = -\frac{\partial \overline{\psi}}{\partial y} \text{ and } v = 0 = \frac{\partial \overline{\psi}}{\partial x} \tag{7.3}$$

which gives

$$\overline{\psi}(y) = \begin{cases} -y & \text{if } y > 0 \\ y & \text{if } y < 0 \end{cases} \tag{7.4}$$

and

$$\overline{\xi}(y) = \Delta\overline{\psi} + y = -2\delta_0 + y \tag{7.5}$$

where δ_0 is the Dirac delta function at $y = 0$. For a proper numerical treatment with the present schemes, some smoothing of the singularity is required. The Dirac delta function is thus replaced by a regularizing sequence (ρ_ε), which converges towards δ_0 when $\varepsilon \to 0$. Let

$$\rho_\varepsilon(y) = \begin{cases} 0 & |y| > \varepsilon \\ \frac{1}{\varepsilon^2}y + \frac{1}{\varepsilon} & -\varepsilon \leq y \leq 0 \\ -\frac{1}{\varepsilon^2}y + \frac{1}{\varepsilon} & 0 \leq y \leq \varepsilon \end{cases} \tag{7.6}$$

where ε is a small positive real number. In our numerical solution, we take $\varepsilon = \Delta y$ for the second-order method that couples the Arakawa Jacobian and the second order Poisson solver, and $\varepsilon = 8\Delta y$ for the fourth-order method. Where Δy is the grid spacing in the North-South direction. Non-homogeneous Neumann and homogeneous Dirichlet boundary conditions are used at the walls, for the stream-function and potential vorticity, respectively.

$$\frac{\partial \psi}{\partial y}(Y) = -1, \quad \frac{\partial \psi}{\partial y}(-Y) = 1 \tag{7.7}$$

$$\omega = \xi - y = 0 \quad \text{at } y = \pm Y. \tag{7.8}$$

We consider solutions of (7.1) that are initially perturbations of the Helmholtz shear, on the form

$$\psi(x, y, t) = \overline{\psi}(y) + \mu\psi'(x, y, t)$$

$$\xi(x, y, t) = \overline{\xi}(y) + \mu\Delta\psi'(x, y, t) = -2\delta_0 + y + \mu\Delta\psi'(x, y, t)$$

where $\psi'(x, y, t)$ is given in (6.46) and $\mu > 0$ is a (small) dimensionless amplitude parameter and c is the complex root of (6.51) corresponding to the growing mode. It is easy to find the roots of (6.51) as a function of β/k^2. For $\beta = 1$ (consistent with our

non-dimensional units) and $k = \dfrac{2\pi k'}{P}$ with $P \approx 26.66$ is the non-dimensional length of our computational domain in the x-direction, (in this case $k' = 10$-waves) we find three roots:

$$\begin{cases} c_1 = -0.0448 + 0.9970i \\ c_2 = -0.0448 - 0.9970i \\ c_3 = -0.0451. \end{cases} \tag{7.9}$$

The unstable mode corresponds to

$$\begin{cases} c = -0,0448 + 0.9970i \\ l_1 = 0.106 + 2.2539i \\ l_2 = 0.106 + 2.4661i. \end{cases} \tag{7.10}$$

To be more precise, we run the two methods forward in time for two values of the parameter μ (a weak and a strong perturbation) with the initial condition given by

$$\psi(x, y, 0) = \overline{\psi}(y) + \mu\psi'(x, y, 0) \tag{7.11}$$

$$\xi(x, y, 0) = \overline{\xi}(y) + \mu\Delta\psi'(x, y, 0) = -2\rho_\varepsilon(y) + y + \mu\Delta\psi'(x, y, 0) \tag{7.12}$$

where ψ' is given by equations (6.46) and (7.10) and ρ_ε and $\overline{\psi}$ given by (7.6) and (7.4).

We recall here that the method of Arakawa tends to develop numerical instabilities on the grid scale and a dissipation term $\upsilon\Delta\xi$, where Δ is the horizontal Laplacian operator, is added to the vorticity advection equation in order to achieve meaningful results. This is not the case for the code ENO-4 which has its own numerical dissipation built in. A trial-and-error procedure revealed that $\upsilon = 0.006$ is an optimal choice for the range of grid sizes used here: 64×38 to 256×150. A more systematic strategy would be to use an υ that depends explicitly on Δx and/or Δy.

We consider two initial conditions on the form of the wave modes in (7.11)-(7.12): a weak perturbation with $\mu = 0.01$ and a strong perturbation of size $\mu = 0.5$. The contour plots of the initial (background plus perturbation) stream function and velocity arrows are shown in Figure 7.1, based on the finest grid 256×150, for the two parameter values $\mu = 0.01$ and $\mu = 0.5$. These two initial conditions are then evolved for a long period of 100 days using the two numerical methods and three different grids: 64×38, 128×75, and 256×150, in the x-zonal and y-meridional directions, respectively, yielding a total of 12 numerical experiments. The time step is based on the CFL condition of stability for each method. For the sake of completeness the various time steps used in this study are shown in Table 7.1.

Table 7.1: Time steps (in non-dimemsional unist) used in the various simulation conducted here. See text for details.

Grids	Arakawa	ENO-4
64×38	$1.94E-002$	$1.16E-002$
128×75	$5.93E-003$	$6.43E-003$
256×150	$1.4E-003$	$1.86E-003$

In addition, because of the stencil structure differences, the two numerical methods respond very differently to the width, ε, of the regularizing function ρ_ε in (7.6). While the Arakawa Jacobian works well with a smoothing width as small as $\varepsilon = \Delta Y$. Because of its non-linear stencil, the ENO-4 scheme requires a much wider smoothing region. A value as large as $\varepsilon = 8\Delta Y$ is required for the ENO-4 scheme.

The energy,

$$E(t) = \frac{1}{2}\int_{-Y}^{Y}\int_{0}^{P} |\nabla\psi(x,y,t)|^2 \, dxdy$$

and enstrophy

$$\mathcal{E}(t) = \frac{1}{2}\int_{-Y}^{Y}\int_{0}^{P} |\Delta\psi(x,y,t)|^2 \, dxdy$$

that are associated with the smoothed initial profile (smoothed background plus initial perturbation) are reported in Table 7.2 for the three grid sizes and for the two values of the width of the regularizing function in (7.6) that are used for the two methods.

From Table 7.2, we can see that although the solution at $t = 0$ is analytically the same, the associated energy and enstrophy depend on both the grid size and the width of the regularizing function. We note that the choice of ε value may have a significant impact on the numerical solution especially for the ENO-4 method on the coarse grid with only 38 points in the y-direction. In fact, this might be the reason why, in the results reported below, the ENO-4 coarse resolution solutions are so different from the rest, for both perturbations. However, according to numerical tests that are not shown here, these two choices are the minimal values of ε for which respectively the two methods seem to give meaningful results. We note however that the enstrophy is more sensitive to changes in grid size and the width of regularizing function. In fact changes in the width of the regularizing function affect very little $E(0)$ and therefore

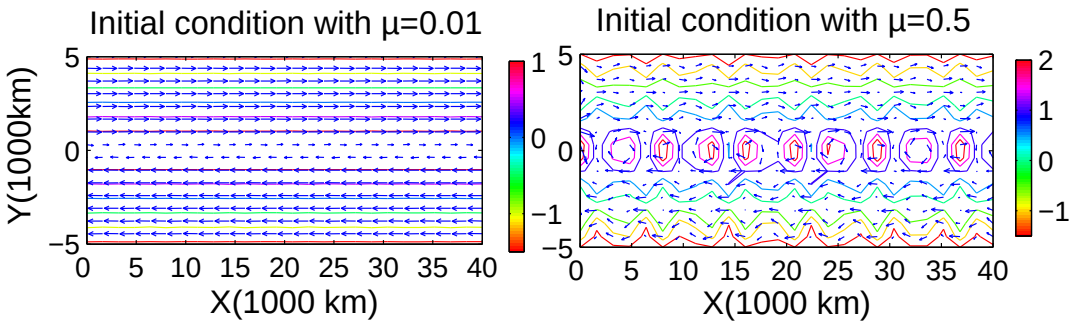

Figure 7.1: The contours-plots of total streamfunction and velocity profile at t=0.

only one value per grid is reported (for each perturbation size) in Table 7.2. We note in particular that $\mathcal{E}(0)$ increases significantly with the grid size while $E(0)$ doesn't. This is due to the fact that the Dirac δ function is not in L_2, which makes the L^2 norm of the regularizer ρ_ϵ grow without bound when $\epsilon \longrightarrow 0$.

7.2.1 Small perturbation

The contours of the total stream function and the velocity vectors, at $t = 100$ days, obtained by both the Arakawa and ENO-4 methods with the amplitude parameter $\mu = 0.01$, are shown in Figure 7.2. Except for the ENO-4 method on the coarsest grid in Panel (D), the two methods yield almost identical solutions; while the coarse grid solution in Panel (D) exhibits a flat profile that has zonally parallel stream lines, all the other solutions have curved streamlines near the equator, where the discontinuity was initially placed, that are to some extent grid and somewhat method dependent, in terms of both their structures and amplitudes. As noted above the deficiency of the ENO-4 coarse grid solution might be due to the high ratio between ε and the total number of grid points in the y-direction.

The time histories of $E(t)/E(0)$ and $\mathcal{E}(t)/\mathcal{E}(0)$ are plotted in Figure 7.3. We note that the energy is relatively conserved, within 75% to 80% of its initial value, while the enstrophy displays various behaviors depending on the grid size and method used. Except for the case of the coarsest grid with ENO-4, the enstrophy decreases a great deal during a transient period of roughly 20 days and, in some cases, reaches a level which is more than 50% below its initial value. After this transient period, the enstrophy dissipation seems to follow the same slope as that of the energy, except for the coarse

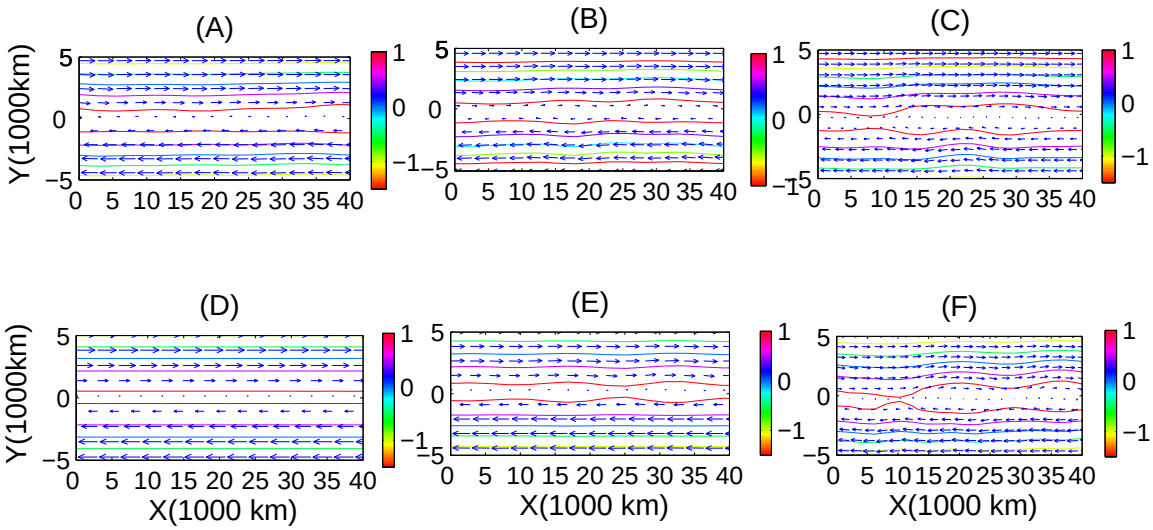

Figure 7.2: The contour plot of the total streamfunction and velocity arrows at $t = 100$ days for an initial perturbation of size $\mu = 0.01$. (A), (B), and (C) are obtained by the Arakawa method with a viscosity $\upsilon = 0.006$ while (D), (E), and (F) are obtained with the ENO-4 scheme with grid sizes 64×38 (A and D), 128×75 (B and E), and 256×150 (C and F).

Table 7.2: Grid dependence of energy and enstrophy of the perturbed shear solution at time $t = 0$ for the weak and strong perturbations.

$\mu = 0.01$			
Grid	$E\,(0)$	$\mathcal{E}\,(0)$ Arakawa code	$\mathcal{E}\,(0)$ ENO-4 code
64×38	0.50150191	0.29642776	0.10108676
128×75	0.50411647	0.59719193	0.19510097
256×150	0.50049725	1.12537820	0.38199015
$\mu = 0.5$			
Grid	$E\,(0)$	$\mathcal{E}\,(0)$ Arakawa code	$\mathcal{E}\,(0)$ ENO-4 code
64×38	0.91284319	6.94654430	4.81485961
128×75	0.98175762	8.16705125	6.00498203
256×150	0.99415416	10.0772929	7.20432832

mesh case in Panel (D). This can be explained by the fact that initially the numerical solutions have a significant amount of enstrophy stored at small scales due to the presence of the (smoothed) delta function; it is less so for the energy which is based on a Heaviside function background flow. The small scale enstrophy is thus dissipated during the first 20 days thanks to the numerical viscosity (which is added to the Arakawa scheme or intrinsically present in the ENO-4 scheme). After this period, both energy and enstrophy continue to be dissipated at the rate at which they are being cascaded from large scales to small scales. However, the case of the coarsest mesh with ENO-4 is an exception; while energy seems to obey the same dissipation rate, enstrophy remains almost constant. This behavior is consistent with the contour profiles in Figure 7.2 where the solution corresponding to the ENO-4 scheme on the coarsest mesh displays a linear shear profile (which is an exact solution for the barotropic equation) for which nonlinear transfer of enstrophy appears to be negligible.

Except for the relatively small structure, which is seen more clearly on the finer grid plots, in Figure 7.2, no other sign of the growth of the instability can be seen in this simulation. In fact because the initial perturbation is very smaller compared to the background flow, the associated linear growth, which in theory, is effective only for a short period of time, is being camouflaged by the numerical dissipation at small scales. Nonetheless, we can argue that the main role of the instability is to remove energy from the background flow until this later equilibrates and becomes stable.

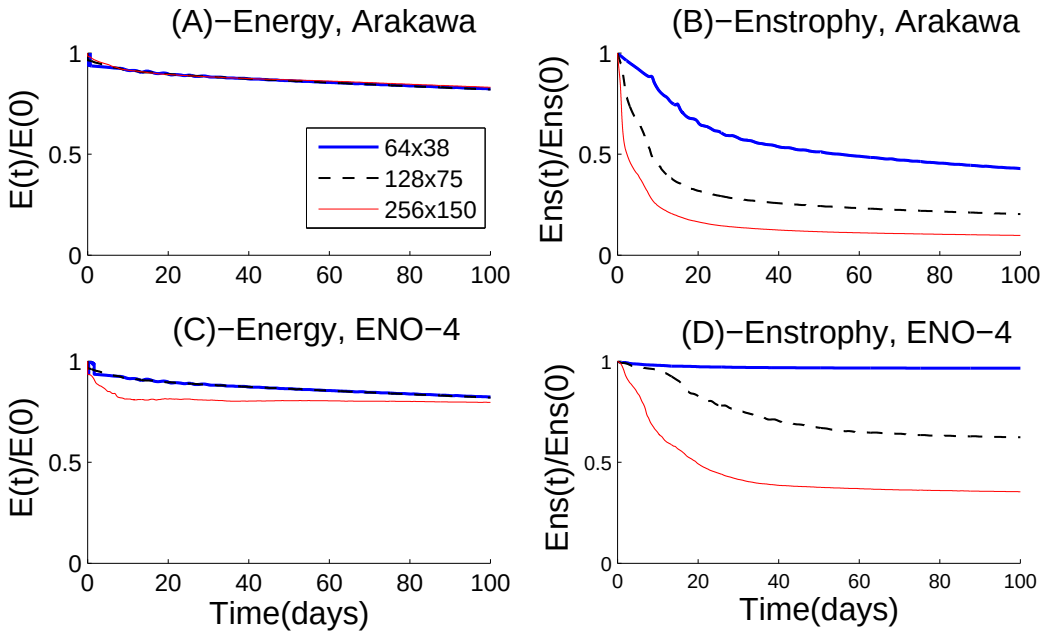

Figure 7.3: Energy and Enstrophy time series with $\mu = 0.01$. (A) and (B): Arakawa Jacobian method with viscosity $\upsilon = 0.006$. (C) and (D): ENO-4. Thick curves: 64×38. Thin light curves: 128×75. Thin dark curves: 256×150.

In Figures 7.4 and 7.5, we plot, respectively, the initial background profile of the stream function and the gradient of the potential vorticity, $\beta - \dfrac{d^2\bar{u}(y)}{dy^2}$, together with their counterparts obtained by averaging each one of the six numerical solutions (corresponding to the three grids and the two methods) in time, between times 50 days and 100 days, and in the zonal direction, over the whole domain. Ignoring the upward shift in the stream function, which is an artifact of the numerical methodology that assumes that the streamfunction has a zero mean, we see that, for this small perturbation, the main effect of the barotropic instability is to smooth out the flow profile in the vicinity of the equator resulting in a stable profile. We note that the six profiles are approximately the same, independent of the grid size and/or the method used.

The stability of the final profiles is confirmed by the plots of the potential vorticity gradients in Figure 7.5. We recall that according to (6.4) and (6.4), a necessary condition for the barotropic instability is that the background potential vorticity gradient changes sign somewhere in the domain. As we see from Figure 7.5, while this condition is clearly satisfied by the initial profile, all the other profiles are positive for all y values.

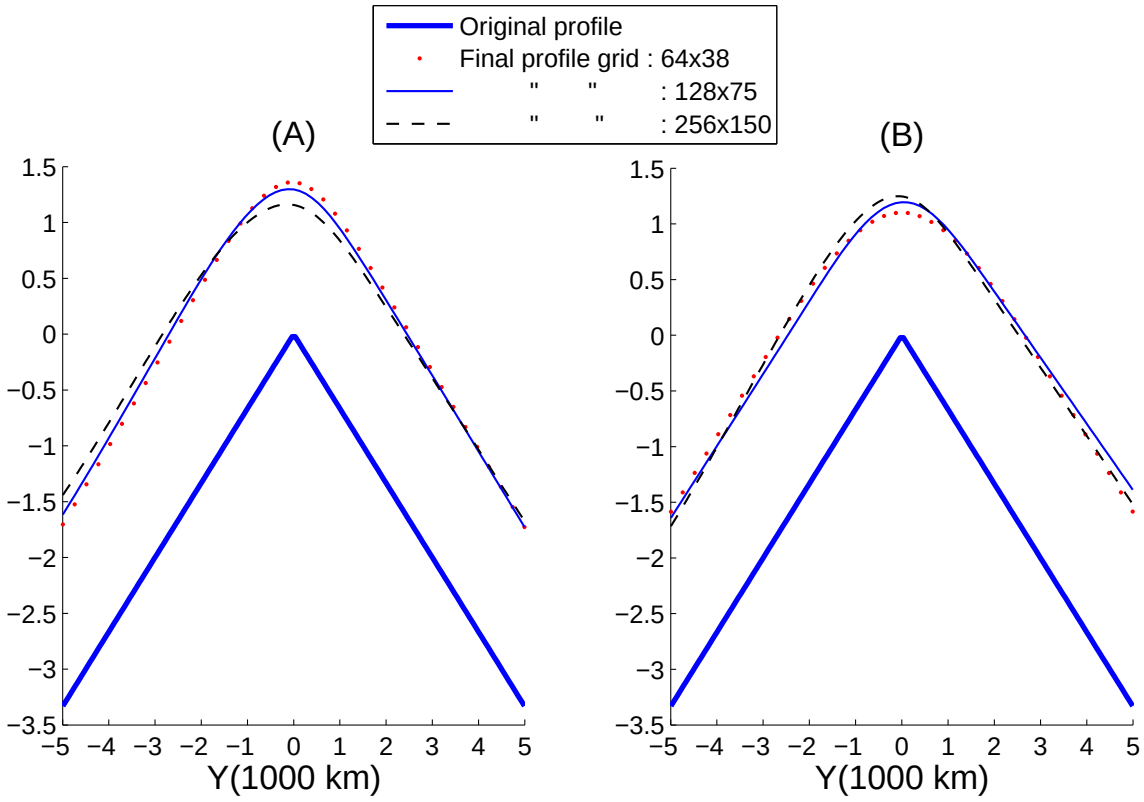

Figure 7.4: Initial and final profiles of the streamfunction for the case of weak perturbation with $\mu = 0.01$. The final profiles are obtained by a running average in both x and t–over the last 50 days of the simulation. (A): Arakawa's method with a viscosity coefficient $\upsilon = 0.006$. (B); ENO-4 scheme.

We note that for the sake of clarity, the initial potential vorticity gradient profile, which is displayed in Figure 7.5, corresponds to the derivative of the smoothed delta-function on the coarsest grid.

7.2.2 Large perturbation

In figure 7.6, we show the total flow profile (contours of the stream function and velocity vectors) of the numerical solution obtained on the coarse grid 64×38 at times 10 days, 50 days, and 100 days by both the Arakawa and ENO-4 methods when the size of the initial perturbation is fixed to $\mu = 0.5$. Figures 7.7 and 7.8 report the same solution profiles for the finer grids of 128×75 and 256×150, respectively. The most remarkable

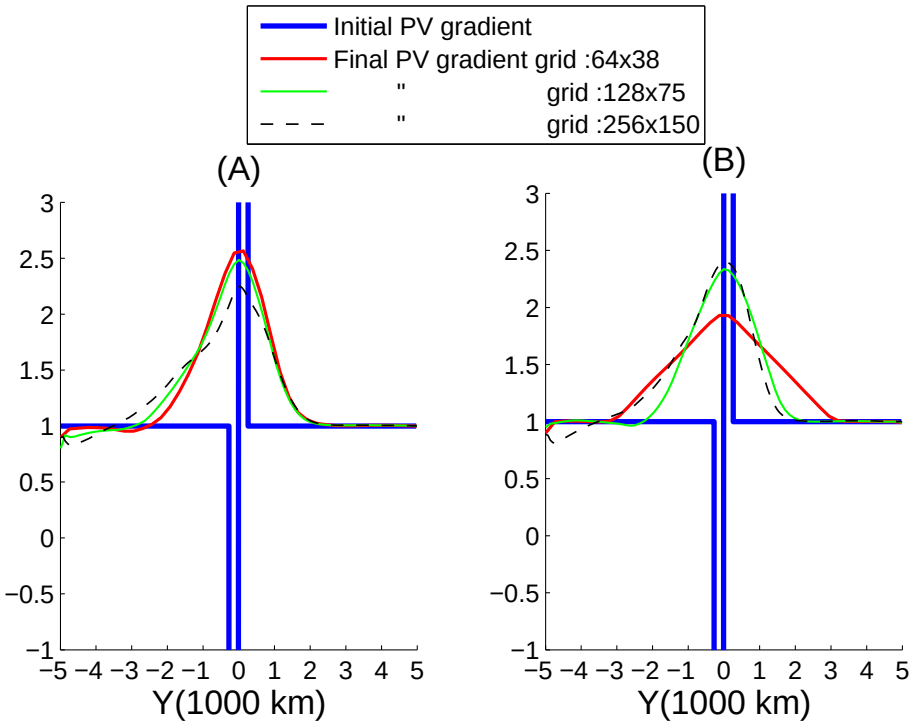

Figure 7.5: Same as 7.4 but for the vorticity gradient.

feature that we see in these results is the development and persistence of a large-scale vortex that is more or less centered at the equator, for both methods, on the last panels of Figure 7.8 corresponding to the finest mesh. A detailed documentation (not reported here) of a longer (and more compact) sequence of solutions suggests that a scenario of an inverse cascade of energy occurs during a transient period during which the ten vortices that characterize the initial solution on the right panel of Figure 7.1 progressively merge into fewer and larger vortices and ultimately converge to the large scale vortex shown on Figure 7.8 at $t = 100$ days. The same is somewhat true for the other two simulations, especially, for Arakawa's method on the left Panels of Figures 7.6 and 7.7 although the merging of the vortices seems to occur on a smaller time scale. The solution corresponding to the ENO-4 method in Figures 7.6 and 7.7 display a rather different behavior. While the coarsest-mesh solution tends to exhibit very little variability, which is rather located near the Northern boundary, the intermediate grid solution seems to converge (in time) towards an elongated vortex somewhat located in the North part of the domain.

By comparing the results in Figures 7.6, 7.7, and 7.8, we can conclude that both methods seem to converge with the grid refinement, qualitatively and somewhat quantitatively, to the same long-time solution which consists of a single large scale vortex which is more of less centered near the equator. However, Arakawa's method seems to converge faster than the ENO-4 method. Even at the coarsest mesh of 64×38 points, Arakawa's method captures the important trend of the converged solution in Figure 7.8. For the ten vortices initial solution, this amounts to roughly 6×38 points per vortex. The ENO-4 method seems to be very sensitive to the number of grids points per vortex that are needed in order to capture some of the main features of the solution; even with 128×75 (i.e, 13×75 grid points per vortex) the long-time vortex seems to be shifted to the Northern part of the domain.

The relative evolution of the energy and enstrophy for the case of a large initial perturbation is displayed in Figure 7.9. Similarly to the case of a small perturbation, the numerical solutions seem to lose most of their enstrophy during a transient period of about 20 days, for both methods and for all the three grids. The ENO-4 solution corresponding to the finest grid may appear to saturate at a higher enstrophy level. However, a quick comparison of the corresponding initial enstrophies in Table 7.1, suggests that the two finest grid solutions may actually have comparable amounts of

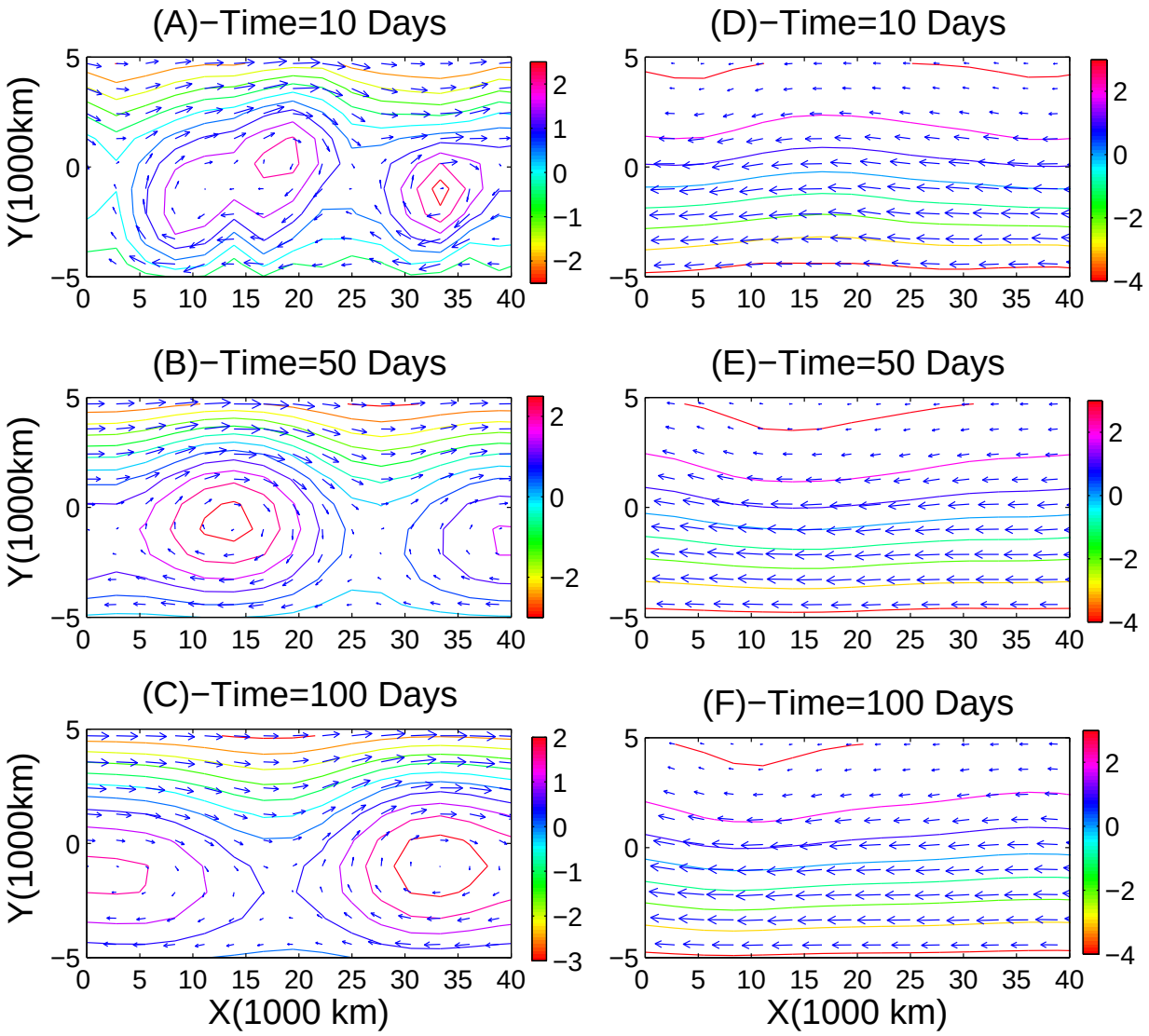

Figure 7.6: xy-contours of the total stream-function and total velocity vectors at times $t = 10$ days, $t = 50$ days, and $t = 100$ days in the case of the large perturbation $\mu = 0.5$ obtained on the coarse grid 64×38. Panels (A), (B), and (C): Arakawa's method, with $\upsilon = 0.006$. Panels (D), (E), and (F): ENO-4 scheme.

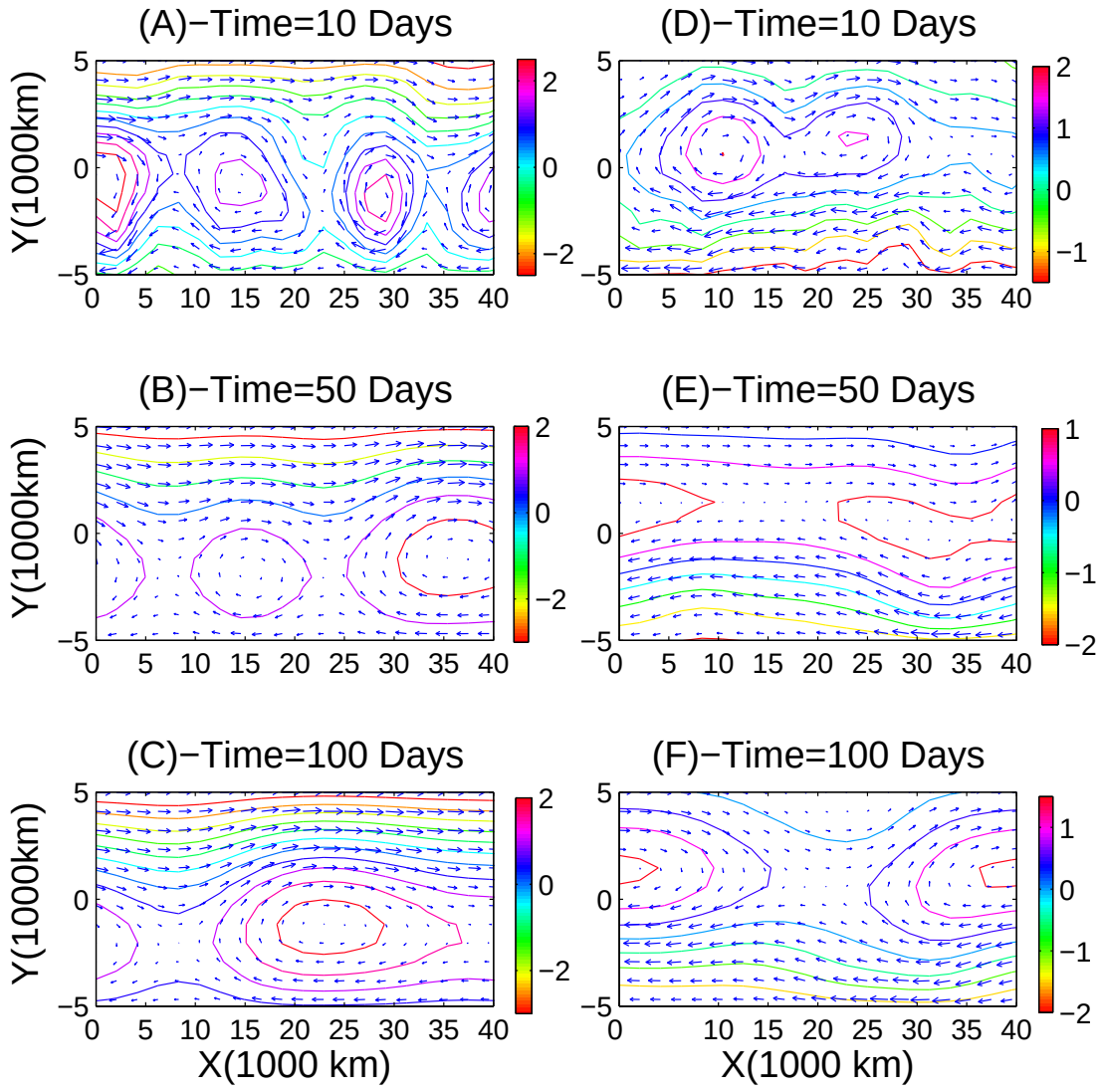

Figure 7.7: Same as in fig 7 but for finer grid: 128×75.

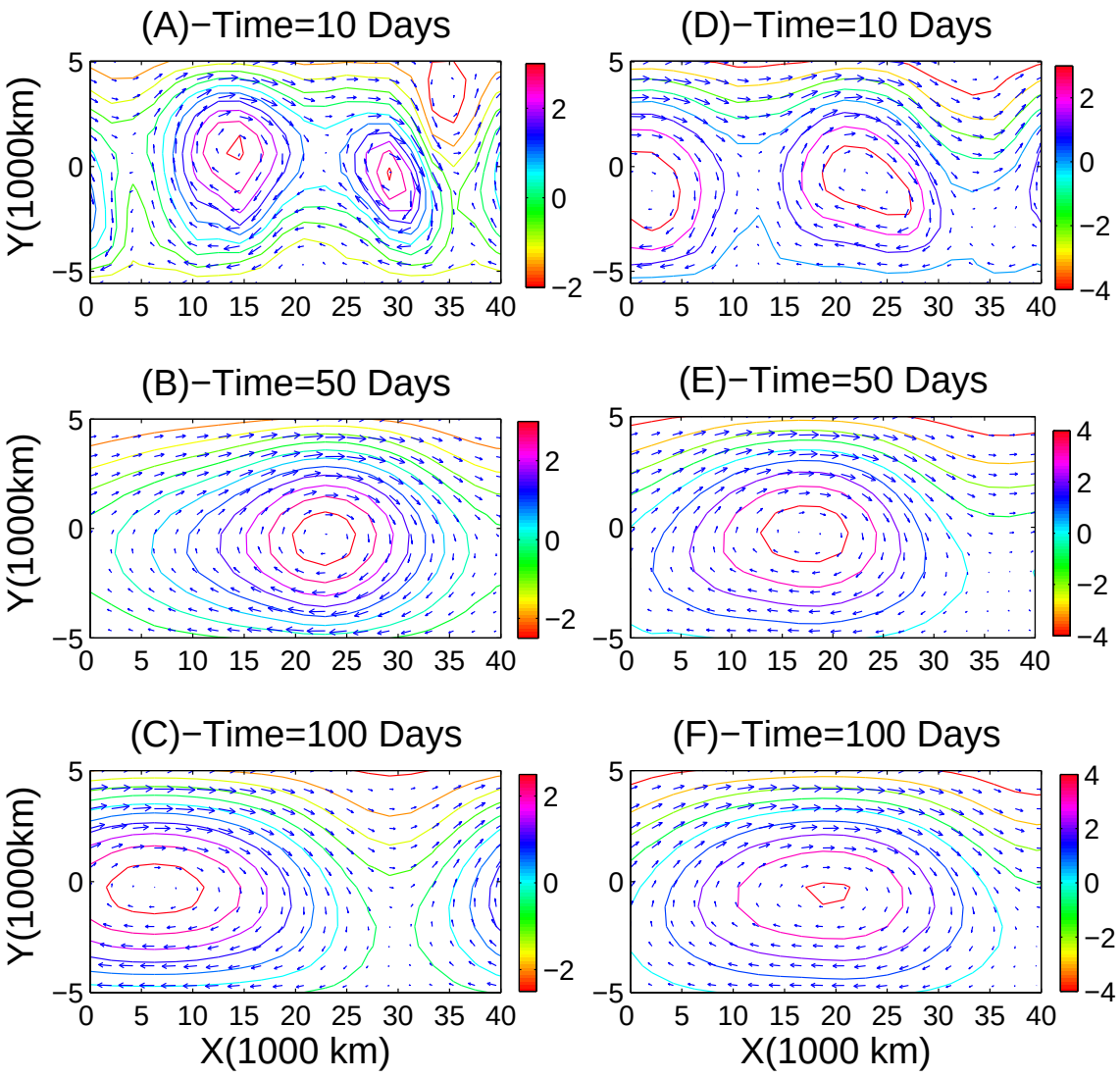

Figure 7.8: Same as in Figure 7.6 but for finest grid: 256×150.

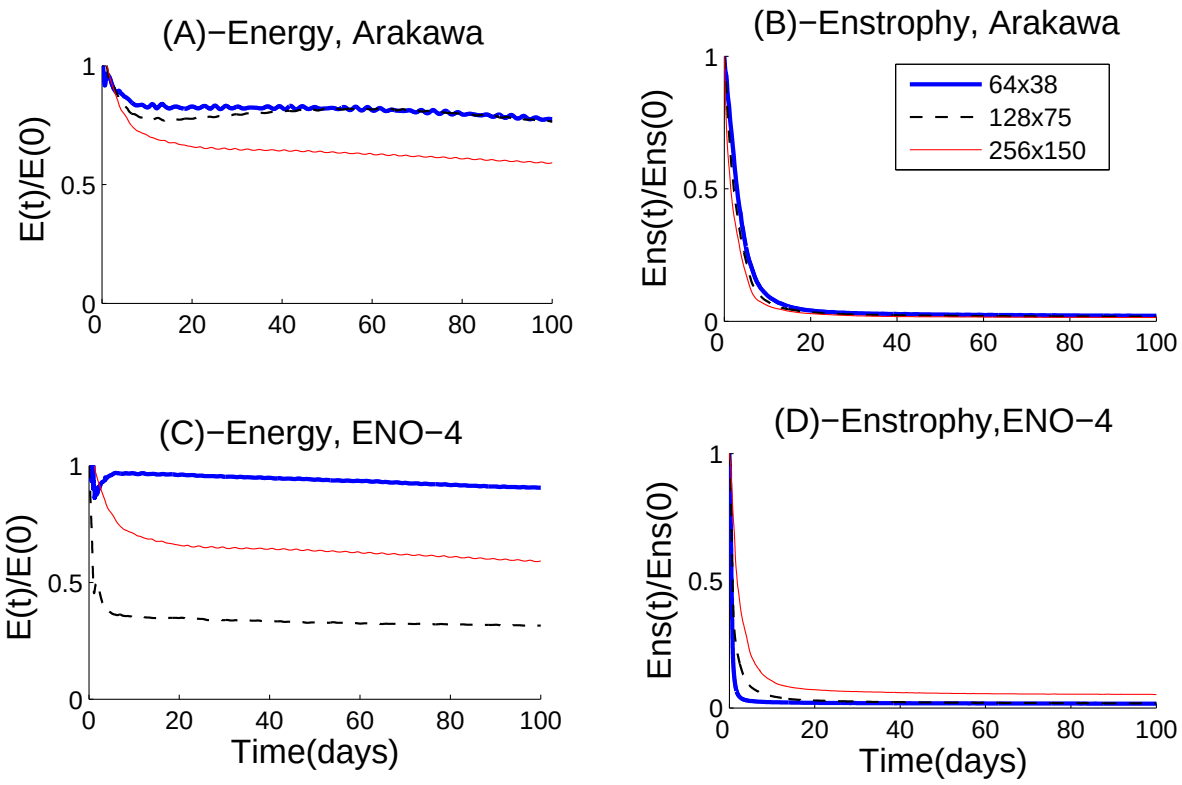

Figure 7.9: Energy and Enstrophy time series in the case of a large perturbation $\mu = 0.5$ for the three different grids. (A) and (B): Arakawa Jacobian method with $\upsilon = 0.006$. (C) and (D): ENO-4.

enstrophy, consistent with the resemblance of the two flow profiles depicted on the bottom of Figure 7.8.

The energy time series behaves very differently than that of the weak perturbation case in Figure 7.3. In the case of Arakawa's method, there is a clear trend which is somewhat easy to understand; the more there is energy at small scales initially the more this energy is dissipated during the short transient period. According to Table 7.1, at $\mu = 0.5$, the 256×150 grid has by far the largest initial energy, at small scales, so it is expected to dissipate more, although this trend is not strictly monotonic. However, a strict analogy is hard to make here given that the regularizing functions change with the grid size.

The energy behavior in the case ENO-4 method is the least intuitive. For the coarsest grid case, the energy first goes quickly down then up and stays constant thereafter. This is only possible if the scheme actually develops a numerical instability during the energy uprising time, because the actual physical system conserves energy. This is possible giving the fact that the scheme is only essentially non-oscillatory; there is still a potential for oscillations if the mesh space is not wide enough for the stencil to avoid the discontinuities. Another counterintuitive behavior resides in the fact that the intermediate mesh solution appears to be more dissipative than the one corresponding to the finest mesh. This however can be explained by the differences in the corresponding solutions, as shown on the right panels in Figures 7.7 and 7.8, respectively; the vortex merging in the 128×75 solution occurs on a much longer time scale, which appeals for more energy dissipation.

The profile of the stream-functions and potential vorticity gradients, for both the initial and long-time solutions, are shown in Figures 7.10 and 7.11. The initial profiles are those of the smoothed background shear while the final ones are obtained by a space and time averaging as in the case with the small perturbation above. We note that the stream-function profiles are now more grid-dependent than in the case of a weak perturbation. Moreover, while the three Arakawa profiles are consistent with each other (they are at least qualitatively similar), those obtained by the ENO-4 scheme are all over the place: while the two coarse mesh profiles are skewed towards the Northern part of the domain, consistent with the location of the variability in Figures 7.6 and 7.7, the finest grid profile is more or less identical to the one obtained with the Arakawa Jacobian method on the same mesh. The same conclusion can be drawn for

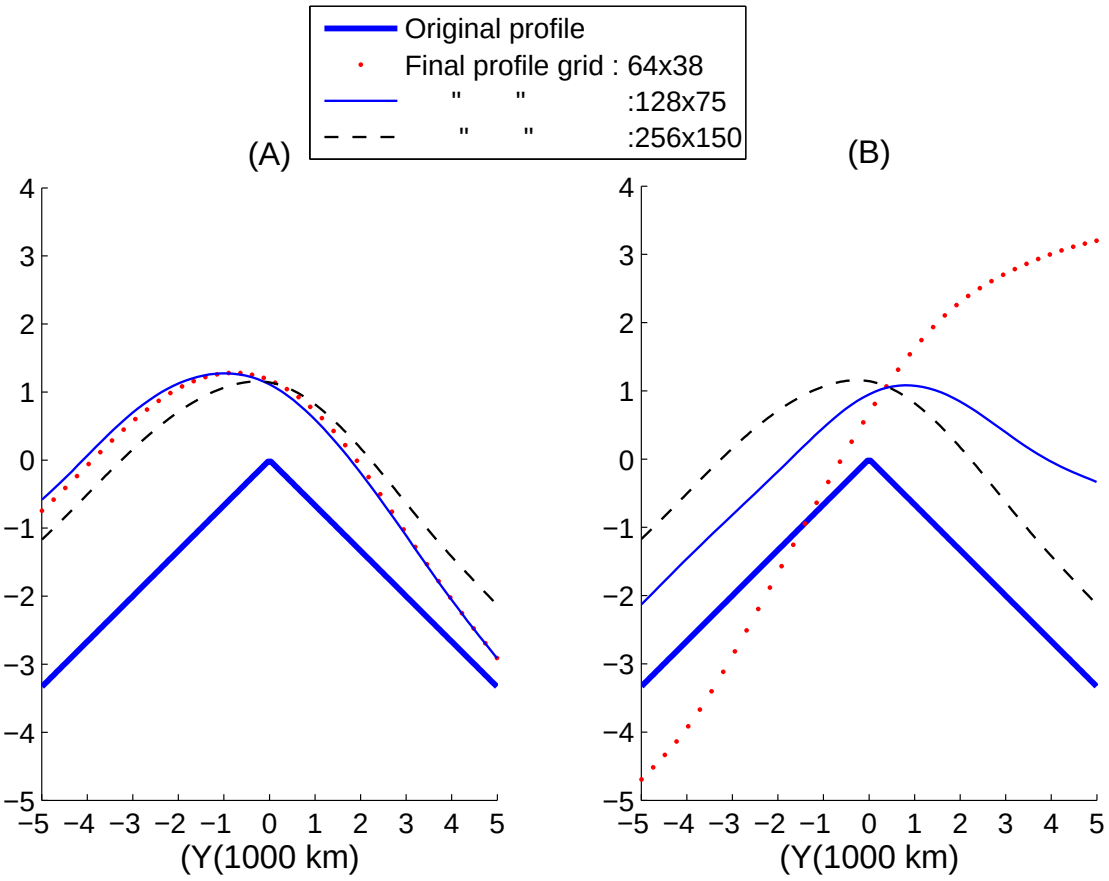

Figure 7.10: Original and final profile (averaged in x and t-over the last 50 days) of the stream-function computed on three different grids for the case of a strong perturbation $\mu = 0.5$. (A) Arakawa's method with a viscosity coefficient $\upsilon = 0.006$. (B): ENO-4.

the potential vorticity profiles in Figure 7.11 in addition to the fact that similarly to the weak perturbation case in Figure 7.5, all the six final profiles appear to satisfy the (sufficient) condition for barotropic stability.

To gain more physical insight into the numerical solutions obtained in this case of a large perturbation, we plot in Figure 7.12, the space-time contours of the meridional average of the six streamfunctions. Such contour plots are known in the atmosphere-ocean science community as the Hovmöller diagrams; they are used to detect the signatures of zonally propagating wave disturbances that may exist in the data as the wave crusts and wave troughs would describe streaks corresponding to the characteristic lines of the underlying waves. Thus accordingly, we can see on all the six panels in Figure 7.12, a

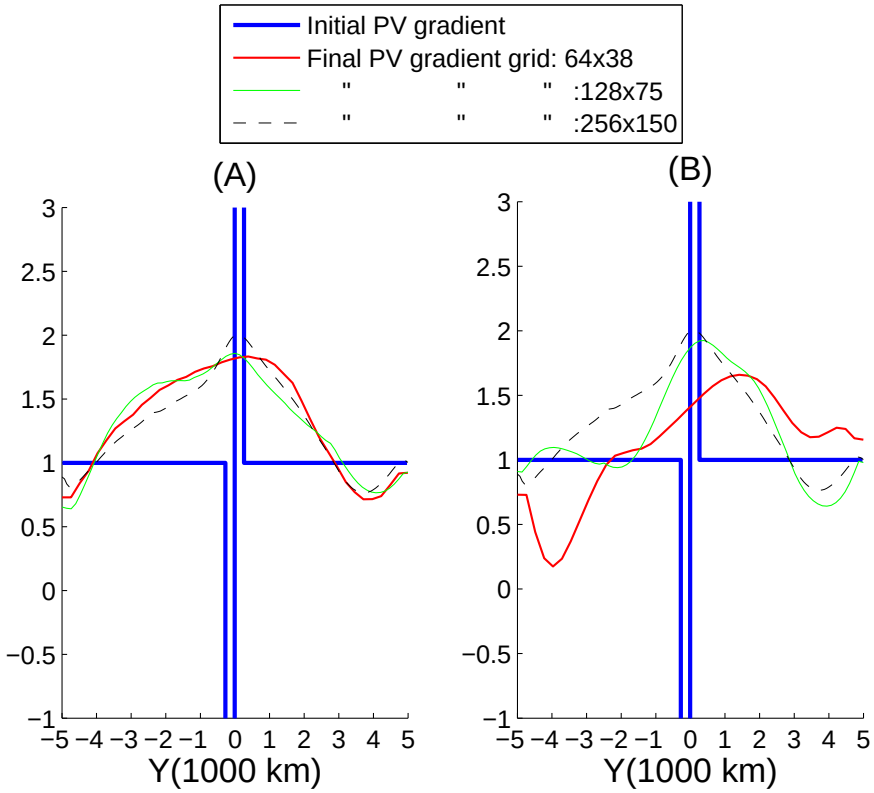

Figure 7.11: Same as Figure 7.10 but for the gradient of the potential vorticity. To produce these profile, the same procedure as in Figure 7.5 is used.

disturbance that propagates westward (to the left) and circles the zonal domain roughly every 3 days. The two panels (A) and (B) corresponding to the Arakawa solution on the 64×38 and 128×75 grids, respectively, appear to have, in addition, a much slower disturbance superimposed on top of the former. We note that the westward propagation of the planetary scale vortex disturbance is consistent with the fact that the baroclinic instability predicts the growth of planetary scale (i.e. small wavenumber) westward propagating modes (see Figure 6.1).

According to linear theory, with respect to a homogeneous background, the barotropic Rossby wave dispersion relation satisfies $\omega = -\frac{\beta k}{l^2+k^2}$ [42] where ω is the frequency, k and l are the zonal and meridional wavenumbers, and β is the Coriolis parameter. For a planetary scale disturbance with $k = 2\pi/P$ and $l = \pi/2Y$, corresponding to a wave that has one full wavelength along x and a half wavelength along y, relative to the computational domain, we get a Rossby wave phase speed of

$$\frac{\omega}{k} = -\frac{\beta}{k^2 + l^2} \approx -180 \text{ m s}^{-1},$$

which is within is the bulk of the characteristic speed of roughly $40,000/2.85$ km day^{-1} $\approx$ 162 m s^{-1} which as suggested by the slopes of the wave streaks in Figure 7.12. However, there is a significant a phase lag between the propagating vortices in Figure 7.8, obtained by the Arakawa method and the ENO-4 scheme, respectively. While the Arakawa solution in Fig. 7.12 (C) has a period of roughly 2.85 days while the ENO-4 solution in Fig. 7.12 (F) has a period of 3.33 days, i.e, the ENO-4 wave solution seem to move much slower than the Arakawa one. This is beyond the numrical truncation errors because as demonstrated by the validation tests in chapter 4 it is actaully the ENO-4 method that seems to over estimate the phase speed of the Rossby wave packet exact solutions while the Arakawa method appears to slightly under estimate it. Therefore an explanation for the period difference between the waves in Figs. 7.12 (C) and (F), respectively, can come only from differences in dynamical and physical structure of the two waves.

While the phase speed of the converged solution corresponds roughly to that of a planetary scale Rossby wave, its structure is not that of a linear wave. The single propagating vortex may however bear some resemblance to tropical depressions that are associated with African Easterly waves, which are believed to play a central role in the formation of hurricanes as they propagate from (tropical) West Africa towards the

warm waters of the tropical Atlantic Ocean [7, 10, 50]. Although, it has been suggested that African Easterly waves are initiated by the barotropic-baroclinic instability that builds up over West African due to the contrast between the warm and dry Saharian surface and the moist tropical forest South of it [7], the present solution suggests that the barotropic instability alone could trigger African Easterly waves.

7.3 Sensitivity to parameters

To demonstrate that the difference in performance of the two methods is due solely to differences in the way the nonlinear advection term is approximated, we perform here a series of sensitivity tests with respect to the various parameters used in the numerical approximation.

First we test the size of the smoothing parameter ε and the artificial viscosity added to the dynamical equation in the case of the Arakawa method. On the left of Figure 7.13, we show the total flow profile of the numerical solutions, at times 10 days, 50 days, and 100 days obtained by the Arakawa method using the larger smoothing parameter $\varepsilon = 8\Delta Y$, i.e, the same as originally used by the ENO-4 scheme. This is contrasted with the solution obtained by the ENO-4 scheme when the same artificial viscosity term and same coefficient $\upsilon = 0.006$, as in the Arakawa method, are used. Note that only results for the coarse grid 64×38 for which the two method show the largest discrepancy are shown.

Comparing the results in Figure 7.13 with those in Figure 7.6 shows that the discrepancy between the Arakawa solution and the ENO-4 solution remains and thus does not depend on these two specific parameters. In fact, since, as already mentioned here, the ENO-4 scheme produces its own viscosity and thus it is not surprinsing that adding a small viscosity term does not make much of a difference. In deed, the fact that the ENO-4 solutions in Figs 7.6 and 7.13 are very similar suggests that the numerical viscosity produced intrinsically by the ENO-4 scheme is larger or similar in magnitude to the one injected artificially with a coefficient $\upsilon = 0.006$.

To test the sentivity of the results to the Poisson solver and the time discrtization, we report in Figure 7.14 the numerical solution obtained by the ENO-4 scheme, on the coarse grid 64×38, when the Poisson equation for the stream-function is handled by the same second order solver used in the Arakawa method: Panels (A), (B), and

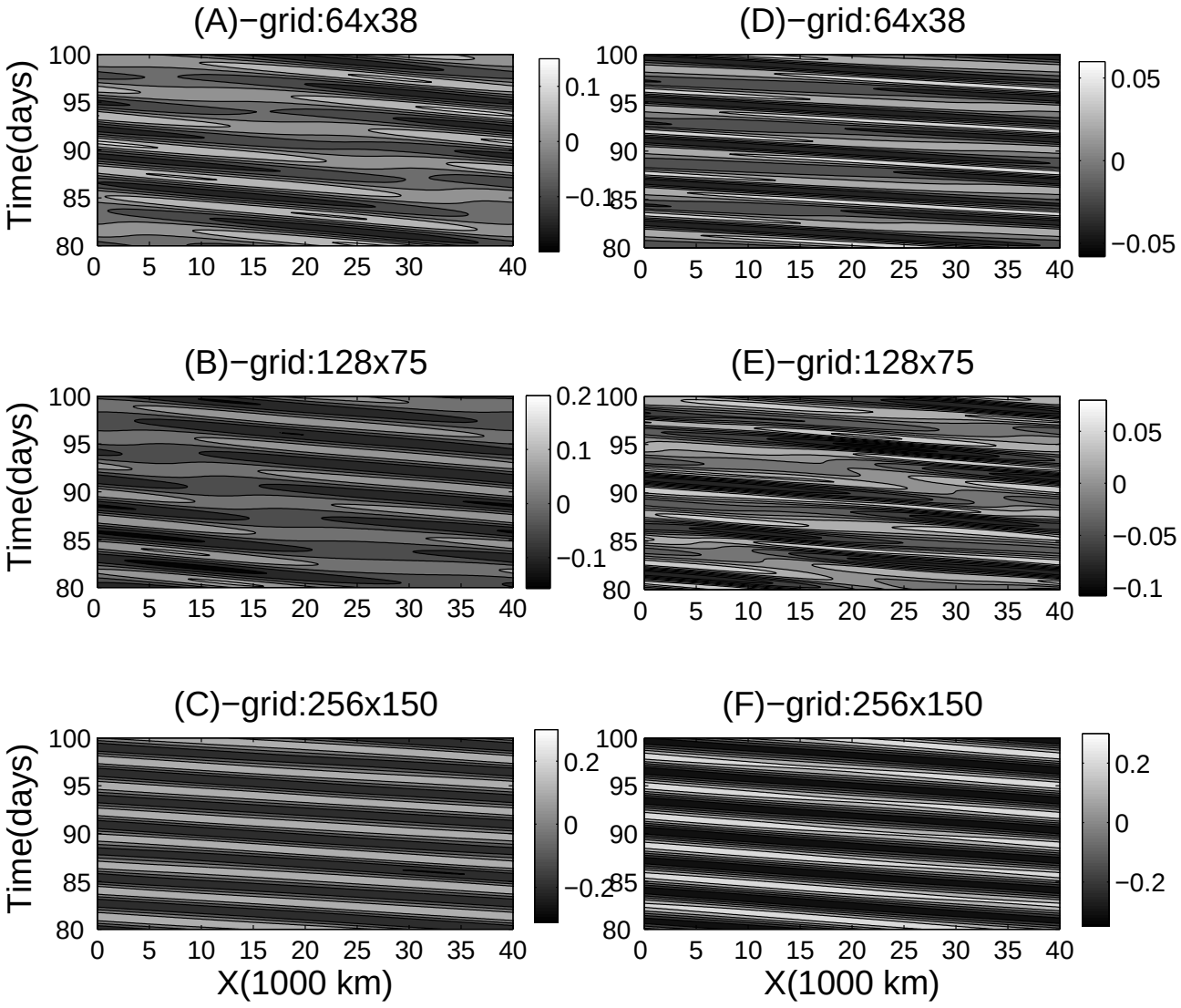

Figure 7.12: Hovmöller diagrams of the six solutions corresponding to the strong perturbation simulations. (A), (B), (C) Arakawa Jacobian method with a viscosity coefficient $\upsilon = 0.006$ using 64×38, 128×75, and 256×150, grid points. (D), (E) and (C) Same as (A), (B) and (C) respectively but for the ENO-4 scheme.

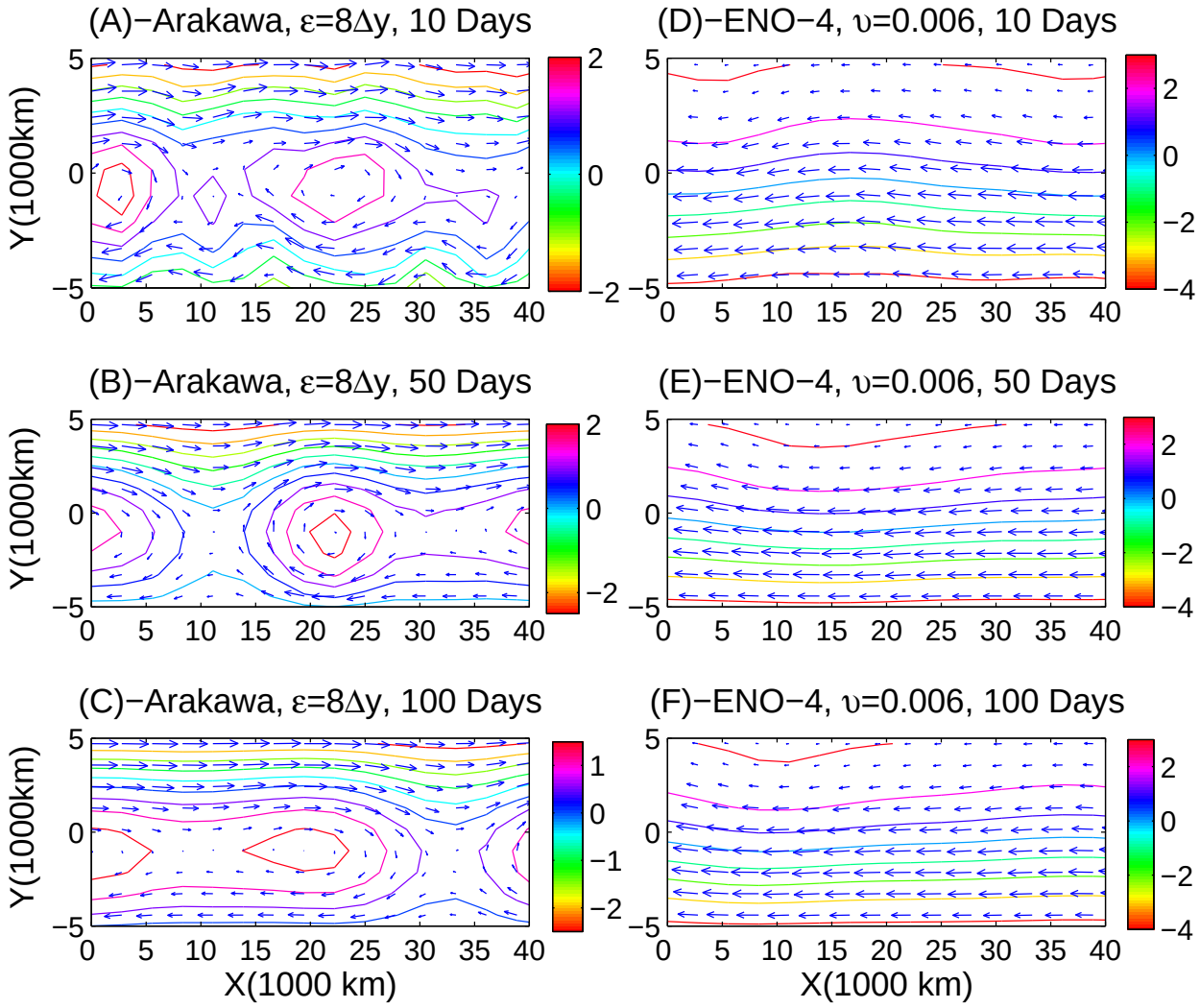

Figure 7.13: Sensitivity tests. Same as Figure 7.6 but with $\varepsilon = 8\Delta Y$ for the Arakawa Jacobian method and ENO-4 scheme with artificial viscosity: $\upsilon = 0.006$.

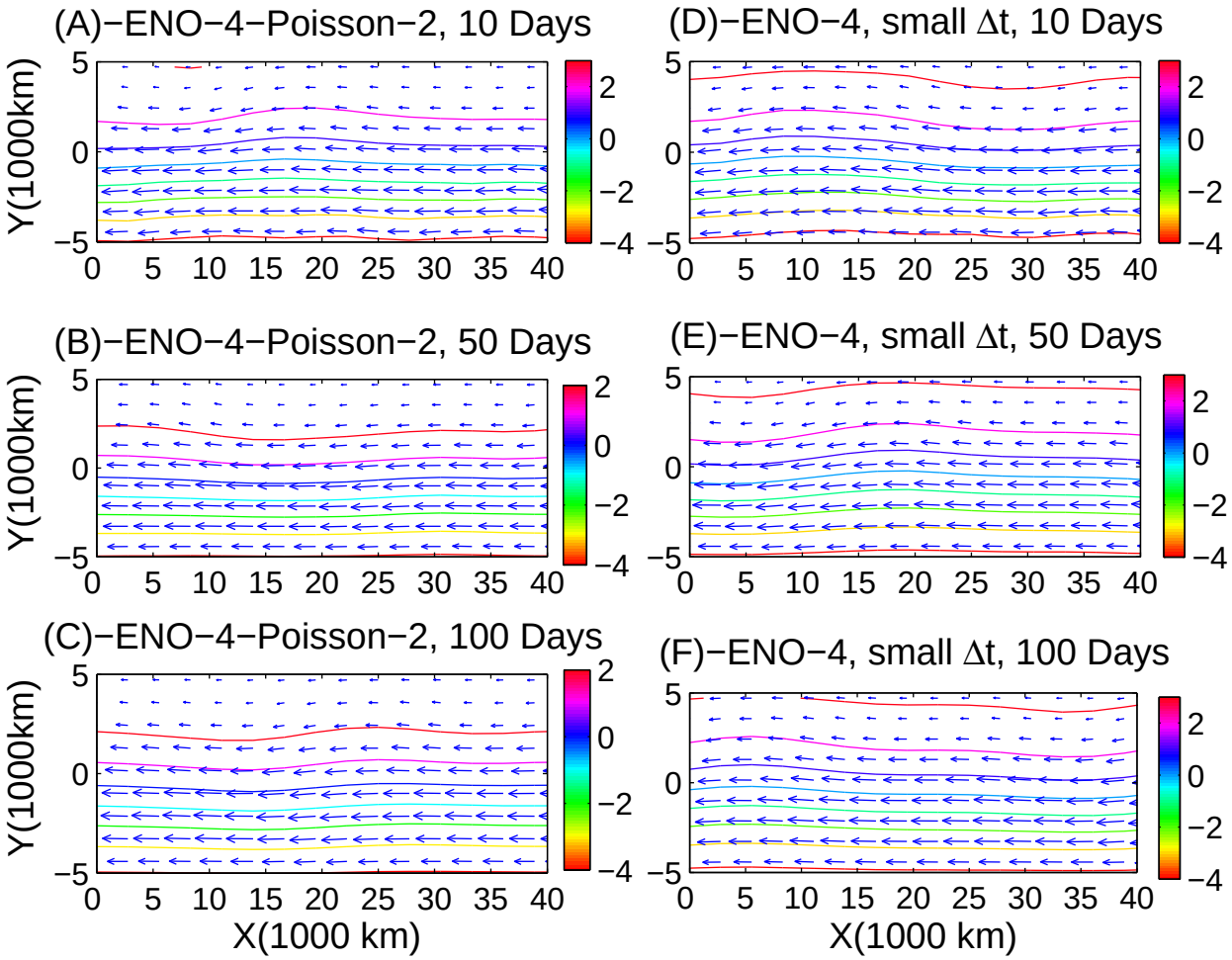

Figure 7.14: Sensitivity tests. Same as Figure 7.6 but for ENO-4 combined with a second-order Poisson solver: Panels (A), (B), and (C) and ENO-4 with a small time stepping $\Delta t = 2.9E-003$: Panels (D), (E), and (F).

(C) and when the time step is fixed to be four times smaller than allowed by the CFL condition (3 E-3 compared to 1.16 E-2). Again comparing these results with those in panels (D), (E), and (F) of Figure 7.6 suggests that the discrepancies between the two methods is not due to some kind of sensitivity of the fourth order poisson solver to the non-smooth initial data or differences in the time discretization used by the two methods.

7. A NUMERICAL SIMULATION OF THE BAROTROPIC INSTABILITY ON THE EQUATORIAL β-PLANE

Chapter 8

Conclusion

This thesis is divided into two parts. The first part discusses the implementation of the Arakawa Jacobian method and the fourth-order essentially non-oscillatory scheme (ENO-4) of Osher and Shu [41] for solving the equatorial barotropic equations. The Arakawa Jacobian scheme [1] is a second order centered finite difference scheme that conserves energy and enstrophy and it is specifically designed for the barotropic vorticity equation in (2.50). As such, it is widely used in the atmosphere-ocean community. The fourth-order essentially non-oscillatory scheme of Osher and Shu [41] however, is originally designed for hyperbolic conservation laws and Hamilton-Jacobi equations, and is used to track sharp fronts. Nonetheless, it can be implemented for any first order non-linear evolution PDE, and in particular for the barotropic vorticity equation in (2.50). The incompressible barotropic vorticity equation is considered in the advective form and solved using the Arakawa Jacobian method and the ENO-4 scheme with an explicit Runge-Kutta time integration. At each stage of the Runge-Kutta integration, the wind field was updated by solving a Poisson problem for the stream function.

In a first test, the numerical schemes for the equatorial barotropic vorticity equations using the Arakawa Jacobian and ENO-4 scheme are validated using a known Rossby wave packet solution. It is shown that as expected the Arakawa Jacobian method conserves energy and enstrophy nearly exactly and captures the dispersive wave structure of the test solution with an overall second order accuracy. The same properties are preserved by the ENO scheme and the large scale dispersive wave is captured with an overall forth-order accuracy. In a second validation test, we considered a discontinuous shear flow with a jump discontinuity at the equator, which in theory,

is an exact solution for the system (2.38), in the weak sens, despite the jump discontinuity. Because the vorticity of the prescribed discontinuous shear flow is a Dirac delta function, a smoothing procedure consisting of approximating the delta function with the regularizing sequence (ρ_ε), where ε, the width of the smoothing region around the discontinuity, is set to $\varepsilon = \Delta y$ for Arakawa's method and $\varepsilon = 8\Delta y$ for the ENO-4 scheme; Δy is the grid spacing in North-South direction. An examination of the rate of convergence, found by taking the ratio of error of two grids at a given time, show that Arakawa's method reproduces the discontinuous shear solution with second order accuracy but the ENO-4 scheme is only third order accurate, for the grids used here.

Comparing the two methods, Arakawa's method is simpler to code and faster at runtime. Moreover in the case of the discontinuous shear flow, the ENO-4 scheme's order of accuracy is reduced due to the regularizing sequence (ρ_ε), which uses a much larger ε value. A recent state of the art method for solving the barotropic vorticity equation is a non-oscillatory central scheme by Khouider and Majda [28]. They showed that the non-oscillatory central scheme can accurately model equatorial waves. However, as demonstrated in [28], the central scheme suffers from a serious problem of phase lagging. The numerical wave solution propagates slower that its exact analog. As it can be summarized from Figure 5.2, the same issue seems to occur her for Arakawa method but it is less severe than what was seen in [28]. The ENO scheme on the other hand, seems to produce a wave packet that moves slightly faster. Moreover, the central scheme has a more serious problem of distorting the shape of the wave because various parts of the wave may be lagged differently, as shown in [11] for the case of equatorially trapped waves. This is due to the systematic averaging along grid cells that characterizes the central scheme [11]. The objective of this numerical solution of the barotropic system by the two methods described in this thesis is a search for an adequate numerical method to study the barotropic instability on the equatorial beta-plane. This is pursued in the second part of this thesis (chapters 6 and 7).

We used two different numerical methods to investigate their performance in tracking the non-linear effects on the longtime evolution of the barotropic instability in an equatorial beta plane: the Arakawa Jacobian [1], and a fourth order ENO-4 scheme, of Osher and Shu [41], which are described and implemented for solving the equatorial barotropic equations in the first part of this thesis (chapters 3 and 4).

For simplicity, we considered a parallel shear flow of Helmholtz-type with a jump discontinuity at the equator. Linear analysis was conducted for the prescribed shear and the standard theory, according to which a necessary condition for instability is that the gradient of the potential vorticity must change sign somewhere in the domain, was revisited. The unstable mode was then used as an initial perturbation for the numerical simulations. Two perturbations were used. A weak perturbation of roughly 1% and a strong perturbation of 50%, relative to the background-equatorially parallel shear. The perturbation consists of a standing zonal wavenumber $k = 10$ mode, repeated periodically over the whole domain (see Figure 7.1).

Because the vorticity of the prescribed shear layer is a Dirac delta function, we use a smoothing procedure which consists of approximating the delta function with the regularizing function ρ_ε where ε, the width of the smoothing region around the discontinuity, is set to $\varepsilon = \Delta Y$ for Arakawa's method and to $\varepsilon = 8\Delta Y$ for the ENO-4 scheme; ΔY is the mesh size in the y-direction. Moreover, because the barotropic instability has no scale selection, i.e, all zonal wavenumber modes have positive growth rates, there is a potential for grid scale instabilities to develop rapidly from roundoff errors and/or from the cascading of energy from large scales to small scales. To eliminate such grid-scale instabilities, a numerical viscosity term is required, in the vorticity equation, for the Arakawa Jacobian method. The ENO-4 scheme has its own numerical dissipation that results from the non-linear stencil which behaves like up-winding discretization near discontinuities.

The two methods were tested against both a small perturbation and a large perturbation initial data and against three different grids: a coarse grid of 64×38 points, an intermediate grid of 128×75 points, and a fine grid of 256×150 points. Each case (12 in total) is run for a total integration time of 100 days. After a short transient period of about 20 days, the solution enters a statistical steady state where grid-scale energy and enstrophy dissipation is minimal. For the small perturbation case, the two methods yield results that are consistent in terms of both the total flow profile at time $t = 100$ and the mean zonal flow, averaged in time, over the last 50 days, and in the zonal direction, at least for the fine resolution cases.

For the weak perturbation case, except for the case of ENO-4 on the coarse mesh, the time evolution curves of energy and enstrophy are to some extent similar. While energy dissipation is minimal, there is an important decrease in enstrophy during roughly the

first 20 days. The finer grids seem to lose more enstrophy during this initial dissipation stage consistent with the fact that they have more significant small-scale contributions due the nature of the discontinuity at initial time (Table 7.2); the more there is enstrophy stored at small scales initially the more it is susceptible for being dissipated quickly by the numerical viscosity. However, in the case of ENO-4 on the coarse mesh, enstrophy seems to be conserved. This is likely due to the fact that the corresponding flow profile in Figure 7.2 (D) is a flat-linear shear which is an exact steady solution towards which the numerical solution appears to converge quickly, in time. Nevertheless, according to the fine mesh solutions, the two methods yield both qualitatively and quantitatively similar solutions consisting of a smooth shear profile around which some weak perturbations evolve. Moreover, from the corresponding profiles of the mean potential vorticity gradient in Figure 7.5, we can see that the final solution doesn't satisfy the necessary condition for barotropic instability unlike the initial shear. Therefore, in this case of a weak perturbation, both methods seem to indicate, that, in the case of the barotropic instability, the main role of the nonlinearity is to drive the background flow towards a stable state.

In the case of a strong initial perturbation, the two methods showed consistent behaviours as in the weak perturbation case. While in the case of the finest grid, both methods resulted in qualitatively and quantitatively similar solutions displaying a cyclonic vortex propagating westward with a phase speed roughly corresponding to that of a planetary scale Rossby wave and of the same equatorially symmetric smooth background shear flow, in the case of the coarse and intermediate grids, they have mixed results. For the coarse grid simulations, the Arakawa Jacobian resulted in an elongated vortex, which is more or less consistent with the fine grid solution but the ENO-4 scheme depicts variability that is rather located on the Northern side of the equator; the intermediate grid has more or less an elongated vortex located in the Northern half of the domain while the coarse mesh solution has its variability confined to the upper boundary with no sign of a vortex. Consistently, the energy and enstrophy time series displayed similar mixed results. Also the final flow backgrounds for the Arakawa's method consisted of smooth shear profiles that are slightly skewed towards the Southern hemisphere, at low resolution, and slowly drifting northward to result in an almost perfectly equatorially symmetric shear flow, at high resolution, consistent with the case of a weak perturbation. But for the ENO-4 scheme, at low resolution,

it exhibits a background shear profile that is heavily skewed towards the North, which then drifts an almost symmetric profile as the grid is refined, consistent with Arakawa's method.

These results show that while at high resolution both methods yield consistent results, that are most likely physically sound, at coarse resolution, only the results of Arakawa's method are somewhat consistent with the converged (fine grid) solution. However, because the initial data consists of a wavenumber 10 perturbation, it provides an extremely hard test case for any numerical method. Nevertheless, the fact that Arakawa's method performed relatively well at such low resolution (of roughly 7 grid points per wavelength), and for both the weak and strong perturbation cases, is somewhat interesting and surprising at the same time. The relatively good performance of Arakawa's method on coarse grids is consistant with earlier findings that showed that the so-called mimetic methods, i.e, methos that conserve the discrete equivalent of some invariants of the original equations such as energy and enstrophy for example perform generally well at coarse resolution [2, 3, 6, 24, 43, 51, 53].

The westward propagating planetary scale vortex solution obtained in the strong perturbation case, at high resolution, can be considered as being the true physical solution towards which the barotropic instability drives the system. It provides an interesting paradigm for tropical meteorology research because it bears some resemblance to tropical depressions, a.k.a. African easterly waves, that are believed to play an important role in the initiation of tropical cyclones (hurricanes) over the tropical-eastern Atlantic ocean. While earlier theories advanced the possibility of these waves being triggered by a combined barotropic-baroclinic instability that builds up over West Africa due to the contrast between the warm Saharian air to the North and the moist tropical forest to the South, the present work is suggestive that the barotropic instability alone is sufficient. Another potential application of the cyclonic vortex solution resides in its resemblance to the monsoon trough which is also believed to be triggered via the baroclinic-barotropic instability mechanism [27]. A natural extension of the present work is to consider the two-way interactions of the barotropic instability with the baroclinic flow following the approach developed in [28] and [29]. This may provide possible mechanisms for the initiation of convectively coupled equatorial waves [11]. Non-linear resonance is suggested to be an important mechanism through which baroclinic and barotropic waves can interact with each other [37]. We finally note that for

a more physically realistic problem, the shear center should be displaced northward to the extra-tropics to mimic the persistence of the jet stream westerlies and the equatorial easterlies.

Bibliography

[1] A. Arakawa, Computational design for long-term numerical integration of the equations of fluid motion,two-dimensional incompressible flow. Journal of computational physics, pp 119-143, 1966. ii, iv, 1, 49, 60, 101, 102, 127, 128

[2] A. Arakawa, V. Lamb, A potential enstrophy and energy conserving scheme for the shallow water equations, MWR, 109, 18–136, (1981). 131

[3] A. Abba', L. Bonaventura, A vorticity preserving finite difference discretization for the incompressible Navier-stokes equations, int. J. Num. Meth. in fluids, **56**, 1101–1106, (2008). 131

[4] G.K, Batchelor An introduction to fluid dynamic. Cambridge University Press, 2000-02-28 - 660 pages. 5

[5] R. Benoit Cushman, B. Jean-Marie, Introduction to geophysical fluid dynamics: Physical and numerical aspects. Academic Press, (2011). 17, 87, 89, 91

[6] L. Bonaventura, T. Ringler, Analysis of discrete shallow water models on geodesic Delaunay grids with C-type staggering, MWR, 133, 2351–2373, (2005). 131

[7] R. W. Burpee, The origin and structure of easterly waves in the lower troposphere of North Africa, J. Atmos. Sci. **29**, 77–90 (1972). 121

[8] J. C. L. Chan, R. T. Williams, Analytical and numerical studies of the beta-effet in tropical cyclone motion. Part I, zero mean flow. Journal of atmospheric sciences 44(9): pp1257-1265, 1987. 1

[9] J. G. Charney, R. Fjortoft, Von Neumann, Numerical integration of the barotropic vorticity equation. Tellus 2(4): pp 237-254, 1950. 1

[10] G. E. Dunn, B. I. Miller, Atlantic hurricanes. Louisiana State Univ. Press, Baton Rouge, Louisiana, 377 pages (1960). 121

[11] J.Ferguson, B.Khouider, M.Namazi, Two-way intraction between equatorially-trapped waves and the barotropic flow. Chinese Annals of Mathematics, Series B 30: pp 2943-2975, 2009. 1, 128, 131

[12] R. Fjortof, Application of integral theorems in deriving creteria of stability for laminar flow and the baroclinic circular vortex. Geofys, Publ. **17**, 52 pages (1950). 3

[13] G.B.Folland, Introduction to partial Differential equation, Princeton Univ. press, Princeton, NJ, (1995).

[14] A. Gill, Atmosphere-ocean dynamics, Academic Press, New York, 1982. 2, 17, 18

[15] D.Gilbarg, and N. S.Trudinger, Elliptic Partial Differential Equations of Second Order, Springer-Verlag, Berlin, revised third printing.

[16] S. Gottlieb, C. W. Shu, Total Variation Diminishing Runge-Kutta schemes, Math. Comput,67: pp 73-85, 1998. 71

[17] M. Grandall and P.Lions, Two approximations of solutions of Hamilton-Jacobi equations, Math. Comput,43: pp 1-19, 1984. 49, 69, 70

[18] F.J.Mc Grath Nonstationary plane flow of viscous and ideal fluid. Arch Rational mech anal V27, pp 329-348, (1968).

[19] A. Harten and S. Osher, Uniformly high order accurate non-oscillatory schemes, I. SIAM J. numer.anal ,24: pp 279-309, 1987. 61

[20] A. Harten, B. Engquist, S. Osher,and S. Chakravarty, Uniformly high order accurate non-oscillatory schemes, III. J.comput.Phys.,71: pp 231-303, 1987. 61

[21] J. R. Holton, An introduction to dynamic meteorology (4th eden). Elsevier Academic Press : Burlington, MA, 2004. 1

[22] L. N. Howard, P. G. Drazin, On instability of parallel flow of inviscid fluid in rotating system with variable Coriolis parameter. J. Math. Phys, **43**, 83–99 (1964). 3, 91, 96

[23] Numerical Methods in Ocean Modelling Lecture Notes for MP066 December 2010. 50

[24] Z.I. Janjic, Nonlinear advection schemes and energy cascade on semi-staggered grids, MWR, 111, 1234–1245, (1984). 131

[25] Kacimi, A., Aliziane, T., Khouider, B.: The Arakawa Jacobian method and a fourth-order essentially nonoscillatory scheme for the beta-plane barotropic equations. International Journal of Numerical Analysis and Modeling. Accepted (2012). ii, iv, 102

[26] A.Kacimi, B.Khouider, A numerical investigation of the barotropic instability on the equatorial beta-plane. Theoretical and Computational Fluid Dynamic, DOI 10.1007/s00162-012-0260-3, 2012. iii, v, 102

[27] Keshavamurty, R. N., Asnani, G. C., Pillai, P. V., Das, S. K.: Some studies of the growth of monsoon disturbances. Journal of Earth System Science **87**, 61–75 (1978). 131

[28] B. Khouider. A. J. Majda,. A non-oscillatory balanced scheme for an idealized tropical climate model. Part I: Algorithm and validation, Theor. Comput. Fluid Dyna. 19: pp 331-354, 2005. 1, 20, 49, 55, 56, 61, 68, 75, 77, 102, 128, 131

[29] B. Khouider, , A. Majda, A non-oscillatory balanced scheme for an idealized tropical climate model. Part II: Nonlinear coupling and moisture effects. Theor. Comput. Fluid Dyn. **19**, 355–375 (2005). 131

[30] H. L. Kuo, Dynamic instability of two-dimensional non divergent flow in a barotropic atmosphere. J.Meteor. **6**, 105–122 (1949). 2, 3, 90

[31] D. Levy, E. Tadmor, Non-oscillatory central schemes for the incompressible 2d Euler equations. Mathematical Research Letters 4, pp 1-20 1997. 1, 55

[32] R. J. LeVeque, Finite volume methods for hyperbolic problems. Cambridge University Press (2002). 102

[33] R. L. Leveque, Finite difference methods for ordinary and partial differential equations: Steady-state and time-dependent problems, SIAM, Philadelphia, USA (2007). 50, 102

[34] R. S. Lindzen, A. J.Rosenthal, On the instability of Helmholtz velocity profiles in stably stratified fluids when a lower boundary is present. J. Geophys. Res. **81**, 1561–1571 (1976). 96

[35] R. S. Lindzen, K. K. Tung, Wave overreflection and shear instability. J. Atmos. Sci. **35**,1626-1632 (1978). 2

[36] A. J. Majda, Introduction to PDE and waves for atmosphere and ocean. Courant Lecture Notes in Mathematic,vol.9. American Mathematical Society, providence 2003. 17, 18

[37] A. Majda, J. Biello, The nonlinear interaction of barotropic and equatorial baroclinic Rossby waves. J. Atmos.sci. **60**, 1809–1821 (2003). 131

[38] A. Majda, A. Bertozzi, Vorticity and Incompressible Flow, Cambridge University (2001). 25, 26, 31

[39] K.W. Morton, P.L.Roe, Vorticity preserving Lax-Wendrof type schemes for the system wave equation, SIAM J. Sci. Comp., **23**, 170–192 (2001).

[40] J. E. Nielsen, M. R. Schoeberl, A numerical simulation of barotropic instability. Part II: Wave-wave interaction. J. At- mos. Sci. **41**, 2869–2881 (1984). 3

[41] S. Osher and C. W. Shu, High-order essentialy nonoscillatory schemes for Hamilton-Jacobi equations. Siam J. Numer. Anal., vol. 28, No4: pp 907-922, 1991. ii, iv, xi, 2, 49, 62, 68, 69, 72, 101, 102, 127, 128

[42] J.Pedlosky, The stability of currents in the atmosphere and the oceans. Part I.J. Atmos.Sci., **21** 201–219 (1964). 93, 120

[43] B.Perot, Conservation properties of unstructured staggered mesh schemes, JCP, **159**, 58–89, (2000). 131

[44] M.Petcu, Euler equation in a channel in space dimension 2 and 3. Discrete and Continuous Dynamical Systems. Series A, 13, n3, 208: 215-257 (2005) 25, 29, 31, 36, 37, 41

[45] N.A. Phillips, An example of non-linear computational instability, the atmosphere and the sea in motion, Rossby memorial volume: pp 501-504. Rockefeller Institute Press, New York, 1959. 56

[46] W.H. Press, S.A. Teukolsky, W.T. Vetterling and B.P. Flannery, Numerical recipes in Fortran, 2nd ed., Cambridge University Press, New York, 1992. 54

[47] L. Rayleigh, On the instability of the jets. Scientific Papers **1**, 361–371 (1879). 3

[48] Rayleigh, Lord (John William Strutt), On the stability, or instability, of certain fluid motions. Proc. London Math. Soc. **9**, 57–70 (1880). (Reprinted in Scientific Papers by Lord Rayleigh, **3**, 594–596 (1880). 3, 91

[49] L.Rayleigh, On the stability or instability of certain fluid motions, II, Proceedings of the London Mathematical Society, 1887 (also in Lord Rayleigh, Scientific Papers, **3**, Cambridge, pp. 17–23 (1887). 3

[50] H. Riehl, Waves in the easterlies and the polar front in the tropics. Misc. Rep. No. 17, Department of Meteorology, University of Chicago, 79 pages (1945). 121

[51] T.D. Ringler, D.A. Randall, A potential enstrophy and energy conserving numerical scheme for solution of the shallow-water equations a geodesic grid, MWR,**130**, 1397–1410 (2002). 131

[52] T.D. Ringler, J. Thuburn, J.B. Klemp, W.C. Skamarock, A unified approach to energy conservation and potential vorticity dynamics for arbitrarily-structured C-grids, JCP, **229**, 3065-3090 (2010).

[53] R.Sadourny, The dynamics of finite difference models of the shallow water equations, JSA, 32, 680–689 (1975). 131

[54] M. R. Schoeberl, R. S. Lindzen, A numerical simulation of barotropic instability. Part I. Wave-mean flow Interaction. J. Atmos. Sci. **41**, 1368–1379 (1984). 3

[55] M. R. Schoeberl, J. E. Nielsen, A numerical simulation of barotropic instability. Part III. Wave-wave interaction with dissipation. J. of the Atmos. Sci. **41**, 2869–2881 (1984). 3

[56] A. Solomon, R. S. Lindzen, The impact of resolution on a numerical simulation of barotropic instability. J. Atmos. Sci. **57**, 3799–3816 (1999). 3

[57] C. W. Shu, and S. Osher, Efficient implementation of essentially non-oscillatory shock-capturing schemes I, Journal of Comput physic, 77: pp 439-471 1988. 71, 72

[58] C. W. Shu, and S. Osher, Efficient implementation of essentially non-oscillatory shock-capturing schemes II, Journal of Comput physic, 83: pp 32-78 1989. 71

[59] L. D. Talley, Radiating barotrpic instability. Journal of physical Oceanography **13**, 972–987 (1983). viii, 91, 95, 98, 99

[60] L. D.Talley, Instabilities and radiation of thin, baroclinic jets. Thesis (PhD). Massachusetts Institute of Thechnology and the Woods Hole Oceanographic Institutions (1982). viii, 95, 96, 98, 99

[61] G. Vallis, Atmospheric and Oceanic Fluid Dynamics; Fundamentals and Large-scale Circulation. Cambridge University Press; 2006. 5, 11

[62] D. L. Williamson, Integration of the barotropic vorticity equation on a spherical geodisic grid. Tellus, 20(4):pp 642-653, 1968. 1

[63] W. Wolibner, Un theoreme d'existence du mouvement plan d'un fluid parfait, incompressible, pendant un temps infiniment long. Math. Zeitschrift, 37 pp 698-726. (1933).

[64] V. I.Yudovich,Non-stationary flow of an incompressible liquid, Zh. Vychisl. Mat. Mat. Fiz. 3, 10321066, 1963.